

December 1997

Master of Science

for the Degree of
of the Requirements
Submitted in Partial Fulfillment

©1997 Robert Todd Klaput

Robert Todd Klaput

by

Aerospace Engineering

A Thesis in

WITH ACTIVE FLOW CONTROL IMPLICATIONS

AROUND A LOW-SPEED AIRFOIL AT HIGH ANGLE OF ATTACK

AN EXPERIMENTAL STUDY OF THE VISCOUS FLOWFIELD

Department of Aerospace Engineering

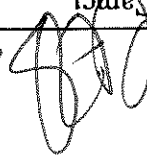
The Graduate School

The Pennsylvania State University

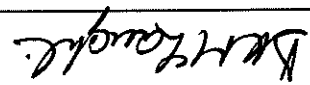
Date of Signature

11/20/1997

Cengiz Camci
Associate Professor of Aerospace Engineering
Thesis Advisor



Dennis K. McLoughlin
Professor of Aerospace Engineering
Head of the Department of Aerospace Engineering



11/21/1997

Mark D. Maughmer
Associate Professor of Aerospace Engineering



11/29/1997

We approve the thesis of Robert Todd Klaput.

Robert T. Klaput
Robert T. Klaput

I grant The Pennsylvania State University the nonexclusive right to use this work for the University's own purposes and to make single copies of the work available to the public on a not-for-profit basis if copies are not otherwise available.

heat transfer data as a baseline solution for the development of better heat transfer/viscous heat transfer data was verified numerically, thus providing confidence in the use of the near the airfoil surface than was found by using either method alone. The accuracy of the visualizat ion. Using both methods in conjunction revealed more detail of the viscous flow

The heat transfer study was found to compliment the conventional oil flow

the large-scale flow structures were shed.

gauges and single sensor hot-wire probes were used to determine the frequencies at which and shed from the airfoil under stalled conditions. Time-accurate surface shear stress progressed to examining the nature of the large-scale vortical structures that are created thermochromic liquid crystals to generate heat transfer coefficient maps. Work then regions: fluorescent oil flow visualization and a heat transfer study which utilized discussed. Two experimental methods were used to document these surface viscous flow information is necessary so that the location at which to put control actuators can be determined. The viscous flow regions on the suction surface of the airfoil. This separation on a low speed airfoil under stalled conditions. Initial work involved This thesis presents necessary background work for the active control of flow used as a possible explanation for this flow reattachment phenomenon.

surface over which the flow is separated. An argument involving the Coanda effect can be free shear layer will be drawn toward the surface, be it that of an airfoil or any other strengthened. The entrainment of free stream fluid will then be increased. The separated coherent vortical structures in the separated shear layers can be artificially excited and mixing process in the separated free shear layer. The naturally existing large-scale It is possible that separation control may be achieved through enhancement of the and windmills would be more efficient with separation control.

coefficients and lower stall speeds. Runway distances could then be shortened. Propellers leading to better fuel efficiency. Airfoil lift can be enhanced creating higher maximum lift diffusers become more efficient if separation is reduced. Vehicle drag can be lessened active control of flow separation can be beneficial for many fluid flow systems. Inlet

ABSTRACT

flow solvers. The qualitative shear stress measurements along the chord of the airfoil revealed to instill more confidence in the trends of the heat transfer results but failed to reveal dominant flow instability frequencies. In effect, the flow recirculating region acts as a buffer to shield the dominant frequencies of the coherent structures that exist in the separated shear layer from detection by the surface shear stress gauges. Wake profile hot-wire anemometry measurements easily captured the frequencies of these large-scale coherent structures. In addition, velocity fluctuation skewness measurements and smoke flow visualization verified the existence of the large-scale flow structures. These flow structures were seen to not only dominate the flow physics away from the airfoil, but also to cause significant increases in the convective heat transfer and turbulence levels on the surface near the trailing edge of the airfoil.

A limited examination of the use of piezoelectric films as surface actuators was performed and revealed possible difficulties in using the films to excite the coherent flow structures of the separated shear layer. As a result of the work presented in this thesis, a reasonable active control strategy may now be developed and pursued for separation control on the SM701 airfoil under stalled conditions at low Reynolds numbers.

1	INTRODUCTION	
2	EXPERIMENTAL MODEL AND FACILITIES	4
2.1	The Airfoil Definition	4
2.2	The Axisymmetric Wind Tunnel (ASWT)	9
2.3	The Low-Speed Low-Turbulence Wind Tunnel (LSLT)	10
3	BOUNDARY LAYER PREDICTIONS ON THE AIRFOIL SECTION SIDE	12
3.1	Potential Flow	12
3.2	Boundary Conditions	17
3.2.1	Initial Considerations	17
3.2.2	Starting Velocity Profile	19
3.3	The Boundary Layer Code STANS	25
4	EXAMINATION OF VISCOSUS FLOW REGIONS ON SM701 AIRFOIL	29
4.1	Fluorescent Oil Flow Visualization	29
4.1.1	Oil Flow Visualization Objective	29
4.1.2	Oil Flow Visualization Procedure	29
4.1.3	Oil Flow Visualization Results	31
4.1.4	Conclusions from Oil Flow Visualization	41
4.2	Liquid Crystal Thermography	43
4.2.1	Objectives of the Heat Transfer Experimentation	43
4.2.2	Liquid Crystal History and Properties	44
4.2.3	Types of Heat Transfer Experiments	50
4.2.3.1	Transient Technique	50
4.2.3.2	Steady State Technique	53
4.2.4	Importance of the Convective Heat Transfer Coefficient, h	55
4.2.5	Past Heat Transfer Work Using Liquid Crystals	57
4.2.6	Experimental Determination of the Thermal Conductivity of the Wing Material	59
4.2.7	The Image Processing System	65
4.2.8	Modifications to Model Prior to ASWT Heat Transfer Experimentation	65
4.2.9	ASWT Setup for Heat Transfer Experimentation	67
4.2.10	ASWT Experimental Procedure	70
4.2.11	Problems Discovered and Knowledge Gained During ASWT Tests	72
4.2.12	Modifications to the Model Prior to LSLT Heat Transfer Experimentation	74
4.2.12.1	Fabrication of the Wing Extensions	74
4.2.12.2	Model Changes Due to Knowledge Gained	74
4.2.13	LSLT Setup for Heat Transfer Experimentation	84

TABLE OF CONTENTS

<p>BIBLIOGRAPHY</p> <p>254</p> <p>APPENDIX A: ASWT Turbulence Intensity Information 203</p> <p>APPENDIX B: Numerical Predictions Input Information 204</p> <p>APPENDIX C: Heat Transfer Codes 208</p> <p>APPENDIX D: Hot-Wire Anemometry Codes 229</p>	<p>8 SUGGESTIONS FOR FUTURE WORK 199</p> <p>7 CONCLUSIONS 197</p> <p>6.1 Background on Piezoelectric Materials 191</p> <p>6.2 The Experiment 192</p> <p>6 SIMPLE ACTIVE CONTROL TEST USING PIEZOELECTRIC FOIL 191</p> <p>5.2.1 Objectives of Hot-Wire Flowfield Experimentation 147</p> <p>5.2.2 Experimental Setup for Hot-Wire Flowfield Measurements 147</p> <p>5.2.3 Description of Data Acquisition and Data Reduction Codes 152</p> <p>5.2.4 Verification of Experimental Setup 154</p> <p>5.2.5 Procedure for Hot-Wire Flowfield Measurements 156</p> <p>5.2.6 Hot-Wire Flowfield Measurements Results 157</p> <p>5.2.7 Conclusions from Hot-Wire Flowfield Measurements 188</p> <p>5.2.8 Verification of Hot-Wire Flowfield Measurements 188</p> <p>5.1.1.1 Objectives of Qualitative Shear Stress Experiments 126</p> <p>5.1.1.2 Past Work with Shear Stress Gauges 127</p> <p>5.1.1.3 Setup for Qualitative Shear Stress Measurements 128</p> <p>5.1.1.4 Description of Data Acquisition and Data Reduction Codes 130</p> <p>5.1.1.5 Procedure for Qualitative Shear Stress Measurements 131</p> <p>5.1.1.6 Qualitative Shear Stress Results 132</p> <p>5.1.1.7 Conclusions from Qualitative Shear Stress Measurements 146</p> <p>5.2 Hot-Wire Flowfield Measurements 147</p> <p>5.2.1 Objectives of Hot-Wire Flowfield Experimentation 147</p> <p>5.2.2 Experimental Setup for Hot-Wire Flowfield Measurements 147</p> <p>5.2.3 Description of Data Acquisition and Data Reduction Codes 152</p> <p>5.2.4 Verification of Experimental Setup 154</p> <p>5.2.5 Procedure for Hot-Wire Flowfield Measurements 156</p> <p>5.2.6 Hot-Wire Flowfield Measurements Results 157</p> <p>5.2.7 Conclusions from Hot-Wire Flowfield Measurements 188</p> <p>5.1.1.1 Objectives of Qualitative Shear Stress Experiments 126</p> <p>5.1.1.2 Past Work with Shear Stress Gauges 127</p> <p>5.1.1.3 Setup for Qualitative Shear Stress Measurements 128</p> <p>5.1.1.4 Description of Data Acquisition and Data Reduction Codes 130</p> <p>5.1.1.5 Procedure for Qualitative Shear Stress Measurements 131</p> <p>5.1.1.6 Qualitative Shear Stress Results 132</p> <p>5.1.1.7 Conclusions from Qualitative Shear Stress Measurements 146</p> <p>5.1 Qualitative Shear Stress Measurements 126</p> <p>5.0.1 Fluid Instability 113</p> <p>5.0.2 Importance of Separation Control 115</p> <p>5.0.3 Approaches To Separation Control 115</p> <p>5.0.4 Past Work in Control of Separated Shear Layers 120</p> <p>5.0.5 Keys to Controlling the Separated Shear Layer 124</p> <p>5.1.1.1 Objectives of Qualitative Shear Stress Experiments 126</p> <p>5.1.1.2 Past Work with Shear Stress Gauges 127</p> <p>5.1.1.3 Setup for Qualitative Shear Stress Measurements 128</p> <p>5.1.1.4 Description of Data Acquisition and Data Reduction Codes 130</p> <p>5.1.1.5 Procedure for Qualitative Shear Stress Measurements 131</p> <p>5.1.1.6 Qualitative Shear Stress Results 132</p> <p>5.1.1.7 Conclusions from Qualitative Shear Stress Measurements 146</p> <p>5 EXAMINATION OF POST-STALL FLOW INSTABILITIES 113</p> <p>4.2.14 Calibration of the Liquid Crystals 88</p> <p>4.2.15 LSLTT Experimental Procedure 91</p> <p>4.2.16 LSLTT Heat Transfer Results 92</p> <p>4.2.17 Conclusions from LSLTT Heat Transfer Measurements 109</p> <p>4.2.18 LSLTT Heat Transfer Error Analysis 110</p>
---	--

Figure	Page	Description
2.1	2	SMT01 Airfoil Shape
2.2	6	Sandwich Panel Construction of the Test Model Skin
2.3	7	Leading Edge Spar of the Airfoil
2.4	8	The Airfoil Model
2.5	9	Axysymmetric Wind Tunnel (ASWT)
2.6	10	Low-Speed Low-Turbulence Wide Tunnel (LSLT)
3.1	13	Venification of Panel f
3.2	14	Potential Flow Cp Distribution for $\alpha = 0^\circ$
3.3	15	Non-dimensional Velocity Distribution for $\alpha = 0^\circ$
3.4	16	The Boundary Layer (B.L.) Coordinate System
3.5	17	Outer Flow Velocity Distribution in B. L. Coordinate System
3.6	19	Setup for Falkner-Skan Wedge Flow Solution
3.7	22	Determination of m for $\alpha = 0^\circ$
3.8	23	Falkner-Skan Similarity Profile for SMT01 at $\alpha = 0^\circ$
3.9	27	Comparison of STANS C, Results and Blasius Solution
3.10	28	Comparison of STANS C, Results and Blasius Solution
4.1a	32	$\alpha = 0^\circ$, $Re = 315,000$, ASWT
4.1b	32	$\alpha = 0^\circ$, $Re = 315,000$, LSLTT
4.1c	34	$\alpha = 10^\circ$, $Re = 315,000$, LSLTT
4.2a	35	$\alpha = 15^\circ$, $Re = 315,000$, ASWT
4.2b	35	$\alpha = 15^\circ$, $Re = 315,000$, LSLTT
4.2c	35	$\alpha = 5^\circ$, $Re = 750,000$, LSLTT
4.3a	34	$\alpha = 10^\circ$, $Re = 315,000$, ASWT
4.3b	34	$\alpha = 10^\circ$, $Re = 315,000$, LSLTT
4.4a	35	$\alpha = 15^\circ$, $Re = 315,000$, ASWT
4.4b	35	$\alpha = 15^\circ$, $Re = 315,000$, LSLTT
4.4c	35	$\alpha = 15^\circ$, $Re = 750,000$, LSLTT
4.5a	36	$\alpha = 18^\circ$, $Re = 315,000$, ASWT
4.5b	36	$\alpha = 18^\circ$, $Re = 315,000$, LSLTT
4.5c	36	$\alpha = 18^\circ$, $Re = 750,000$, LSLTT
4.6a	37	$\alpha = 20^\circ$, $Re = 315,000$, ASWT
4.6b	37	$\alpha = 20^\circ$, $Re = 315,000$, LSLTT
4.6c	37	$\alpha = 20^\circ$, $Re = 750,000$, LSLTT
4.7	40	Sketch of a Lamellar Separation Bubble
4.8	40	Two Regions of Lamellar Separation Bubble
4.9	45	Smectic Liquid Crystal Molecular Structure
4.10	46	Nematic Liquid Crystal Molecular Structure

4.11	: Cholesteric Liquid Crystal Molecular Structure	47
4.12	: Clarification of Transient Heat Transfer Method	52
4.13	: The Composite Heater Element	53
4.14	: Various Flow Regimes in Which h Can Validate Codes	56
4.15	: Sketch of Wing Material Being Tested	60
4.16a	: K Test Piece	62
4.16b	: Side View of K Test Piece	62
4.16c	: Insulation Material	62
4.16d	: Insulating the Test Piece	62
4.16e	: Assembly of Insulating Box	62
4.16f	: Insulation Complete	62
4.16g	: Final K Testing Setup	62
4.17	: Experimental Determination of k_{wall}	64
4.18	: Inconel Before Painting	67
4.19	: The Model in the ASWT	68
4.20	: Schematic of ASWT Heat Transfer Experimentation Setup	70
4.21	: Edge Effects on The Heater Strip Color Pattern	73
4.22	: Sketch of Inside of Model for ASWT Tests	73
4.23	: Rectangular Indenting Table Mount	75
4.24a	: Top Wing Extension (lower surface view)	76
4.24b	: Bottom Wing Extension (lower surface view)	77
4.25	: Model with Extensions Mounted in LSLTT	78
4.26	: Aligning Load-Carrying Assembly	79
4.27a	: Aligning Load-Carrying Beams	80
4.27b	: Aligning Load-Carrying Beams (cont.)	80
4.28a	: Beginning Wing Extension Assembly	80
4.28b	: Matting Extension to Wing	80
4.28c	: Attachment of First Foam Piece	81
4.28d	: Attachment of Final Foam Piece	81
4.28e	: Extension After Sanding	82
4.28f	: Completed Extensions Before Covering	82
4.29	: Calibration of the Nine Thermocouples	85
4.30	: Model Mounted to Rotary Indenting Table	86
4.31	: Rotating Bearing Mount Above Test Section	86
4.32	: Model Mounted in LSLTT Test Section (view of upper surface)	87
4.33	: Schematic of LSLTT Heat Transfer Experimentation Setup	88
4.34	: Liquid Crystal Calibration Graph	89
4.35	: Hue Versus Intensity Check for Liquid Crystal Calibration	91
4.36	: h Map for $\alpha = 0^\circ$, $Re = 315,000$	94
4.37	: h Map for $\alpha = 0^\circ$, $Re = 750,000$	94
4.38	: h Map for $\alpha = 5^\circ$, $Re = 315,000$	95
4.39	: h Map for $\alpha = 5^\circ$, $Re = 750,000$	95
4.40	: h Map for $\alpha = 10^\circ$, $Re = 315,000$	96
4.41	: h Map for $\alpha = 10^\circ$, $Re = 750,000$	96

4.42	: h Map for $\alpha = 15^\circ$, $Re = 750,000$	97
4.43	: h Map for $\alpha = 18^\circ$, $Re = 750,000$	98
4.44	: h Map for $\alpha = 20^\circ$, $Re = 750,000$	99
4.45	: Velocity Distribution over a Separation Bubble	101
4.46	: Cf, Trend After Flow Reattachment	102
4.47	: Convective Heat Transfer in a Separation Bubble	103
4.48	: Schematic Interpretation of Streamwise Vortices at Reattachment	105
4.49	: Evidence of Longitudinal Vortices at Reattachment	106
4.50	: Comparison of Heat Transfer Results to Cylinder-in-Crossflow	107
4.51	: Heater Strip Negative Effect on Flow	108
5.1	: The Coanda Effect (Surface Located Near a Jet)	117
5.2	: Airfoil Flow Separation	118
5.3	: Summary of the Two Main Separation Control Approaches	119
5.4	: Flow Reattachment Caused by Sound	120
5.5	: Schematic of Setup for Qualitative Shear Stress Measurements	129
5.6	: The DISA 55M01, Krohn-Hite Filter, and Techkor Amplifier	129
5.7	: $\alpha = 0^\circ$, $Re = 315,000$	133
5.8	: $\alpha = 5^\circ$, $Re = 315,000$	133
5.9	: $\alpha = 10^\circ$, $Re = 315,000$	136
5.10	: $\alpha = 15^\circ$, $Re = 315,000$	136
5.11	: $\alpha = 18^\circ$, $Re = 315,000$	138
5.12	: Coherent Vortical Structures in Separated Shear Layer	138
5.13	: Separated Flow Region Streamlines, $\alpha = 20^\circ$, $Re = 315,000$	139
5.14	: Separated Flow Region Velocity Vectors, $\alpha = 20^\circ$, $Re = 315,000$	139
5.15	: Turbulent Kinetic Energy Along Airfoil Surface, $\alpha = 20^\circ$	141
5.16	: Enhanced Training Edge Heat Transfer (ASWT), $\alpha = 20^\circ$	141
5.17	: Visualization of Coherent Vortical Structures, $\alpha = 20^\circ$	142
5.18	: $\alpha = 20^\circ$, $Re = 315,000$	144
5.19	: $\alpha = 22^\circ$, $Re = 315,000$	144
5.20	: $\alpha = 25^\circ$, $Re = 315,000$	145
5.21	: $\alpha = 20^\circ$, $X/C = 70\%$	145
5.22	: Schematic of Setup for Flowfield Measurements	149
5.23	: Travelse Calibration	150
5.24	: Calibration of Hot-Wire Agamist Pitot-Static Probe	151
5.25	: Hot-Wire Calibration Polynomial and Its Repetability	152
5.26	: Simple Propeller Test for Hot-Wire Measurement System	155
5.27	: Velocity Profile and Wake Survey Locations for $\alpha = 15^\circ$	158
5.28	: $\alpha = 15^\circ$, $Re = 315,000$, $X/C = 80\%$	159
5.29	: $\alpha = 15^\circ$, $Re = 315,000$, $X/C = 90\%$	160
5.30	: $\alpha = 15^\circ$, $Re = 315,000$, $X/C = 90\%$	162
5.31	: Wake Survey Location for $\alpha = 18^\circ$	163
5.32	: $\alpha = 18^\circ$, $Re = 315,000$, $0.75c$ Wake	164
5.33	: $\alpha = 18^\circ$, $0.75c$ Wake	166

5.34	: $\alpha = 18^\circ$; $Re = 315,000$; 0.75c Wake	167
5.35	: Velocity Profile and Wake Survey Locations for $\alpha = 20^\circ$	169
5.36	: $\alpha = 20^\circ$; $Re = 315,000$; $x/c = 25\%$	170
5.37	: $\alpha = 20^\circ$; $Re = 315,000$; $x/c = 50\%$	171
5.38	: $\alpha = 20^\circ$; $Re = 315,000$; $x/c = 70\%$	172
5.39	: Hot-Wire Recirculation in 1D Reversing Flowfield	173
5.40	: $\alpha = 20^\circ$; $Re = 315,000$; 0.25c Wake	175
5.41	: $\alpha = 20^\circ$; $Re = 315,000$; 0.75c Wake	176
5.42	: $\alpha = 20^\circ$; $Re = 315,000$	177
5.43	: Wake Survey Location for $\alpha = 22^\circ$	181
5.44	: $\alpha = 22^\circ$; $Re = 315,000$; 0.75c Wake	182
5.45	: Wake Survey Location for $\alpha = 25^\circ$	183
5.46	: $\alpha = 25^\circ$; $Re = 315,000$; 0.75c Wake	184
5.47	: Dominant Instability Frequency as Function of Alpha	186
5.48	: Modified Strouhal Number as Function of Alpha	186
5.49	: Summary of Important Hot-Wire Experimentation Conclusions	190
6.1	: Piezoelectric Film	192
6.2	: Attachment Location of PVDF Film Element	193
6.3	: The Function Generator with Digital Oscilloscope	193
6.4	: The Microphone Above the PVDF Element	195
8.1	: Synthetic Jet Actuator	201
A.1	: ASWT Turbulence Intensity Level	203

2.1	: SM701 Airfoil Coordinates	5
2.2	: LSLT Description Summary, (Brophy, 1994)	11
3.1	: Information Required for Dimensional Starling Profile Calculations	24
4.1	: Fluorescent Oil Flow Visualization Summary	42
4.2	: Selected Samples of Thermal Conductivity Values of Insulators	64
4.3	: Estimates of Uncertainties in Measured Quantities	110
4.4	: Summary of Heat Transfer Uncertainty Analysis	112
5.1	: Test Matrix for Qualitative Shear Stress Experimentation	132
5.2	: Test Matrix for Hot-Wire Experimentation	156
5.3	: Sf_{sim} Results for Various High-Angle-of-Attack Airfoil Experiments	188
B.1	: Inputs for Panel f for Angle of Attack = 0 degrees	204
B.2	: STAN5 Input File - SM701 Airfoil, $\alpha = 0^\circ$; $Re=315000$	205

LIST OF TABLES

A	: area
c	: airfoil chord, also specific heat at constant pressure
C_s	: skin friction coefficient
C_p	: pressure coefficient
D	: van Driest damping function
e	: fluctuation voltage
E	: mean voltage
f	: dependent variable in Falkner-Skan similarity solution
$f_{excitation}$: excitation frequency
f_s	: dominant flow instability frequency (shedding frequency)
h	: convective heat transfer coefficient
I^*	: fluctuation stagnation enthalpy
k	: thermal conductivity
l	: mixing length
Ma	: Mach number
p	: local static pressure
p_a	: free stream static pressure
q''	: heat flux per unit area
R	: electrical resistance
Re	: Reynolds number based on airfoil chord
s	: arc length coordinate from airfoil leading edge stagnation point in boundary layer coordinate system
$Si_{Stm,a}$: Strouhal number based on airfoil chord
Si	: modifed Strouhal number ($= St \cdot \sin \alpha$)
t	: time
T_u	: turbulence intensity
U	: fluctuation velocity in boundary layer in x -direction
U_x	: inviscid velocity at airfoil surface in x - y coordinate system
U_{ANSYS}	: inviscid velocity at outer edge of boundary layer in boundary layer coordinate system
U_y	: mean velocity in boundary layer in y -direction
U_z	: fluctuation velocity in boundary layer in y -direction
V	: mean velocity in boundary layer in y -direction
x,y	: coordinates of airfoil surface point location in Cartesian coordinate system
y	: also coordinate normal to airfoil surface in boundary layer coordinate system
α	

NOMENCLATURE

Subscripts

∞	: free stream quantity
$wall$: quantity pertaining to wall of model
rms	: root-mean-square value
$initial$: initial value
avg	: average value
air	: quantity pertaining to air

Greek

ζ	: Stefan-Boltzmann constant
ρ	: air density
ν	: air kinematic viscosity
κ	: turbulence viscosity
μ	: air viscosity
η	: von Karman constant
τ	: independent variable in Falkner-Skan similarity solution
ϵ_m	: eddy diffusivity for momentum
ϵ_e	: emissivity
δ_{99}	: 99% boundary layer thickness
α	: angle of attack with respect to airfoil chordline

$(\bar{ })$: time averaged quantity

Many people have helped to make my time at Penn State enjoyable. First I must thank my advisor Dr. Cengiz Camci for his time and help throughout my work. Also important are Dr. Dennis McLoughlin and Dr. Mark Maughmer who always had helpful and insightful comments on my research.

I must thank Chris Bosetti for teaching me about the operation of low-speed wind tunnels and for the rides in the Thing. Chris McLean was very helpful regarding instrumentation and deserves my gratitude. Thanks to Todd Wolowink for assisting in the setup for the hot-wire anemometry experiments and the signal analysis. Also, without Rick Auhl and Mark Sausseur my research effort would have been much more difficult. In addition, I want to thank Ms. Shelia Corl as well as the other secretaries for always being helpful. Thanks to Eric Donahoo for the interesting conversations over the years and to Oguz Uzol for performing the computer flowfield simulations.

My friends and family have also been very important to me during my time at Penn State. Thanks to my friends for the comic relief they provide: Manny Wolfe, Tim Malec, Dave Cribbs, Drew Fennell, and all those I can not name. I must thank my parents, Robert and Donna, and my sister Melanie for their continued support throughout the years. In addition, thanks to my grandparents who were always there for me, especially my grandfather Edward Klaput, for the interest he showed in all of my work that has culminated with this thesis.

ACKNOWLEDGMENTS

The subject of active control of separated flow regions has become a popular research topic since the discovery in the mid 1970's that large-scale coherent structures dominate the development of turbulent mixing layers. A coherent structure is defined by Hussain as a large-scale turbulent fluid mass with phase-correlated vorticity which transports significant amounts of mass, momentum, and energy (Hussain, 1983). Before coherent structures were understood to dominate turbulent flow regions, the flow was regarded as random motion of fluid particles at all scales which could only be studied by statistical analysis. However, today, with the understanding of deterministic coherent structures, it is generally believed that appropriate aerodynamic excitation can enhance the strength of the naturally occurring coherent structures in a separated turbulent mixing layer influence the turbulent mixing layer growth. By affecting the turbulent mixing layer growth, any separated flow region beneath the mixing layer will also be altered.

Separation control has many applications in all fields of fluid mechanics. Through separation control turbines and reduced approach speeds, supermaneuverability, better engine noise, shorter runways and reduced separation control, propellers, windmills, inlets, and diffusers could be made more efficient. Increased C_{μ} and a_{μ} of airfoils, improved axial flow compressors, reduced separation control, propellers, windmills, inlets, and diffusers could be made more efficient. Fuel consumption could be lessened. At the heart of (Gad-el-Hak and Bushnell, 1991), fuel consumption could be lessened. At the heart of all of these examples lies the common problem: interaction with and enhancement of the coherent flow structures which exist in the separated flow mixing layer regions produced by the object in question.

This thesis provides initial steps toward that ultimate goal of separation control. Many experiments are presented that were performed on the SM701 airfoil. Detailed objectives for the different experiments that were given in the relevant sections of the thesis prior to discussing the work. A general idea of the objectives follows.

Before separation control can be realized, an extensive study of the viscous flow around the airfoil must be conducted. The locations and extent of laminar, transitional,

1 INTRODUCTION

To determine the flow regions, qualitative fluorescence oil surface flow visualization was first performed and is discussed in Section 4.1. A steady-state heat transfer approach, Section 4.2, was then examined as a means of corroborating the results of the oil flow visualization. The heat transfer approach utilized thermochromic liquid crystals to measure surface temperature distributions. The temperature information allowed convective heat transfer coefficients along the chord of the SM701 airfoil to be calculated under different experimental conditions. The heat transfer results were compared to the oil flow visualization results in an attempt to determine how well the heat transfer method would reveal the location and extent of the viscous flow regions over an airfoil. This line of research was felt to be of value not only to verify oil flow visualization results for the current airfoil, but if successful, to provide a method of flow visualization results for the fluorescent oil technique is not practical. Such situations include spinning turbomachinery and flight testing.

Besides being used to verify the oil flow visualization results and being examined as a flow visualization tool, the heat transfer research was conducted for other reasons not related to the goal of active flow control. First, results of the heat transfer experiments could be used as a benchmark solution in the development of better heat transfer prediction codes. Second, experimental heat transfer information for airfoils in low turbulence environments is not particularly abundant; therefore, the data generated in the was verified numerically by running a boundary layer code as described in Chapter 3.0.

Once the viscous flow regions on the SM701 model were studied, work began on understanding the naturally occurring coherent structures of the separated flow regions for different experimental conditions. Section 5.1 discusses qualitative shear stress tests made using McCroskey type shear stress gauges. It was hoped that the dominant flow instabilities frequencies could be measured near the surface of the airfoil by the shear stress gauges.

turbulent, and separated regions must be accounted for different angles of attack and for different Reynolds numbers.

In Section 4.2, was then examined as a means of corroborating the results of the oil flow visualization. The heat transfer approach utilized thermochromic liquid crystals to measure surface temperature distributions. The temperature information allowed convective heat transfer coefficients along the chord of the SM701 airfoil to be calculated under different experimental conditions. The heat transfer results were compared to the oil flow visualization results in an attempt to determine how well the heat transfer method would reveal the location and extent of the viscous flow regions over an airfoil. This line of research was felt to be of value not only to verify oil flow visualization results for the current airfoil, but if successful, to provide a method of flow visualization results for the fluorescent oil technique is not practical. Such situations include spinning turbomachinery and flight testing.

Besides being used to verify the oil flow visualization results and being examined as a flow visualization tool, the heat transfer research was conducted for other reasons not related to the goal of active flow control. First, results of the heat transfer experiments could be used as a benchmark solution in the development of better heat transfer prediction codes. Second, experimental heat transfer information for airfoils in low turbulence environments is not particularly abundant; therefore, the data generated in the was verified numerically by running a boundary layer code as described in Chapter 3.0.

Once the viscous flow regions on the SM701 model were studied, work began on understanding the naturally occurring coherent structures of the separated flow regions for different experimental conditions. Section 5.1 discusses qualitative shear stress tests made using McCroskey type shear stress gauges. It was hoped that the dominant flow instabilities frequencies could be measured near the surface of the airfoil by the shear stress gauges.

Single sensor hot-wire measurements were then conducted. Boundary layer profiles and wake surveys were examined and analyzed for frequency content. The locations of the hot-wire sensor where the flow instability frequencies were best revealed were also studied. Results of these hot-wire tests are contained in Section 5.2.6.

Once the frequencies of the coherent structures were better understood, a simple test in active control was attempted using a polyvinylidene fluoride (PVDF) piezoelectric film attached to the upper surface of the airfoil. The film could be made to vibrate normal to the surface by application of a square wave voltage signal. Chapter 6.0 discusses these simple tests and offers possible reasons why they were ineffective in controlling the separated flow region on the SM701 airfoil. Conclusions are given in Chapter 7.0. Suggestions are then given in Chapter 8.0 for future heat transfer, shear stress, hot-wire, and active control research.

Because of the complexity of this flow control problem, ultimate success was not achieved in controlling the separated flow on the SM701 airfoil. Due to this shortcoming, an effort was made to provide extensive background information and extreme detail throughout this thesis. After reading this work, any future experimenter should have much clearer idea as to the problems to be solved to make active control a success. The systems (hardware and software) are now in place to quickly study the frequency of naturally occurring coherent structures formed in the separated mixing layer region of any airfoil. Future time can thus be better allocated to the active control problem itself.

This chapter will describe the model that was tested during the course of this study. In addition, the two different experimental facilities that were used will be discussed.

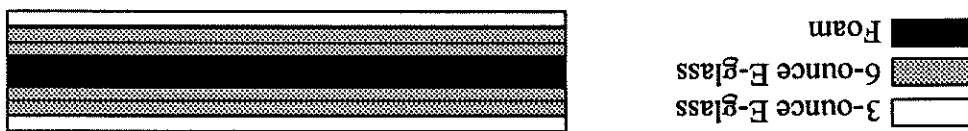
2.1 The Airfoil Definition

The airfoil used for the test model was the SM701, a 16% thick, laminar-flow airfoil designed for World Class sailplanes by Mr. Dan M. Somers of Airfoils, Incorporated and Dr. Mark D. Maughmer of The Pennsylvania State University. The primary objectives of their design were high maximum lift and low profile drag with restrained pitching moment and docile stall characteristics. Details on predicted performance characteristics of the SM701 airfoil (Somers and Maughmer, 1990 and 1991) and experimental verification of those characteristics (Nicks, et. al., 1991 and Althaus and Wurz, 1991) are available. Table 2.1 contains the coordinates of the SM701 airfoil. Figure 2.1 is a sketch of those coordinates.

Upper Surface	Lower Surface	x/c	y/c	x/c	y/c
0.00168	0.00771	0.00016	-0.00212	0.00736	0.01910
0.01701	0.03121	0.01501	-0.01632	0.03055	0.04344
0.04794	0.05534	0.05277	-0.02244	0.06915	0.06648
0.12295	0.08544	0.14575	-0.04101	0.15541	0.09296
0.19133	-0.09914	0.22722	-0.04670	0.23041	0.10397
0.27229	0.10746	0.31929	-0.04943	0.36268	0.11055
0.31654	0.10964	0.36784	-0.04938	0.41019	0.11018
0.45853	0.10853	0.51811	-0.03983	0.50714	0.10557
0.55548	0.10120	0.62191	-0.02623	0.65041	0.08760
0.69676	0.07903	0.77446	-0.00553	0.78466	0.06055
0.74171	0.06990	0.82144	-0.00041	0.78498	0.05125
0.82498	0.04221	0.93768	0.00324	0.86207	0.04221
0.89529	0.03348	0.96489	0.00463	0.86207	0.00567
0.92431	0.02493	0.98462	0.00262	0.94922	0.01669
0.96999	0.00946	1.00000	0.00000	0.98605	0.00405
0.99640	0.00095			0.99640	0.00095
1.00000	0.00000			1.00000	0.00000

Table 2.1: M701 Airfoil Coordinates

Figure 2.2: Sandwich Panel Construction of the Test Model Skin



The test model was fabricated by a group of Penn State aerospace engineering students as part of a senior project. Members of the group were Louis Centolanza, Chris Dunn, Patrick Papay, Duk Park, Robert Smith, and Thomas Thibodeau. The group decided to construct a composite model with a 12 inch chord and a 30 inch span. One-half inch wooden end caps were used to seal the ends of the model, increasing the overall span to 31 inches and the aspect ratio to 2.58.

The group's design included fabricating the upper surface and the lower surface of the model separately and screwing the pieces together with 10 screws along the span of both a main spar and a trailing edge spar. This design feature would allow easy access to the inside of the model during future experimentation.

To fabricate the skin of the model, an existing mold was used. Centolanza et al. used a wet lay-up of E-glass and EPON epoxy resin with EPI-CURE as the hardener. A layer of Owens Corning Foamular 150 foam was then added, followed by two layers of six ounce E-glass and one layer of three ounce E-glass. A layer of Owens Corning Foamular 150 foam was then added to increase the final quality of the composite by pressing the layers together and removing excess voids (Centolanza et al., 1995).

Figure 2.1: SM701 Airfoil Shape

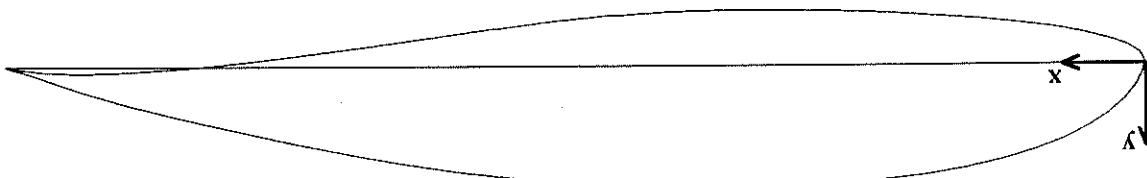
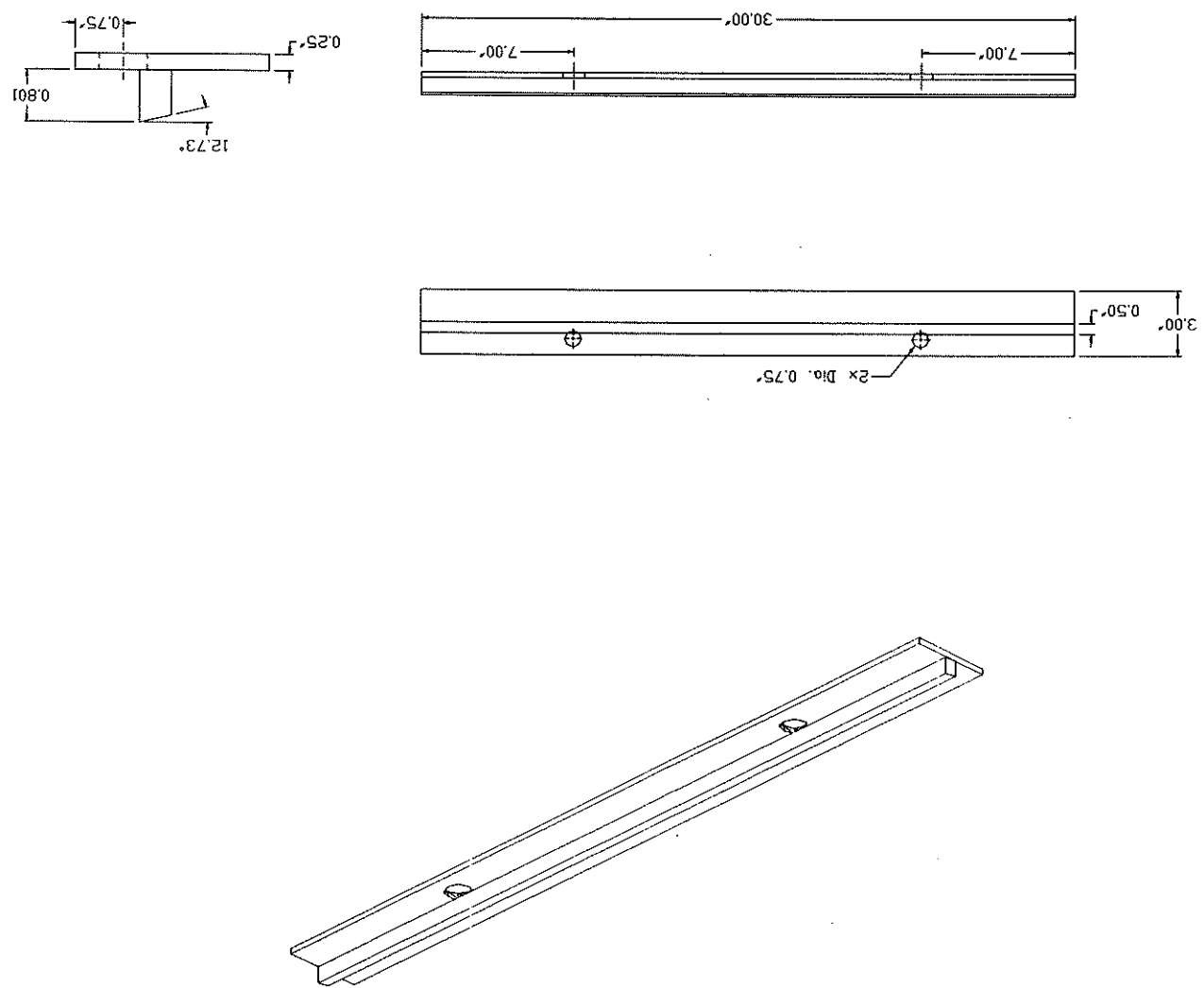


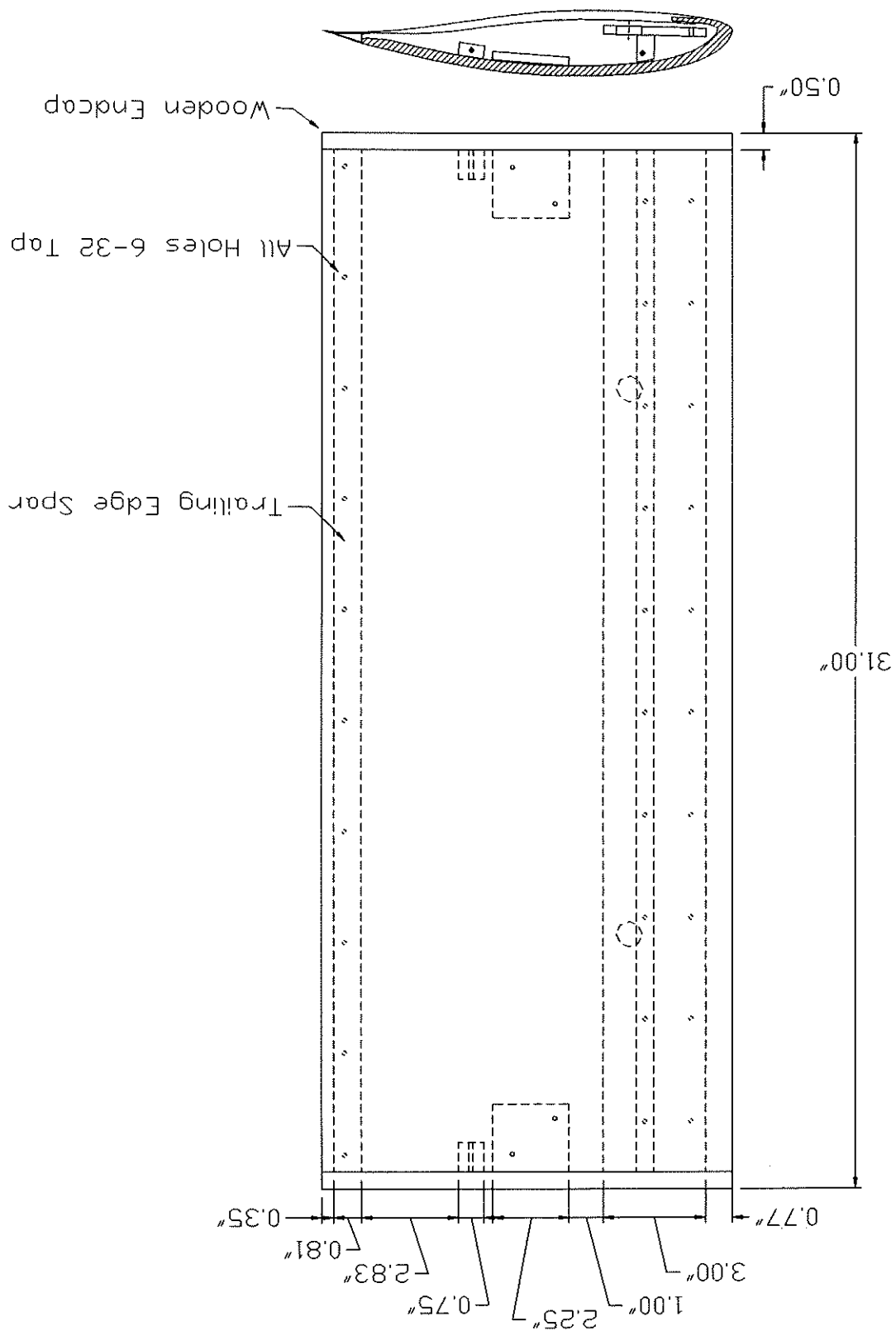
Figure 2.3: Leading Edge Spar of the Airfoil



and 2.4 show the final model.

A main spar and a trailing edge spar were machined from 6061-T6 aluminum. Figures 2.3

Figure 2.4: The Airfoil Model



The test section has a circular cross-section three feet in diameter, and the contraction section accelerates flow through a 4:1 area ratio. Access to the test section is via a side window. To provide turbulence management, a fine cloth and a screen are used at the inlet. This is followed by honeycomb and a series of screens between the inlet and the contraction section. The original design of the tunnel considers the test objects as axisymmetric objects. Hot-wire measurements of the streamwise turbulence intensity in the test section found a representative value of 0.25% over the tunnel operating speed range of zero to 60 f/s (see Figure A.1 in Appendix A for more detailed ASWT

Figure 2.5: Axisymmetric Wind Tunnel (ASWT)

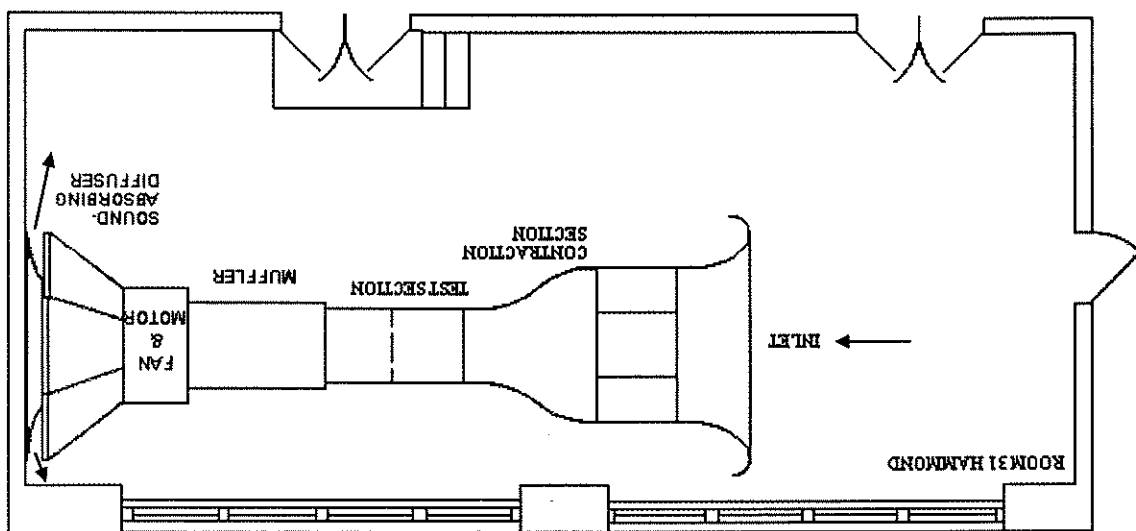
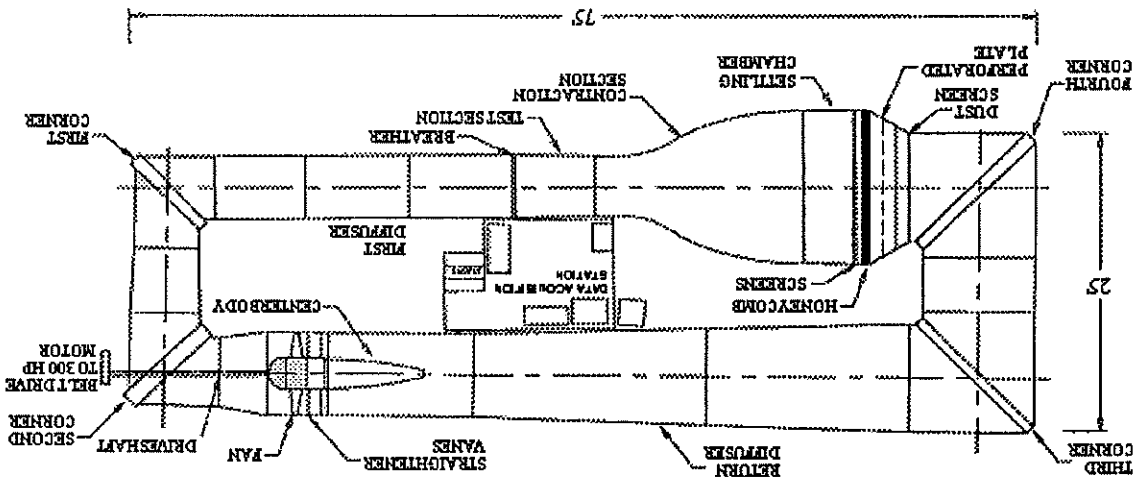


Figure 2.5, is located in 31 Hammond Building at The Pennsylvania State University. The ASWT is an open-return wind tunnel with overall dimensions of 32 x 11 feet. Fiberglass construction was used for the contraction section and test section. The ASWT, fiber-glass construction was used for the contraction section and test section. The ASWT, especially designed acoustic cones protrude into the diffuser section at the flow outlet to provide noise control.

2.2 The Axisymmetric Wind Tunnel (ASWT)

The dimensions at the entrance to the test section are 39.5 inches high by 57.25 inches wide. At the end of the test section, the dimensions are 41 inches high by 59 inches wide. Thus the test section floor and ceiling diffuse at a total angle of 1.2° , and the test section

Figure 2.6: Low-Speed Low-Turbulence Wind Tunnel (LSLT)



The LSLT is a closed-return wind tunnel constructed over a 75×25 foot area. A three-phase, 300 hp electric motor powers the eight-bladed 6.5 foot diameter fan through a belt and drive shaft arrangement. The motor is held at a constant 1100 rpm. An in-line magnetic clutch allows the fan rotation rate to be varied from 150 to 1100 rpm. The LSLT is a closed-return wind tunnel constructed over a 75×25 foot area. A three-phase, 300 hp electric motor powers the eight-bladed 6.5 foot diameter fan through a belt and drive shaft arrangement. The motor is held at a constant 1100 rpm. An in-line magnetic clutch allows the fan rotation rate to be varied from 150 to 1100 rpm.

This facility is given in Brophy, 1994. The most important facility statistics are presented here. It should be noted that Brophy's documentation of the dimensions of the test section used for finite model testing are slightly in error. The correct dimensions are presented in this section.

The LSLT, Figure 2.6, located in 117 Academic Projects Building at The Pennsylvania State University is a high-quality research facility. A detailed description of turbulence intensity information is a high-quality research facility. A two-component strain gauge balance is situated below the test section allowing the measurement of lift and drag.

2.3 The Low-Speed Low-Turbulence Wind Tunnel (LSLT)

Device	Description
Fan	8 blades and 13 stators, max RPM = 1100
Motor	Three phase-300 hp, belt driven
Turming Vanes	First & Second corners Single Wall, 8" chord, 3/16" thick Third & Fourth corners Double Wall, 6" chord, 9/16" max thickness at .5 chord
Dust Screen	46 mesh, .0045" wire diameter, $\beta = .6288$
Perforated Plate	3/8" holes, 3/32" thickness, $\beta = .62$
Settling Chamber Screens	16 mesh, .009" wire diameter, $\beta = .7327$
First Second Third	43 mesh, .005" wire diameter, $\beta = .6162$
Rapid Expansion	46 mesh, .0045" wire diameter, $\beta = .6288$
Contraction Section	9.3:1 Area ratio, tapered corner fillets
Test Section	Closed section w/fillets, 6.1" length, max speed, 220 f/s
First Diffuser	1.9:1 Area ratio
Return Diffuser	2.2:1 Area ratio

Table 2.2: LSITT Description Summary (Brophy, 1994)

Honeycomb and a series of screens are used in the settling chamber for turbulence management. Brophy reports a streamwise turbulence intensity value of less than 0.06% over the operating speed range of the wind tunnel (Brophy, 1994). The tunnel can be used for both finite model testing and infinite airfoil testing. For the former, a six-component pyramidal balance can be used to measure the forces acting upon a model. For the latter, a wake survey system and surface static pressure measurements can be used for determining coefficients of lift, drag, and moment. The contraction section of the LSITT has a 9.3:1 area ratio. Table 2.2 provides many details of the LSITT.

Located at the end of the test section to ensure atmospheric static pressure at that position growing displacement thickness in the test section. A breather slot 1.0 inch wide is side walls diffuse at a total angle of 1.4°. This feature is used to offset the effect of the growing displacement thickness in the test section (Brophy, 1994).

airfoil's surface is then divided. Initially a value of 43 panels was chosen. Calculations for the panel code inputs the desired number of panels from the user into which the

the total number of x/c, y/c points in the input file.

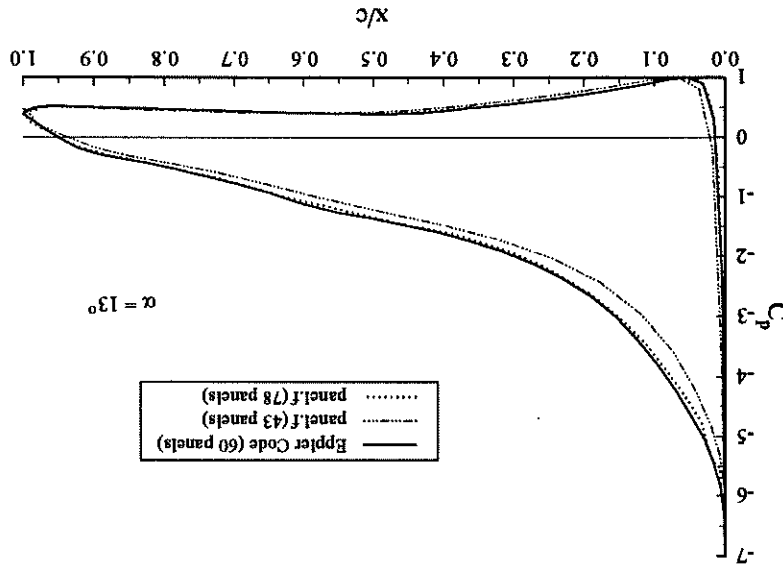
consisting simply of values of 1.0. The first line of the input file should be a value that is 2.1 of Section 2.1. Note that a third column should be included in this input data file repeat this original point. The x/c and y/c points for the SMT01 airfoil were listed in Table continuing along the suction surface back to the original starting point making sure to edge, proceeding along the pressure surface of the airfoil to the leading edge, and to be listed in an input file. The coordinate points should be listed beginning at the trailing edge. The Pennsylvania State University. The code requires the x/c and y/c airfoil coordinates is named Panel.f and was written by Dr. G. S. Dulikravich and several of his students at A two-dimensional panel code was used for the potential flow calculations. The code

3.1 Potential Flow

number of 315,000. process will now be illustrated using the zero degree angle of attack case at a Reynolds 10⁶. Reynolds numbers studied were 315,000 and 750,000. The details of the prediction layer at the airfoil's surface. Predictions were made for three angles of attack: 0, 5, and two-dimensional differential boundary layer code to solve for the details in the boundary experimental configuration, determining the proper boundary conditions, and invoking a basic steps: calculating the potential flow around the SMT01 airfoil for a given airfoil at various angles of attack and two Reynolds numbers. This process involved three convective heat transfer coefficient, h , were computed along the chord of the SMT01 airfoil, two-dimensional theoretical boundary layer predictions were made. Values of the airfoil, to gain insight into the viscous flow behavior on the upper surface of the

3 BOUNDARY LAYER PREDICTIONS ON THE AIRFOIL SECTION SIDE

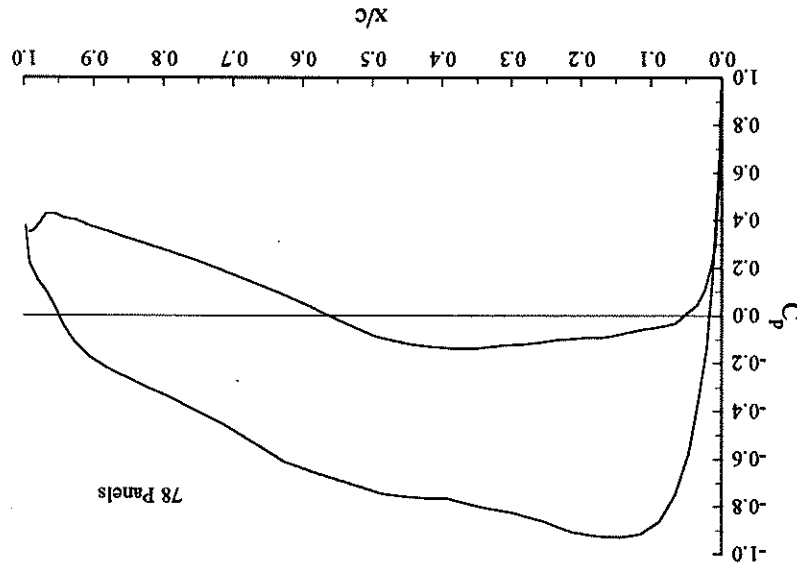
Figure 3.1: Verification of Panel F



Since the accuracy of Panel F was not known, a C_L comparison was made to the potential flow results obtained by Mr. Dan M. Somers and Dr. Mark D. Maugehamer who used the well-known and well-tested Eppler Airfoil Program System for their calculations on the SMT01 airfoil. The Eppler results are trusted since the Eppler Airfoil Program system has been used to design and analyze many other airfoils with experiments verifying the results (Somers and Maugehamer, 1990). Somers' and Maugehamer's C_L predictions are tabulated in their report entitled "The SMT01 Airfoil" (Somers and Maugehamer, 1990) and are plotted for an angle of attack of 13° in Figure 3.1. Results of Panel F for the same angle of attack are plotted for comparison.

$$C_L = \frac{2}{\rho U_\infty^2} \cdot \frac{dp}{dx} \quad (3.1)$$

Figure 3.2: Potential Flow C_p Distribution for $\alpha = 0^\circ$



results are plotted in Figure 3.2.

The code Panel F was then run for a zero degree angle of attack. Pressure coefficient theoretical study.

Two other angles of attack were analyzed and compared to Eppler code results. These angles were 6° and 11° . Good agreement was again obtained. Because of these comparisons, Panel F was felt to be trustworthy for use in the prediction of boundary layer characteristics including convective heat transfer coefficients, the ultimate goal of this study.

obtained for the agreement between Panel F results and those of the Eppler code.

Panel F while increasing the number of panels from 43 until no further improvement was predicted. A value of 78 for the number of panels was obtained by repeatedly running

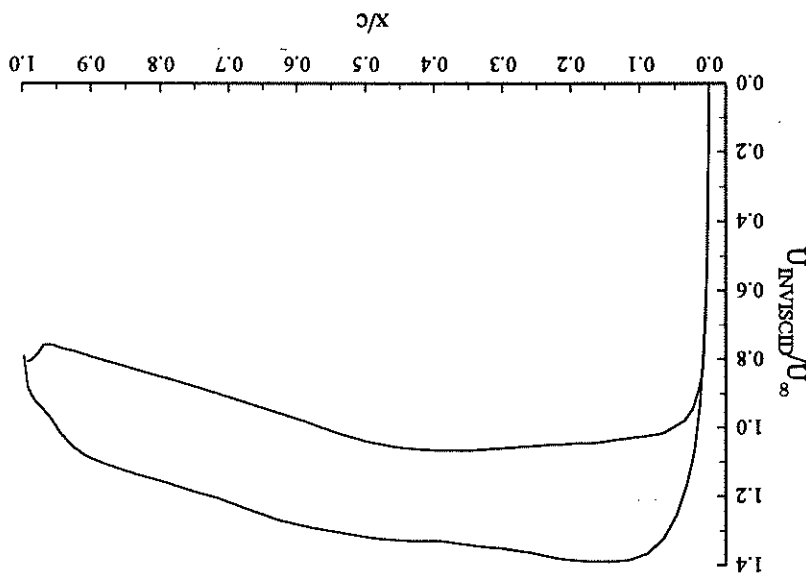
code, Panel F was re-run with the number of panels increased to 78. These results are also shown in Figure 3.1. Notice the good agreement between Panel F and Eppler C_p

surface of the airfoil. Because of the poor agreement between Panel F and the Eppler code, Panel F was re-run with the number of panels increased to 78. These results are also

Note that the C_p prediction made by Panel F using 43 panels is poor along the upper

From this nondimensional velocity distribution, the stagnation point can be located at the x/c location at which $U_{\text{Nondim}} / U_\infty$ goes to zero. Referring to Figure 3.3, the stagnation point for this case is estimated to occur at $x/c = 0.0$. With knowledge of the stagnation point location, the calculated nondimensional inviscid velocity distribution about the SM701 airfoil may be translated into the boundary layer coordinate system which begins at the stagnation point and proceeds along the arc length of the upper surface of the airfoil. See Figure 3.4.

Figure 3.3: Nondimensional Velocity Distribution for $\alpha = 0^\circ$



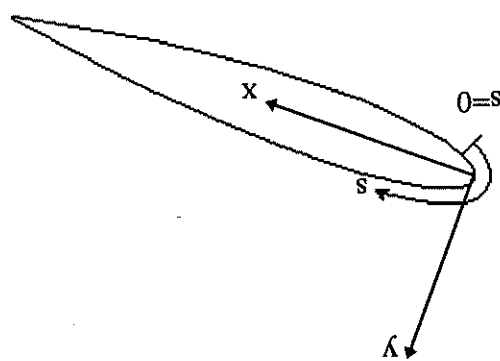
$$\frac{U_{\text{Nondim}}}{U_\infty} = \sqrt{1 - C_p} \quad (3.2)$$

are seen in Figure 3.3.

These C_p values were converted to nondimensional velocity values by using equation 3.2 derived from Bernoulli's equation for steady, incompressible, irrotational flow. Results

The calculated inviscid velocity distribution will hereafter be referred to as the "outer flow velocity distribution" when presented in the boundary layer coordinate system. In addition, the variable U_{inviscid} will be replaced by U . This outer flow velocity distribution at the outer edge of the boundary layer code as the boundary condition velocity distribution will be used by the boundary layer code. The outer flow velocity values at the outer edge of the boundary layer. The outer flow velocity distribution calculated for an angle of attack of zero degrees is shown in Figure 3.5.

Figure 3.4: The Boundary Layer (B.L.) Coordinate System



$$(3.5) \quad S + \left[\left(\frac{\partial}{\partial x} + \frac{\partial V}{\partial x} \right) \frac{\partial}{\partial x} - \frac{g_0 f}{U^2} \left(\frac{\partial}{\partial x} \right)^2 \right] = 0$$

$$(3.4) \quad U \frac{\partial U}{\partial x} + V \frac{\partial V}{\partial x} = U \frac{\partial}{\partial x} \left[\frac{\partial}{\partial x} - \frac{g_0 f}{U^2} \right]$$

$$(3.3) \quad \frac{\partial U}{\partial x} + \frac{\partial V}{\partial x} = 0$$

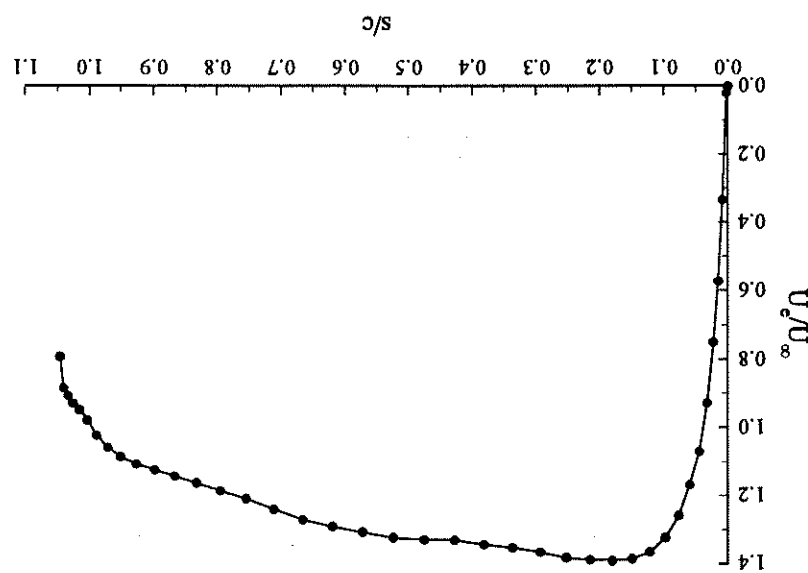
(Crawford and Kays, 1975).

3.4, and 3.5, respectively, in the boundary layer coordinate system. Gravity is neglected incompressible, boundary layer form of these equations are presented as equations 3.3, the continuity, s-momentum, and energy equations simultaneously. The time-average, calculating the boundary layer development at the surface of an airfoil requires solving

3.2 Boundary Conditions

3.2.1 Initial Conditions

Figure 3.5: Outer Flow Velocity Distribution in B.L. Coordinate System for $\alpha = 0^\circ$



The dependent variables in these equations are U , V , $u_{\bar{V}}$, I^* , and $i_{\bar{V}}$. However, modeling the Reynolds stress term and the $i_{\bar{V}}V$ term reduces the dependent variables to the mean velocities (U , V) and the stagnation enthalpy (I^*). Equations 3.3 to 3.5 then reveal the necessary boundary conditions. From the continuity equation it is seen that U must be specified at a given s location for all y locations; this requires specification of a *startling velocity profile*. Continuity also reveals that V must be specified at a given y location for all s locations; the no-slip boundary condition can be used to satisfy this requirement.

The s -momentum equation adds to the current boundary conditions since it contains a second order partial derivative of U with respect to y . Thus U must be specified at two y locations for all s locations. These boundary conditions may be expressed mathematically as

$$\lim_{y \rightarrow 0^+} U(s, y) = U^*(s) \quad \text{edge condition} \quad (3.7)$$

$$U(s, 0) = 0 \quad \text{no-slip}$$

The values of $U^*(s)$, containing pressure gradient information outside the boundary layer, were determined previously in Section 3.1 by use of a panel code.

The energy equation reveals the required boundary conditions on stagnation enthalpy. The first term reveals that I^* must be specified at a given s location for all y locations. This requires a *startling profile for stagnation enthalpy*. The energy equation also shows through its second partial derivative of I^* with respect to y that I^* must be specified at two y locations for all s locations. This is handled by calculating the stagnation enthalpy at the airfoil surface temperature and boundary layer edge temperature will be functions of s , but based on the respective average absolute temperatures. This is an approximation since the airfoil surface temperature and boundary layer edge of the boundary layer ($y = 0^+$)

at the airfoil surface ($y = 0$) and also at the edge of the boundary layer ($y = \delta^+$)

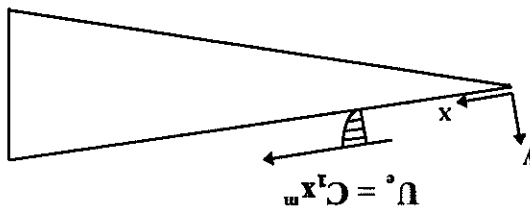
$$\lim_{y \rightarrow 0^+} U(s, y) = U^*(s) \quad \text{edge condition} \quad (3.7)$$

$$U(s, 0) = 0 \quad \text{no-slip}$$

The dependent variables in these equations are U , V , $u_{\bar{V}}$, I^* , and $i_{\bar{V}}$. However, enthalpy boundary conditions.

The similarity solution process for this form of $U^*(x)$ is commonly referred to as the Falkner-Skan wedge flow solution since the assumed velocity distribution can be shown to come directly from the complex potential function $w(z) = Az^{m+1}$ for flow about a two-dimensional wedge; this complex potential function represents the inviscid velocity distribution at the wedge surface with the $x = 0$ point at the wedge vertex. It should be noted that if $m = 0$, the complex potential and assumed velocity distribution revert to Falkner-Skan wedge flow solution since the assumed velocity distribution can be shown to

Figure 3.6: Setup for Falkner-Skan Wedge Flow Solution



$$U^*(x) = C_1 x^m \quad (3.8)$$

Refer also to Figure 3.6.

A simple linear starting profile for U could have been specified and used as a boundary condition in the solution of the continuity, s -momentum, and energy equations (as suggested by Crawford and Kay, 1975). However, a more correct method was chosen to calculate a velocity profile which could be used as the starting profile. This involved a similarity solution of the continuity and x -momentum boundary layer equations where the velocity at the edge of the boundary layer was assumed to be of the form of equation 3.8. Velocity at the edge of the boundary layer was assumed to be of the form of equation 3.8.

3.2.2 Starting Velocity Profile

From this discussion the only unresolved boundary conditions are the starting profiles for U and I^* . The starting profile for stagnation enthalpy I^* is simply modeled as varying linearly between the airfoil surface value of stagnation enthalpy and the boundary layer edge value (as suggested by Crawford and Kay, 1975), both of which are specified as constants in s as previously discussed. The starting velocity profile is somewhat more complex and is now discussed in detail.

$$f''' + \alpha f'' + f' [1 - (f)^2] = 0 \quad (3.14)$$

similarity equation is obtained

Substituting equations 3.11 to 3.13 into the x-momentum equation 3.10, the following

$$V = U \frac{dx}{ds} \frac{df}{ds} - \frac{dx}{ds} (U^2 g) \quad (3.13)$$

equation becomes

With these substitutions and after some rearranging and integration by parts, the continuity

$$\eta = \frac{g(x)}{\gamma} \quad (3.12)$$

$$U = U(x, f, \eta) \quad (3.11)$$

substitutions are made.

Making the similarity assumption that the two dependent variables (U, V) which are functions of the two independent variables (x, y) can be combined into a single dependent variable (f) which is a function of a single independent variable (η), the following

$$\frac{\partial U}{\partial x} + V \frac{\partial U}{\partial \eta} = U \frac{\partial V}{\partial x} + U^2 \frac{\partial f}{\partial \eta} \quad (3.10)$$

$$0 = \frac{\partial V}{\partial x} + \frac{\partial f}{\partial \eta} \quad (3.9)$$

neglected.

The equations to be solved for this similarity solution are the two-dimensional, steady, incompressible continuity and x-momentum boundary layer equations. Gravity is

and one is used to generate a starting profile.

forms for flow over a flat plate. If $m = 1$, the complex potential and velocity distribution represent two-dimensional stagnation point flow. The physical case of flow near the dimensionless stagnation point on an airfoil falls between the case of a flat plate and that of a two-dimensional stagnation point. Thus, the case of wedge flow where m falls between zero and one is used to generate a starting profile.

See Figure 3.7.

attack, these velocity values were calculated via a panel code as explained in Section 3.1. $U_\infty(x)/U_\infty$ outer flow velocity values near the stagnation point at a zero degree angle of attack was obtained by fitting an exponential curve through the first few terms of the equation. The value of m that was used was first broken into three first order differential equations. The value of m that was used was a fourth order Runge-Kutta code was used to solve the similarity equation 3.17 after it starting velocity profile in the solution of equations 3.3, 3.4, and 3.5 of Section 3.2.1. A four-dimensionalized by using equations 3.11, 3.12, and 3.18 to obtain $U(x)$ for use as a boundary conditions (equations 3.19 to 3.21) will yield a profile $f_r(\eta)$. This profile can be dimensionless $f_r(\infty) = 1$, $f_r(0) = 0$, and $f_r'(0) = 0$. It should be emphasized now that the similarity equation 3.17 is a combination of the continuity and x -momentum boundary layer equations. Solution of equation 3.17 with the boundary conditions given by

$$f_r(\infty) = 1 \quad (3.21)$$

$$f_r(0) = 0 \quad (3.20)$$

$$f_r'(0) = 0 \quad (3.19)$$

The boundary conditions are given by

$$\frac{d}{dx} \left[\frac{U_\infty}{\sqrt{\alpha x}} \right] = f_r(x) g \quad (3.18)$$

recalling that $U_\infty(x) = C_1 x^m$

$$f_r''' + \frac{2}{1} (m+1) f_r'' + m \left[1 - (f_r')^2 \right] = 0 \quad (3.17)$$

Using equations 3.15 and 3.16, the similarity equation becomes

$$g = m \quad (3.16)$$

$$a = \frac{2}{1} (m+1) \quad (3.15)$$

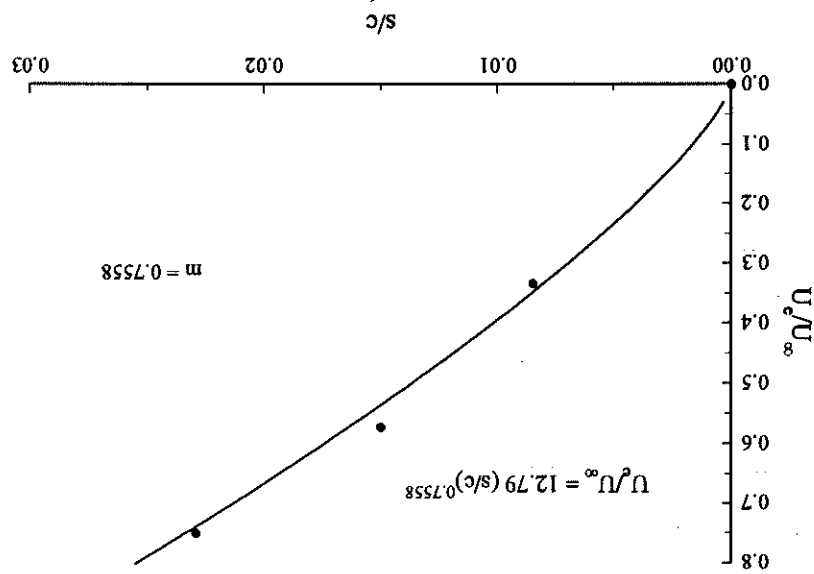
substitution for the coefficients a and g .

flow, equation 3.8, and assuming $g(x) = \sqrt{\frac{U_\infty}{\alpha x}}$, the following results are obtained via

where $a = \frac{V}{g} \frac{dx}{dU_\infty}(U_\infty g)$ and $g = \frac{V}{g^2} \frac{dU_\infty}{dx}$. Taking the assumed form of $U_\infty(x)$ for wedge

Using the value for m determined in Figure 3.7, solution to the similarity equation 3.17 yields the following similarity profile in Figure 3.8.

Figure 3.7: Determination of m for $\alpha = 0^\circ$



obtained during experimentation as will be discussed in Section 4.2.

experimental data listed in the table (U_{AVG} , P_{AVG} , T_{wAVG} , and $T_{\infty AVG}$) were the zero degree angle of attack case, along with data for all other experimental runs. The Table 3.1 summarizes the information used to calculate the dimensional starting profile for calculating using Sutherland's law and experimentally measured free stream temperatures.

in Section 3.1, and $\nu = \frac{\rho}{H}$ is obtained from experimental data. The value of viscosity is the experimental runs at $\alpha = 0^\circ$. $U_e(s)$ and s are obtained from the panel code discussed Finally, to dimensionize this profile, values of $U_e(s)$, ν , and s must be known for

Figure 3.8: Falkner-Skan Similarity Profile for SM701 at $\alpha = 0^\circ$

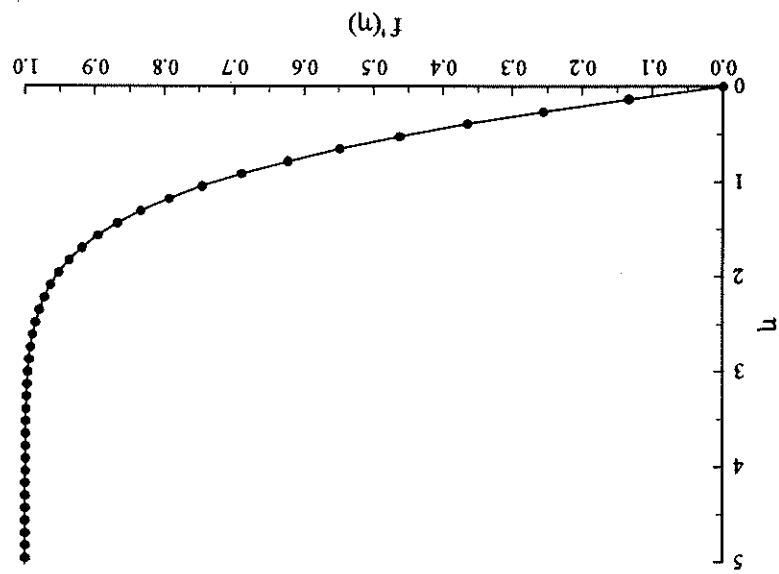


Table 3.1: Information Required for Dimensional Starting Profile Calculations

α (deg.)	Re	Data Determined Through Experimentation					From Panel Code	
		μ_{AVG} $(N \cdot s/m^2)$	ρ_{AVG} (kg/m^3)	$U_{\infty AVG}$ (m/s)	$T_{wall AVG}$ (K)	$T_{\infty AVG}$ (K)	$S_{first node after stagnation point}$ (m)	$U_e \left(\frac{S_{first node after stagnation point}}{U_{\infty}} \right)$
0	315,000	1.8282x10 ⁻⁵	1.174	15.87	303.15	295.10	0.000835	0.020347
0	750,000	1.8851x10 ⁻⁵	1.120	40.48	316.15	304.41	0.000835	0.020347
5	315,000	1.8660x10 ⁻⁵	1.151	16.28	316.15	296.28	0.002159	0.297676
5	750,000	1.8868x10 ⁻⁵	1.117	40.78	316.15	305.29	0.002159	0.297676
10	315,000	1.8652x10 ⁻⁵	1.152	16.31	316.15	295.99	0.001326	0.032894
10	750,000	1.8872x10 ⁻⁵	1.123	40.61	316.15	305.35	0.001326	0.032894
15	750,000	1.8886x10 ⁻⁵	1.125	40.72	316.15	306.07	0.003467	0.052077
18	750,000	1.8882x10 ⁻⁵	1.122	40.79	316.15	305.91	0.005771	0.101089
20	750,000	1.8844x10 ⁻⁵	1.124	40.56	316.15	304.31	0.005522	0.077840
							3.157173	

$$l = \kappa D \quad \text{viscous sublayer} \quad (3.25)$$

$$l = \kappa y \quad \text{near wall region} \quad (3.24)$$

The mixing length, l , is modeled as

$$\epsilon_m = l^2 \left| \frac{\partial U}{\partial x} \right|$$

The Prandtl mixing-length model is used to model the eddy diffusivity.

$$-\underline{u'_v} = \epsilon_m \frac{\partial}{\partial x} = \frac{\rho}{H'} \frac{\partial \phi}{\partial x} \quad (3.22)$$

The eddy diffusivity concept is used to model the Reynolds stresses.

STAN5 is able to solve both laminar and turbulent boundary layers and includes a provision to allow transition based on a momentum thickness Reynolds number criterion (Crawford and Kay, 1975). Viscous dissipation in the energy equation is included, and provision to allow transition based on a momentum thickness Reynolds number criterion to allow transition based on a momentum thickness Reynolds number criterion (Crawford and Kay, 1975).

equations have already been presented as equations 3 to 5 in Section 3.2.1. STAN5, a boundary layer code developed at Stanford University, was used. STAN5, developed from the Patankar/Spalding program which is discussed in their book (Patankar and Spalding, 1967), is "a program for numerical computation of two-dimensional internal/exterior boundary layer flows" (Crawford and Kay, 1975). These flows are described by the parabolic boundary layer equations which include the continuity, momentum, and stagnation enthalpy equations. The time averaged form of these equations have already been presented as equations 3 to 5 in Section 3.2.1.

Now that all necessary boundary conditions have been set for the solution of the

3.3 The Boundary Layer Code STAN5

starting profile is obtained to be used as a boundary condition in the solution of equations 3.3, 3.4, and 3.5. All necessary boundary conditions have now been specified, and solution to the governing equations may now continue.

Using equations 3.11, 3.12, and 3.18 and substituting $x = s_{\text{first node after}}^{s_{\text{stagnation point}}}$, a dimensional

An input file was then created for STAN5. The starting profile required by the input file was calculated by the method described in Section 3.2 with $m = 0$. STAN5 was run, and the calculated skin friction coefficient distribution is presented in Figure 3.9.

$$\rho = 1.225 \frac{m^3}{kg} \quad (3.27)$$

$$\mu = 1.8 \times 10^{-5} \frac{m^2}{N \cdot s}$$

$$U_e = 10 \frac{m}{s}$$

$$C_f = \frac{0.664}{\frac{\sqrt{U_e x}}{m}} \quad (3.26)$$

over a flat plate with the following test values.

Before using STAN5 to perform calculations on the SM701 airfoil, a simple test case was first run to verify that STAN5 was functioning properly. This test was deemed important since the version of STAN5 that was used was slightly modified from the original STAN5 code to run on a PC instead of on a Digital/VAX computer. The well-known Blasius flat plate equation for skin friction was used to calculate the C_f distribution over a flat plate with the following test values.

In the actual input file,

To execute STAN5 an input file must first be created. The STAN5 manual (Crawford and Keys, 1975) contains details regarding the construction of the input file. Table B.2 in Appendix B lists the input file used for the SM701 airfoil at a zero degree angle of attack and a Reynolds number of 315,000. The bold faced comments in the table do not appear and a Reynolds number of 315,000. The bold faced comments in the table do not appear

scheme to solve the continuity, s -momentum, and energy equations simultaneously. boundary condition at the edge of the boundary layer and invokes a finite-differencing damping function. STAN5 uses freestream velocity $U_e(s)$ rather than pressure as the where k is the von Karman constant ($k = 0.41$), and D is the exponential Van Driest

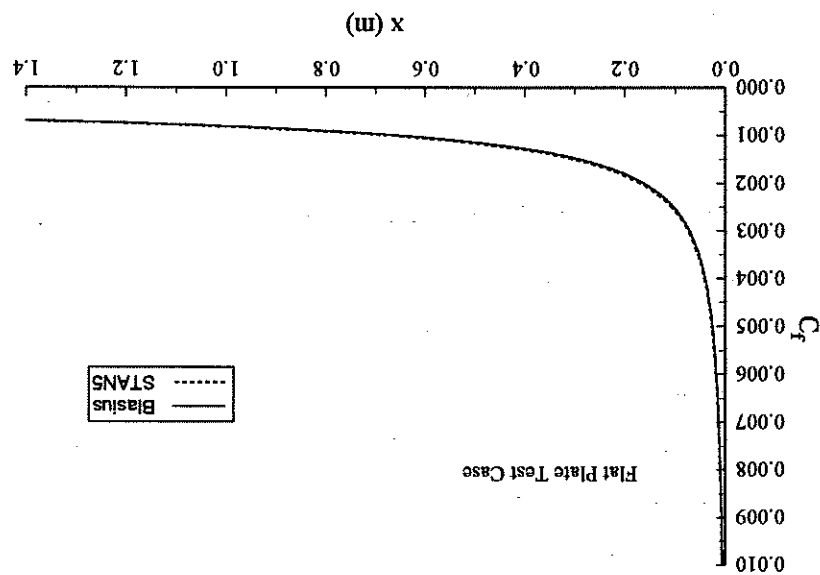
any of the points calculated.

The results can be seen in Figure 3.10. The δ_{99} values never differ by more than 3% for

$$\delta_{99} = 4.92 \sqrt{\frac{U_e}{Vx}} \quad (3.28)$$

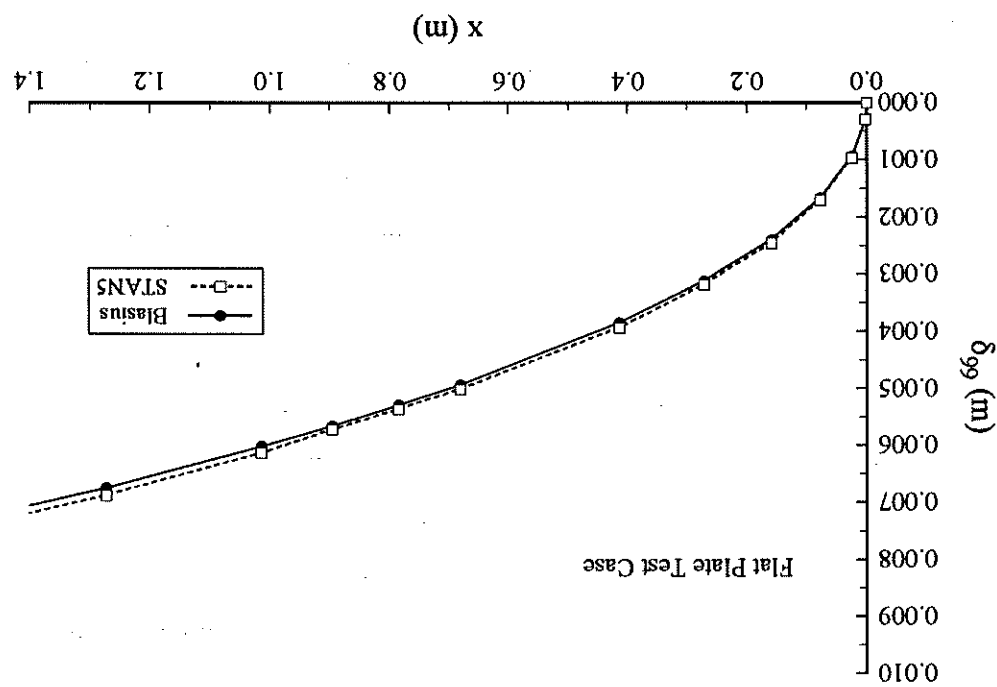
from the following equation. This equation also stems from the classical Blasius solution, calculated by STAN5 along the flat plate and compared to the analytically predicted values further check, the 99% boundary layer thickness was also obtained from velocity profiles as can be seen, STAN5 results agree well with the analytic Blasius solution. As a

Figure 3.9: Comparison of STAN5 Cf, Results and Blasius Solution



along with the experimental heat transfer results. From these two checks (C_f and δ_g), the STAN5 code appeared to be functioning properly. Because of the confidence in the code, it was then run for the cases of interest involving the SM701 airfoil. These numerical predictions are presented in Section 4.2.16 along with the experimental heat transfer results.

Figure 3.10: Comparison of STAN5 δ_g Results and Blasius Solution



This chapter discusses the experimentation that was performed to gain an understanding of the viscous flowfield over the SM701 airfoil under various experimental conditions. The existence and locations of the laminar, transitional, turbulent, and separated/reattached regions on the airfoil are explored using two different methods: fluorescent oil flow visualization and liquid crystal thermography.

4.1 Fluorescent Oil Flow Visualization

The following sections describe the fluorescent oil flow visualization tests and present qualitative results as a series of pictures for experiments performed in Penn State's Axiymmetric Wind Tunnel (ASWT) and Low-Speed Low-Turbulence Wind Tunnel (LSLT) at two different Reynolds numbers and several different angles of attack. Models tested were two-dimensional. The two Reynolds numbers were 315,000 and 750,000. ASWT results are only for a Reynolds number of 315,000 due to the lower maximum flow speed of that facility. Angles of attack studied were 0, 5, 10, 15, 18, and 20°. Angle of attack is referenced with respect to the chord of the airfoil. LSLT tests include a heater strip located on the surface of the model. This heater strip will be discussed in detail in Section 4.2.

The objective of the conventional fluorescent oil flow visualization tests is to determine the locations and extent of the various flow regions on the upper surface of the SM701 airfoil under different experimental conditions. These tests will provide a baseline with which to compare the liquid crystal thermography results of Section 4.2.

4.1.1 Oil Flow Visualization Objective

All lights illuminating the model were replaced with ultraviolet "black lights." Three mixtures of aviation oil (Shell Aeroshell W 100 ashless dispersant SAE 50) and kerosene were prepared.

4.1.2 Oil Flow Visualization Procedure

All lights illuminating the model were replaced with ultraviolet "black lights." Three mixtures of aviation oil (Shell Aeroshell W 100 ashless dispersant SAE 50) and kerosene

- A. "The oil follows the boundary layer surface streamlines except near separation where it tends to form an envelope upstream of the true separation envelope. This early indication of separation is ... less marked for turbulent than laminar layers. The distance by which separation is apparently altered depends on the oil thickness, and the model size, but it is independent of the oil viscosity ..." (Squire 1962)
- B. "The effect of the oil flow on the motion of the boundary layer ... is very small in most practical cases but increases as the oil viscosity decreases." (Squire 1962)
- C. "Results at low Reynolds number should be treated with caution as transition could be erroneously interpreted as separation." (Squire 1962)

C. 1:4
B. 1:3
A. 1:2 (oil:kerosene)

Figure 4.1 compares results from both facilities for $\alpha = 0^\circ$. Figure 4.1a is of poorer quality than Figures 4.1b and 4.1c due to less available "black" light in the test section of the ASWT. The ASWT results indicate a laminar separation bubble existing on the upper surface between 59-75% chord for $Re = 315,000$. At the same Reynolds number, Figure 4.1b shows that a laminar separation bubble exists between 57-75% in the LSST. At $Re = 750,000$, Figure 4.1c shows that the laminar separation bubble has shifted forward and exists from 61-68%. The upper edge of the heater strip is seen to be affecting the downward flow of the oil due to gravity. Flow is seen to be very two-dimensional for the test conditions in Figure 4.1.

Figure 4.2 presents oil flow visualization results for $\alpha = 5^\circ$. In Figure 4.2a, a weak laminar separation bubble is seen between 35-50% in the ASWT at $Re = 315,000$. It is difficult to accurately pin point the location of this weak bubble since the points of laminar separation and flow reattachment are somewhat ambiguous. Figure 4.2b indicates a more distinct laminar separation bubble from 29-45% in the LSST at $Re = 315,000$. Turbulent separation is also seen in Figure 4.2b at approximately 97%. For $Re = 750,000$, Figure 4.2c is somewhat ambiguous. Either a weak laminar separation bubble exists from 21-42% or natural transition is occurring. Turbulent separation is at 95%. Two- dimensional flow is again seen to be a prominent feature for the test conditions of Figure 4.2. Figure 4.3 contains results for $\alpha = 10^\circ$. The ASWT results in Figure 4.3a indicate a laminar separation bubble from 12-25% and turbulent separation at 85%. Although visible features are not very evident in the reproduced photograph that is Figure 4.3a. In the LSST at the same Reynolds number, Figure 4.3b shows the laminar separation bubble is from 11-23% with turbulent separation at 86%. In Figure 4.3c for $Re = 750,000$, the laminar separation bubble has shortened and is located from 12-18% with turbulent separation at 83%. The flow patterns seen on the upper surface of the airfoil remain two-dimensional for the test conditions in these figures, especially near the heater strip.

4.1.3 Oil Flow Visualization Results

Figure 4.1a: $\alpha = 0^\circ$, $Re = 315,000$
ASWT

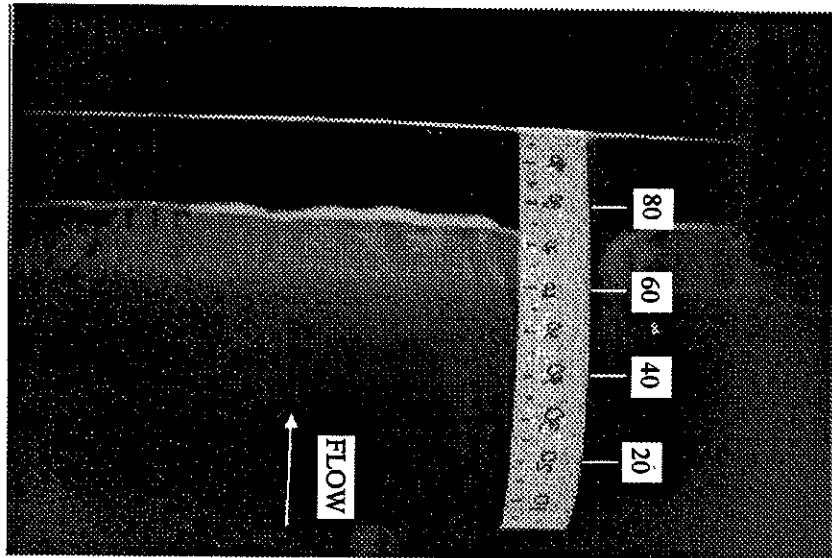


Figure 4.1b: $\alpha = 0^\circ$, $Re = 315,000$
LSLT

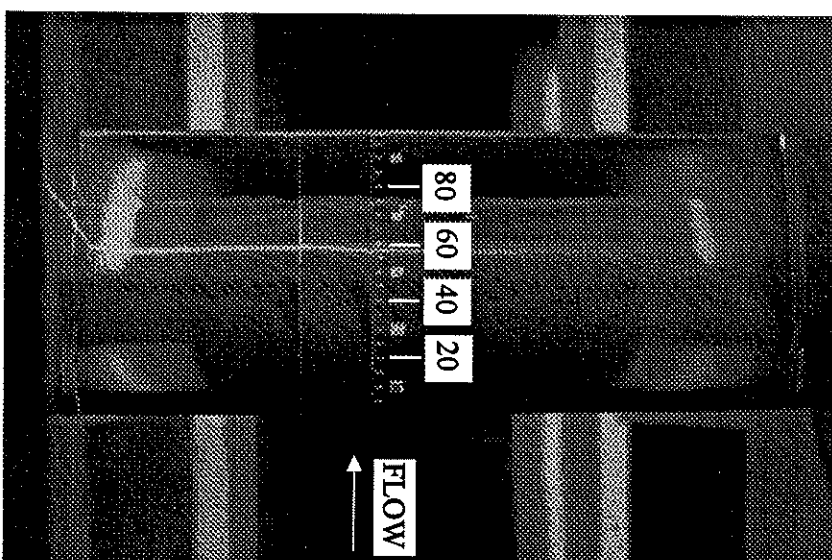


Figure 4.1c: $\alpha = 0^\circ$, $Re = 750,000$
LSLT

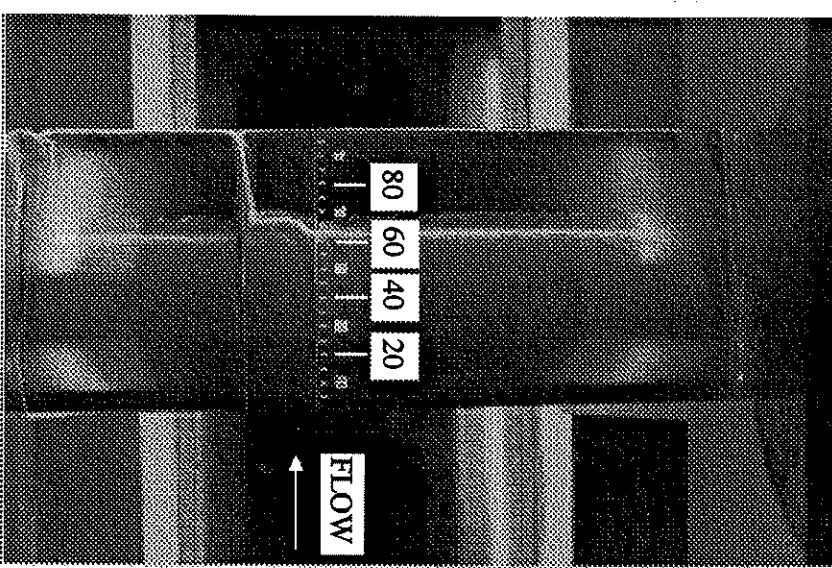


Figure 4.2a: $\alpha = 5^\circ$, $Re = 315,000$
ASWT

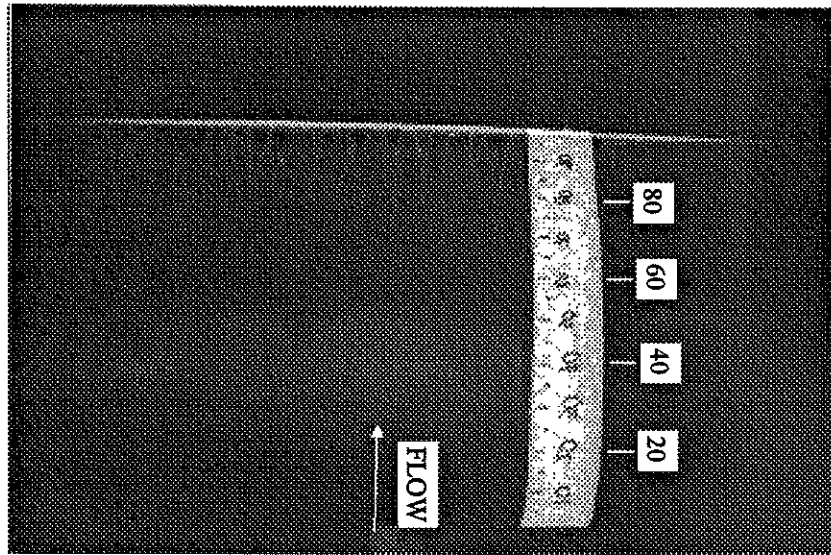


Figure 4.2b: $\alpha = 5^\circ$, $Re = 315,000$
LSLT

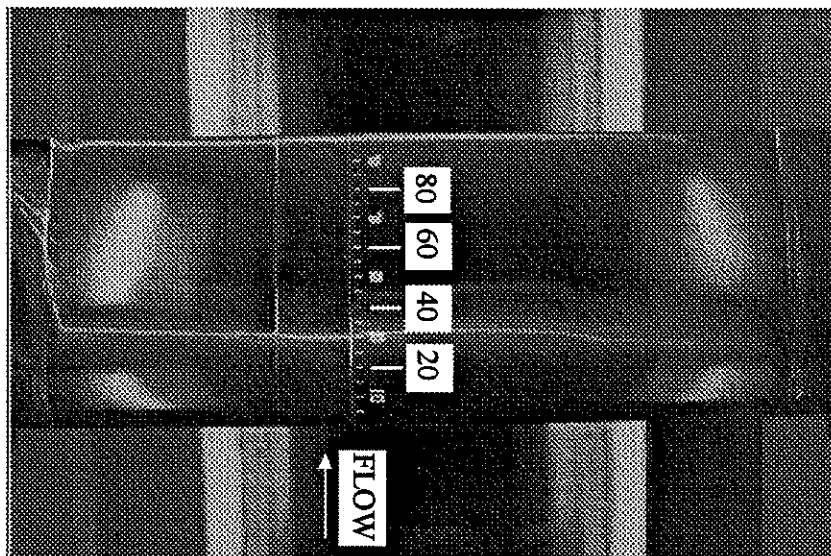
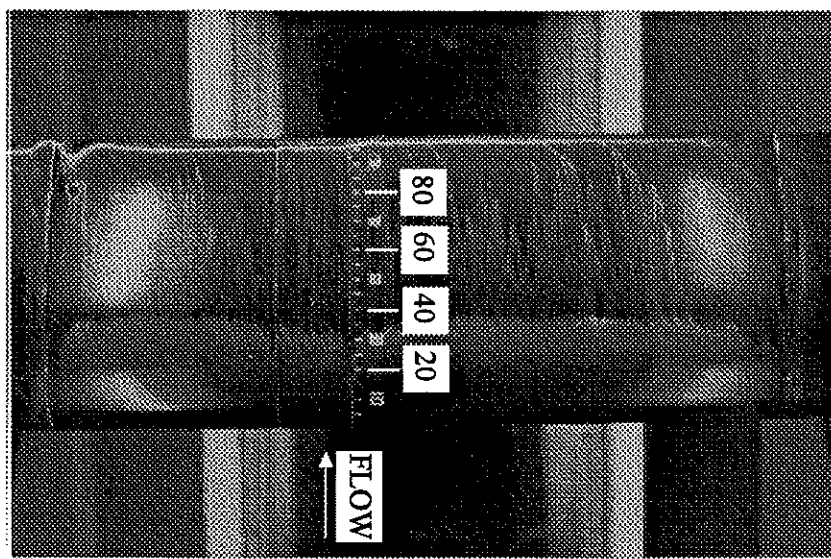


Figure 4.2c: $\alpha = 5^\circ$, $Re = 750,000$
LSLT



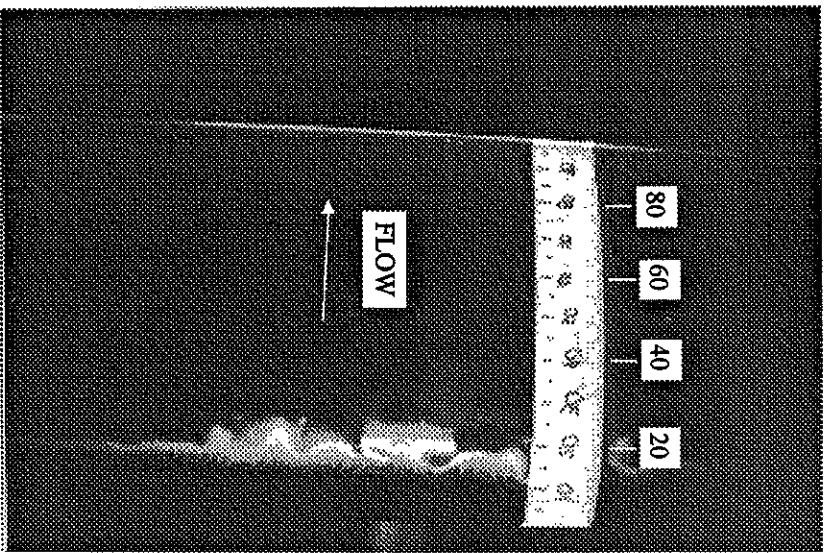


Figure 4.3a: $\alpha = 10^\circ$, $Re = 315,000$
ASWT

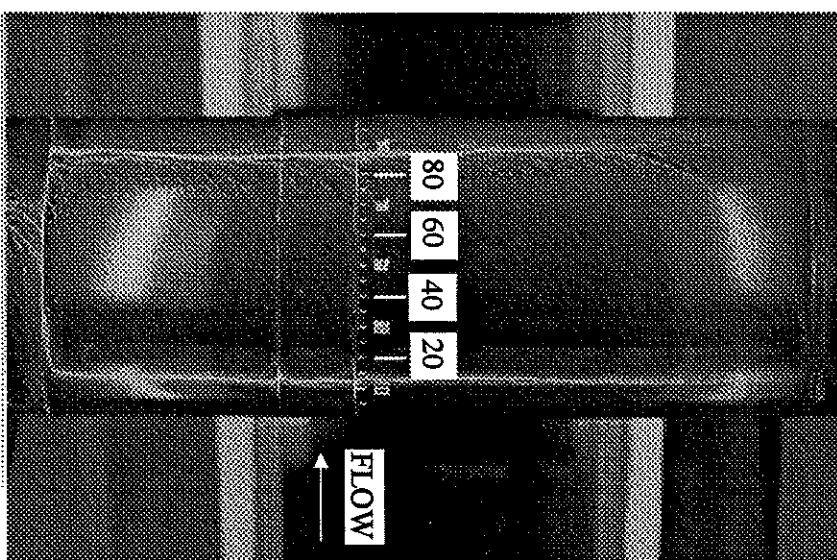


Figure 4.3b: $\alpha = 10^\circ$, $Re = 315,000$
LSLT

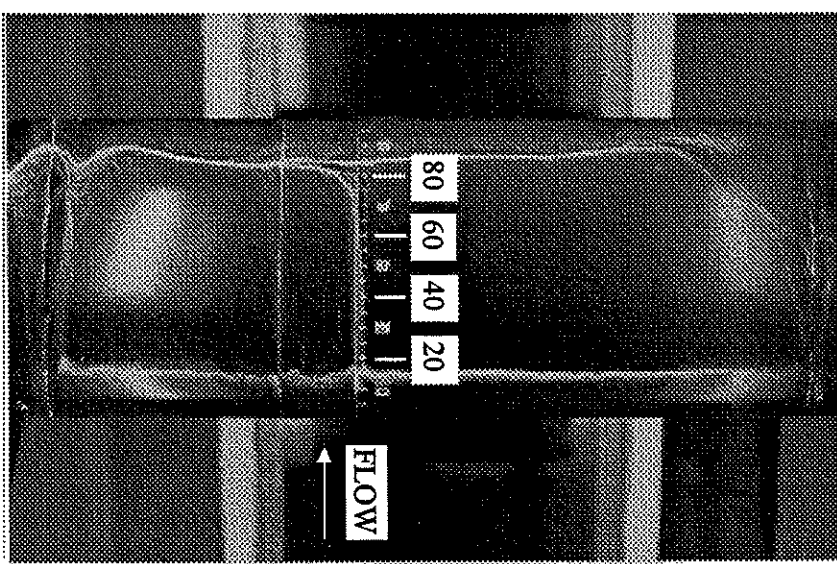


Figure 4.3c: $\alpha = 10^\circ$, $Re = 750,000$
LSLT

Figure 4.4a: $\alpha = 15^\circ$, $Re = 315,000$
ASWT

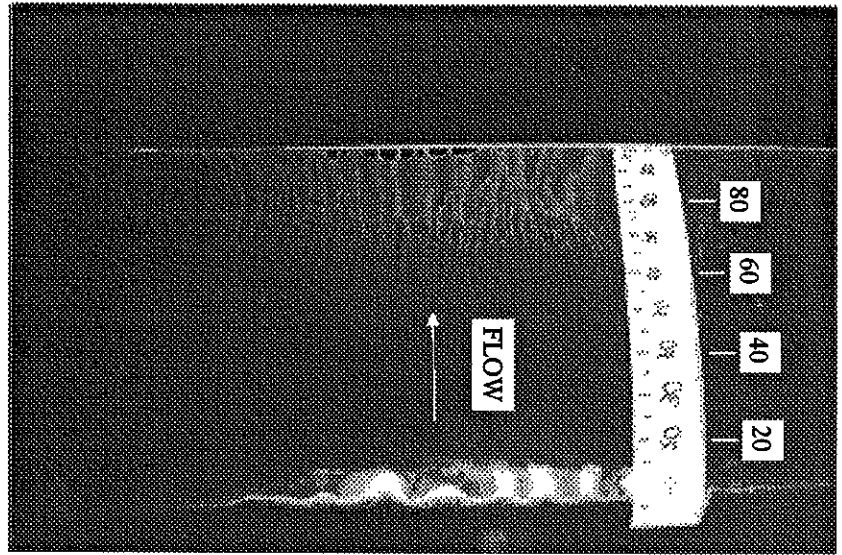


Figure 4.4b: $\alpha = 15^\circ$, $Re = 315,000$
LSLT

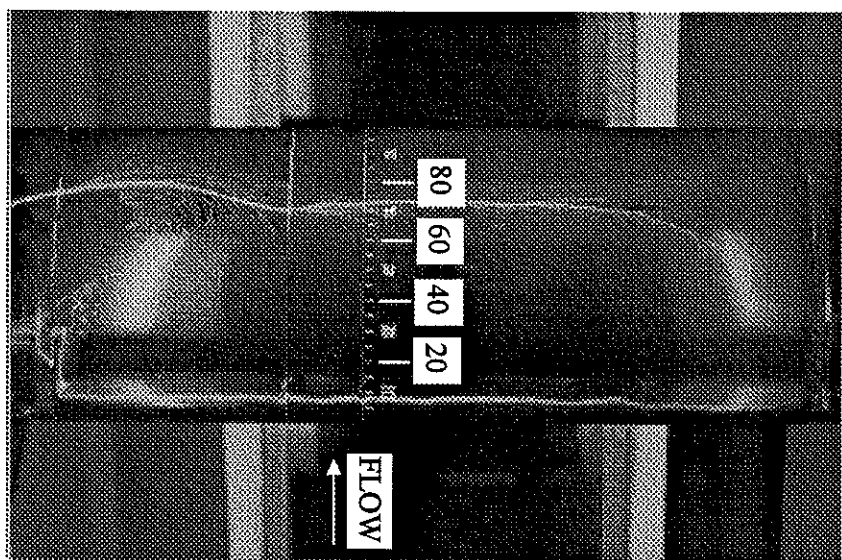


Figure 4.4c: $\alpha = 15^\circ$, $Re = 750,000$
LSLT

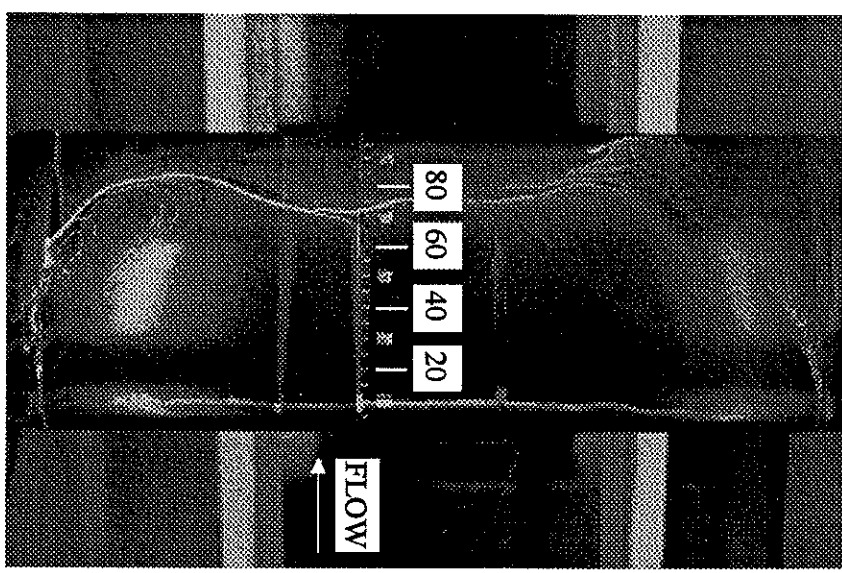


Figure 4.5a: $\alpha = 18^\circ$, $Re = 315,000$
ASWT

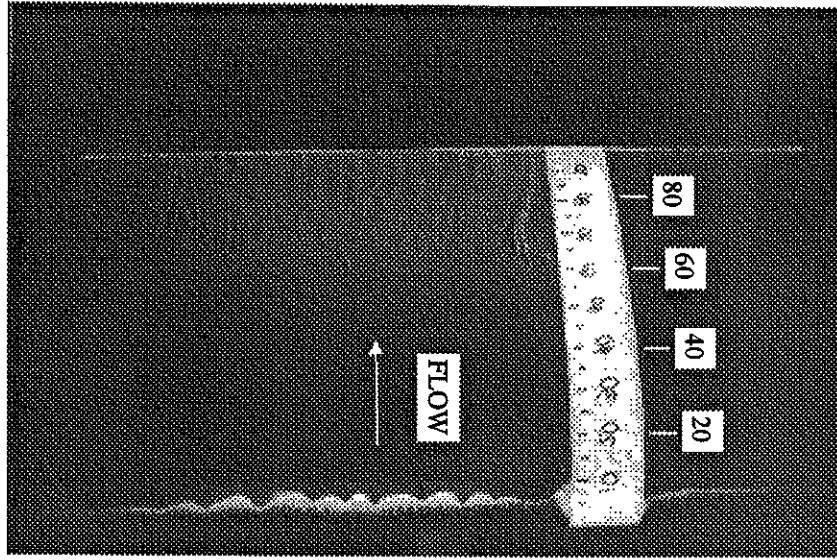


Figure 4.5b: $\alpha = 18^\circ$, $Re = 315,000$
LSLT

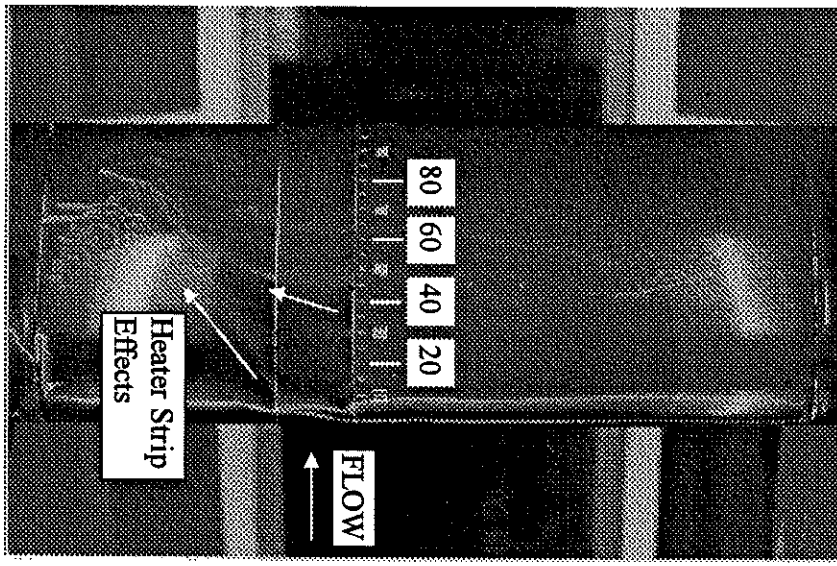


Figure 4.5c: $\alpha = 18^\circ$, $Re = 750,000$
LSLT

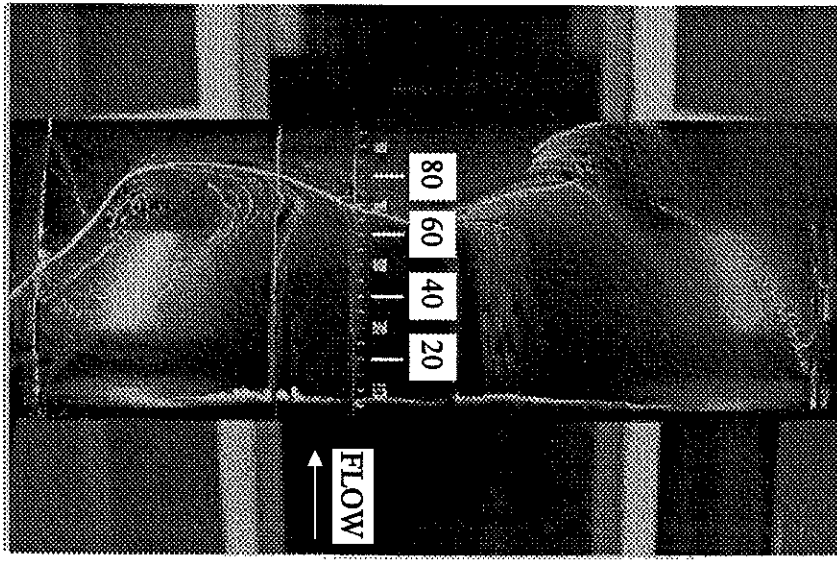


Figure 4.6a: $\alpha = 20^\circ$, $Re = 315,000$
ASWT

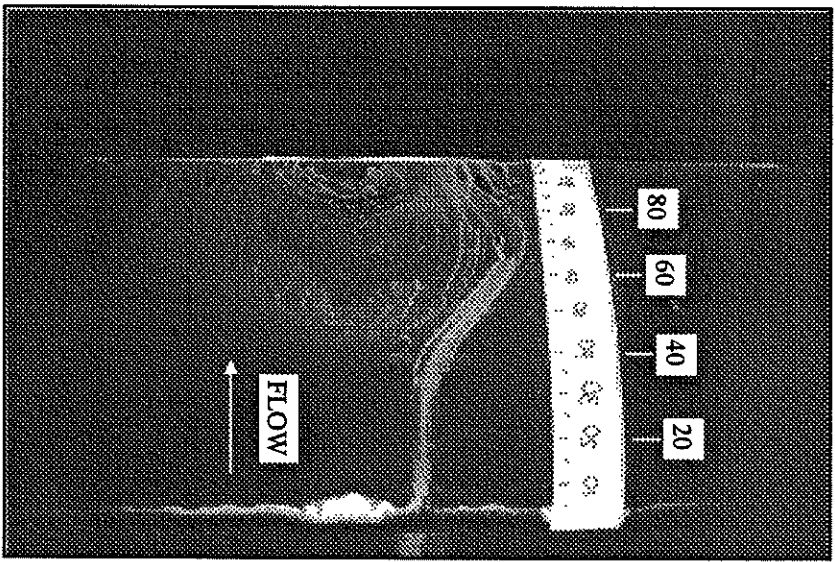


Figure 4.6b: $\alpha = 20^\circ$, $Re = 315,000$
LSLT

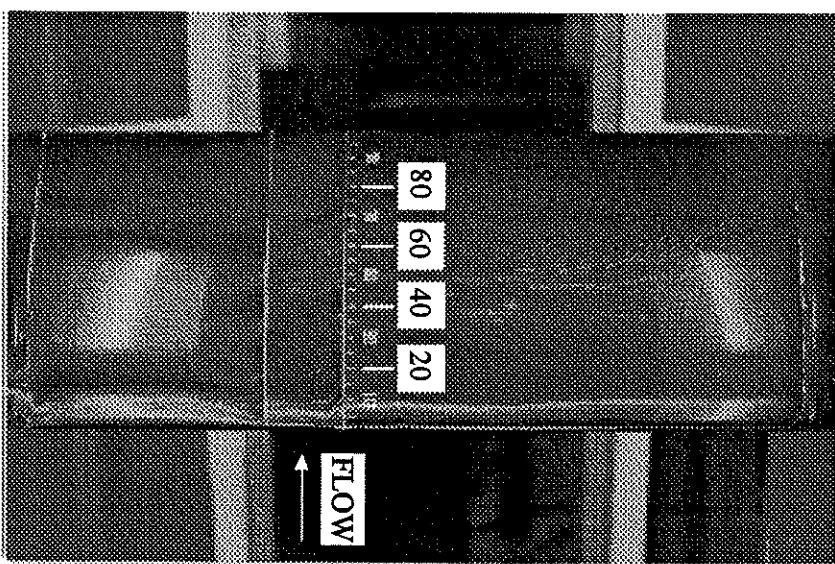


Figure 4.6c: $\alpha = 20^\circ$, $Re = 750,000$
LSLT

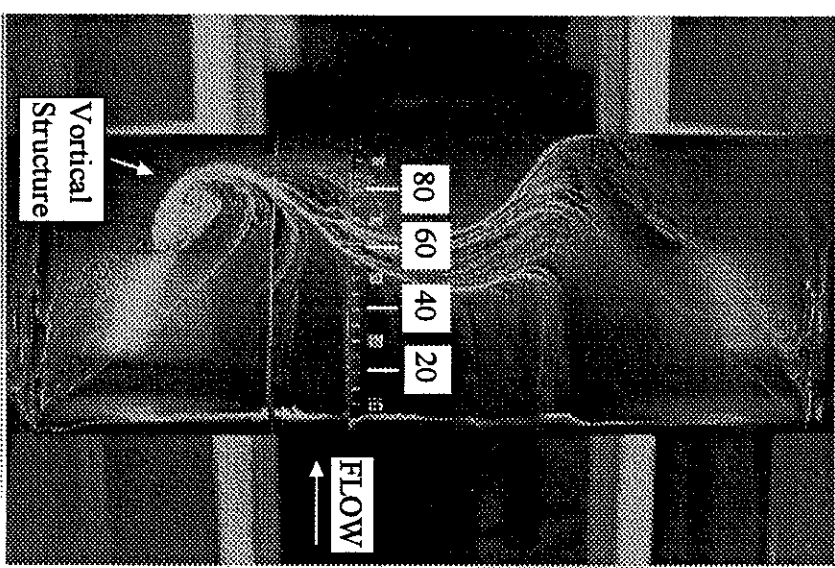


Figure 4.6 shows results for $\alpha = 20^\circ$. From Figure 4.6a, the laminar separation bubble in the ASWT at $Re = 315,000$ is located from 3-7%. The location of turbulent separation is more difficult to ascertain. From Figure 4.6a, it appears that turbulent separation occurs around 40% when examining the midspan region. However, after performing hot-wire

Figure 4.5 contains results for $\alpha = 18^\circ$. Figure 4.5a shows a laminar separation bubble at 5-10% with turbulent separation around 60%. From Figure 4.5b, it appears that a laminar separation bubble exists from 2-3%, followed by turbulent separation at about 10%. On the heater strip in this figure, however, the flow appears to be turbulent back to around 45% before separating. The heater strip thus appears to be affecting the surface flow patterns at this high angle of attack for $Re = 315,000$. It will be seen in the liquid crystal thermography results section that this heater strip effect for $Re = 315,000$ and $a = 18^\circ$ made taking meaningful heat transfer data impossible for this experimental configuration. For $Re = 750,000$, Figure 4.5c shows the laminar separation bubble from 6-10% and turbulent separation around 70 to 80%. While the laminar separation bubble remains two-dimensional for these test conditions, the turbulent separation is extremely three-dimensional, especially far from the strip.

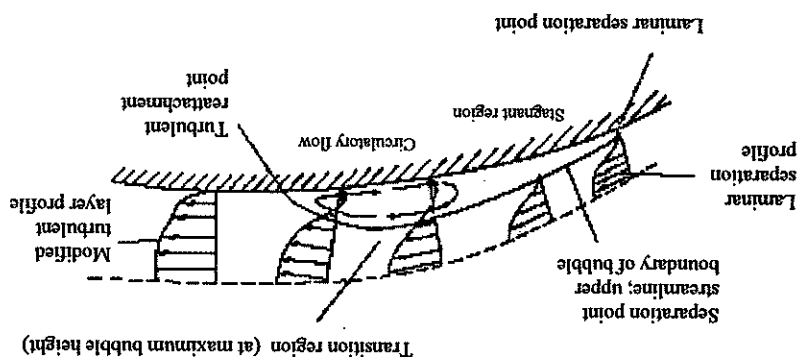
The results for $\alpha = 15^\circ$ are shown in Figure 4.4. This angle of attack is very near the angle of maximum lift coefficient for the SMT01 airfoil. The ASWT results of Figure 4.4 reveal a laminar separation bubble from 6-15% and turbulent separation around 65 to 70% for a Reynolds number of 315,000. Figure 4.4b shows that at the same Reynolds number in the LSLT, the laminar separation bubble is also from 6-15% with turbulent separation around 68 to 72%. Figure 4.4c shows that the laminar separation at the same Reynolds number has moved to 9-11% with turbulent separation at 70%. The flow patterns on the airfoil surface are still fairly two-dimensional at the heater strip location for the test conditions of these figures. Away from the heater strip toward the tunnel walls, three dimensionality of the flow patterns is beginning to appear, especially at $Re = 750,000$. The ASWT results of Figure 4.4a also show some flow effect that is limiting the oil patterns to the midspan region of the model. This effect is not seen in the LSLLT results and might possibly be attributed to the circular cross-section of the ASWT and the corresponding larger blockage effect of the model in that smaller cross-section.

As an additional note, an apparent characteristic of laminar separation bubbles for the Reynolds numbers tested is observed. The separation bubble in Figure 4.1b seems to have two distinct regions associated with it. This is most evident from examining the upper portion of the span away from the heater strip in the figure. This trait is somewhat difficult to see in the figure reproduced for this thesis; however, the original photographs showed this characteristic very clearly. As already mentioned, the laminar separation bubble spans from 57 to 75% of the chord. However, upon closer inspection of Figure 4.1b, it seems that the oil has remained much thicker on the surface from 57 to 62%. The oil from 62 to 75% is much more scrubbed away. It appears that the aft portion of the laminar separation bubble has much more circulation than the forward portion, causing the division occurring at about 35% chord. This apparent trait of the laminar separation bubble was also observed for the cases of Figures 4.3b and 4.4b and for some of the higher Reynolds numbers cases in the original flow visualization photographs; the reproduced photographs are not very clear in showing this division of the separation bubble. Gad-el-Hak and Bushnell give a sketch of a laminar separation bubble that shows what has just been mentioned: a thin forward portion of the bubble and a recirculating zone at the aft of the bubble (Gad-el-Hak and Bushnell, 1991). See Figure 4.7.

Figures 4.1c to 4.6c. laminar separation bubble at 5-7% with turbulent separation around 60 to 80%. Turbulent separation is extremely three-dimensional. A three-dimensional vertical structure near the airfoil surface is seen below the heater strip. Its development can be traced through Figures 4.1c to 4.6c. At this same Reynolds number, Figure 4.6b shows what seems to be a laminar LSLT at this same Reynolds number, Figure 4.6b shows what seems to be a laminar chord. The turbulent separation is seen to be extremely three-dimensional. For the velocity profile surveys at the midspan (Section 5.2), it is known that the flow is separated by 25% chord. Thus an estimate of the turbulent separation location is around 20%

Figure 4.8: Two Regions of Laminar Separation Bubble

Source: Houghton and Carpenter, 1993



In addition, after performing this flow visualization work, a reference was found that discussed the division of a laminar separation bubble into two regions. Figure 4.8 is taken from *Aerodynamics for Engineering Students*, 4th edition (Houghton and Carpenter, 1993). Houghton and Carpenter report, "Within the bubble,, two regimes exist. In the upstream region a pocket of stagnant fluid at constant pressure extends back some way and behind this a circulatory motion develops ...".

Figure 4.7: Sketch of a Laminar Separation Bubble

Source: Gad-el-Hak and Bushnell, 1991

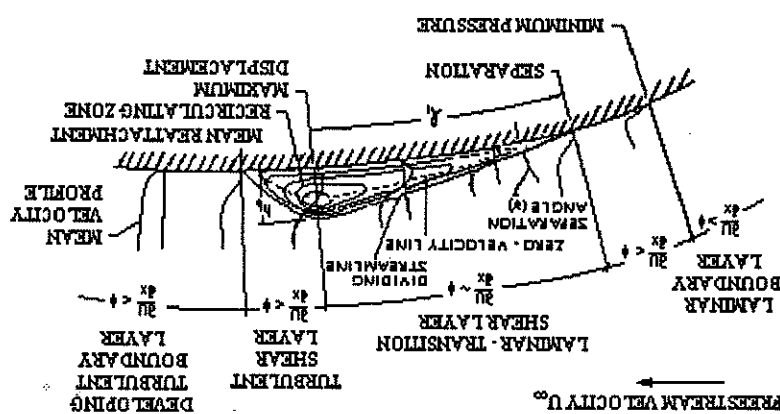


Table 4.1 presents a summary of the fluorescent oil flow visualization results. Included in the table are results for all angles of attack tested for both Reynolds numbers and both facilities. As would be expected, for a fixed Reynolds number as the angle of attack is increased, the laminar separation bubble moves forward toward the leading edge and becomes smaller. In addition, for a fixed angle of attack, as the Reynolds number is increased, the laminar separation bubble moves towards the trailing edge and becomes smaller. It must be mentioned, however, that the differences were minor and probably the LSLT. It appears from the data of Table 4.1 that for a given Reynolds number and angle of attack, the laminar region of flow over the airfoil is slightly longer in the ASWT than in the LS LT. It must be mentioned, however, that the differences were minor and probably the LS LT. The laminar trend in the ASWT is indeed valid, it should be mentioned that it was not expected laminar fluctuations, the ASWT laminar flow region was expected to be shorter than the laminar flow region in the LS LT. An explanation for this longer laminar flow region in the ASWT may be found when blockage effects and related three-dimensional flow patterns near the ends of the airfoil are considered. The blockage in the ASWT is greater than the blockage in the LS LT because of the smaller test section cross-section of the ASWT. Thus, the flow could be accelerated locally near the airfoil causing longer laminar flow regions in the ASWT. Existence of three-dimensional vertical flow structures near the airfoil ends could also induce core flow variations near the midspan of the airfoil.

The region of turbulent separation is much less in the ASWT than in the LS LT. For angles of attack of zero and five degrees, the ASWT results do not show any turbulent separation while the LS LT results indicate turbulent separation near the trailing edge. For $\alpha = 15^\circ$ and 20° , turbulent separation occurs near midchord in the ASWT but around 10% chord in the LS LT. These differences are dramatic. Again, blockage effects could be playing a role by constraining the flow in the ASWT and not allowing it to separate as it would in a less-restricted test environment.

It appears from the data of Table 4.1 that for a given Reynolds number and angle of attack, the laminar region of flow over the airfoil is slightly longer in the ASWT than in the LS LT. The laminar trend in the ASWT is indeed valid, it should be mentioned that it was not expected laminar fluctuations, the ASWT laminar flow region was expected to be shorter than the laminar flow region in the LS LT. An explanation for this longer laminar flow region in the ASWT may be found when blockage effects and related three-dimensional flow patterns near the ends of the airfoil are considered. The blockage in the ASWT is greater than the blockage in the LS LT because of the smaller test section cross-section of the ASWT. Thus, the flow could be accelerated locally near the airfoil causing longer laminar flow regions in the ASWT. Existence of three-dimensional vertical flow structures near the airfoil ends could also induce core flow variations near the midspan of the airfoil.

The region of turbulent separation is much less in the ASWT than in the LS LT. For angles of attack of zero and five degrees, the ASWT results do not show any turbulent separation while the LS LT results indicate turbulent separation near the trailing edge. For $\alpha = 15^\circ$ and 20° , turbulent separation occurs near midchord in the ASWT but around 10% chord in the LS LT. These differences are dramatic. Again, blockage effects could be playing a role by constraining the flow in the ASWT and not allowing it to separate as it would in a less-restricted test environment.

4.1.4 Conclusions from Oil Flow Visualization

Table 4.1: Fluorescent Oil Flow Visualization Summary

α (deg.)	Re	Laminar Flow	Laminar Separation Bubble	Turbulent Flow	Turbulent Separation
0	315,000	0-59%	0-27%	59-75%	75-100%
	750,000	-	0-61%	57-75%	75-100%
5	315,000	0-35%	0-23%	35-50%	50-100%
	750,000	-	0-21%	51-75%	75-100%
10	315,000	0-12%	0-11%	12-25%	25-85%
	750,000	-	0-12%	12-18%	18-80%
15	315,000	0-6%	0-6%	6-15%	15-68%
	750,000	-	0-9%	9-11%	11-70%
18	315,000	0-5%	0-2%	5-10%	10-60%
	750,000	-	0-6%	6-10%	10-75%
20	315,000	0-3%	0-2%	3-7%	7-20%
	750,000	-	0-3%	5-8%	7-70%

ASWT (no heater strip) = LS LT T (with heater strip) =

Several reasons exist for conducting liquid crystal thermography experiments. The main objective is to provide a comparison to the qualitative fluorescent oil flow visualization results. By comparing the heat transfer results to the fluorescent oil flow

4.2.1 Objectives of the Heat Transfer Experimentation

to liquid crystal thermography is given, and related past work is discussed.

Liquid crystal thermography that was performed for the current research. An introduction to liquid crystal thermography is given, and related past work is discussed.

The following sections give a detailed account of the flow visualization work based on

4.2 Liquid Crystal Thermography

visualizations findings.

Results from the heat transfer experiment, be compared to the oil flow map.

method that will now be discussed involves cor.

attack ($\alpha > 15^\circ$). This flow two-dimensionality is

regions were seen to be two-dimensional except for two

airfoil. Six angles of attack were examined at two different

flow angles of

A baseline now exists for the locations of the various flow

This strip effect will be seen again in Section 4.2.16 during the heat tr

20° at a Reynolds number of 315,000, the strip did seem to be having an , 'sisted effect.

surface flow patterns for most of the tests. However, at angles of attack equal to 18° and

This flow visualization study has shown the heat strip to have little effect on the

horizontal ASWT versus the vertical LS TT mounting orientation of the model.

blockage effects, three-dimensional flow structures near the ends of the airfoil, and the

the unequal free stream turbulence intensity levels of the two wind tunnels, tunnel

also show this turbulent separation characteristic. These differences can be attributed to

obvious. Note the accumulation of oil at a distinct separation line. Figures 4.3a and 4.3b

location. The turbulent separation location in the LS TT as seen in Figure 4.4b is more

turbulent separation pattern in the ASWT case of Figure 4.4a does not show a distinct turbulent separation

Finally, the turbulent separation in the ASWT can be seen to be less dramatic than the

A short time after Reinitz noticed this property of cholesterol benzoate, German physicist O. Lehmann termed the distinct compounds with two melting points as "liquid crystals" since the intermediate phase contained areas that appeared to have crystal-like structures. This name makes sense since the liquid crystal phase exhibits the "mesophase." The second melting point occurred when the cloudy liquid turned to a clear liquid.

The substance today known as liquid crystals was first discovered in 1888 by Austrian botanist Friedrich Reinitz who observed that the organic compound cholesterol benzoate appeared to have two distinct melting points (Ferguson, 1964). The first melting point occurred when the solid phase turned to a cloudy liquid phase. This has since been called the "mesophase." The second melting point occurred when the cloudy liquid turned to a clear liquid.

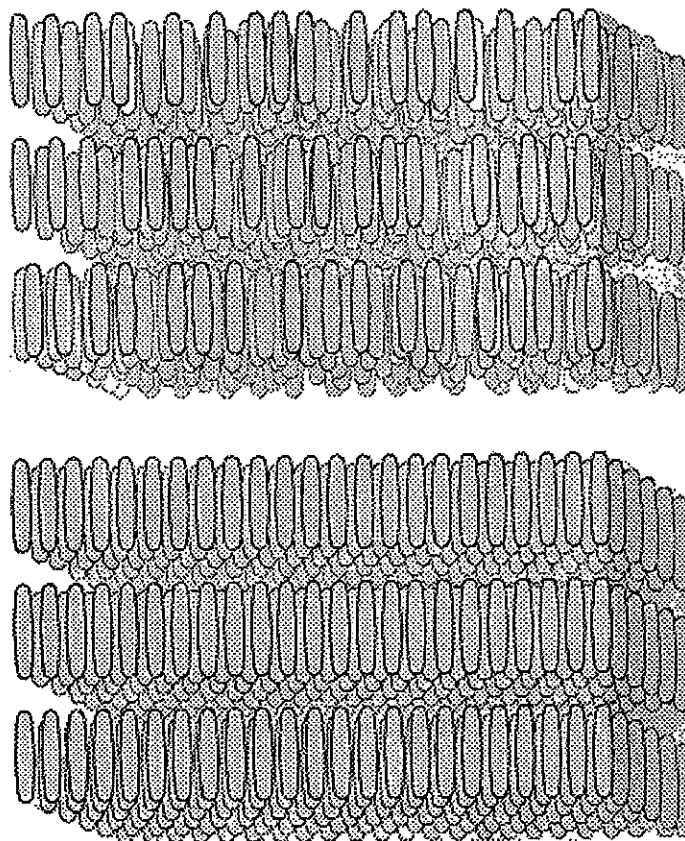
4.2.2 Liquid Crystal History and Properties

A second objective of this heat transfer research is to generate experimental convective heat transfer data for an airfoil with low free stream turbulence conditions. According to Poinsatte and Van Fossen, 1990), the data generated during this investigation can serve as a benchmark solution for the development of better viscous flow/heat transfer codes. Development of heat transfer prediction tools capable of handling large transitional zones currently requires high-quality high-resolution heat transfer measurements.

If the heat transfer method yields the same information about the flow regions on an airfoil that the fluorescent oil method provides, the heat transfer method could then be used for flow visualization in situations where fluorescent oil flow visualization is not practical. Examples of such instances include spinning turbomachinery and flight testing. It is thus hoped that the heat transfer method will confirm the existence and locations of the laminar, transitional, turbulent, and separated flow regions on the SMT01 airfoil under various experimental conditions. Only when these flow regions are well defined can work begin on actively trying to control the separated zones.

Figure 4.9: Smectic Liquid Crystal Molecular Structure

Source: Ferguson, 1964



crystal substance is a soap bubble.

Smectic liquid crystals get their name from the Greek word for soap. They exhibit cigar-shaped molecules arranged side-by-side in layers which are one molecule thick. The long axes of the molecules are parallel to each other and are perpendicular to the plane of the layer. See Figure 4.9. The molecules may either be arranged in rows (top of Figure 4.9) or randomly (bottom of Figure 4.9) in the layers. An example of a smectic liquid crystal substance is a soap bubble.

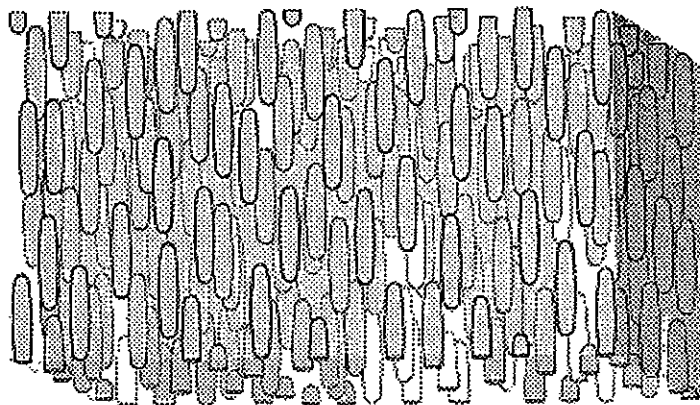
Liquid crystals are thus organic compounds that exhibit a unique molecular structure. Slight differences in molecular structure divide liquid crystals into three categories: smectic, nematic, and cholesteric. These classes were proposed by G. Friedel in 1922 and are described by Ferguson (Ferguson, 1964).

Fluid nature of a liquid while at the same time maintaining a degree of anisotropic and ordered structure like a crystalline solid (Ferguson, 1964).

The third type of liquid crystals is termed "cholesteric." This name stems from the fact that their molecular structure is characteristic of a large number of compounds that contain cholesterol. The molecules are arranged in layers with the long axes of the molecules parallel to the plane of the layers. In each layer the long axes of the molecules are slightly rotated with respect to adjacent layers thereby creating a helical pattern. This pattern can be seen in Figure 4.11.

Figure 4.10: Nematic Liquid Crystal Molecular Structure

Source: Ferguson, 1964

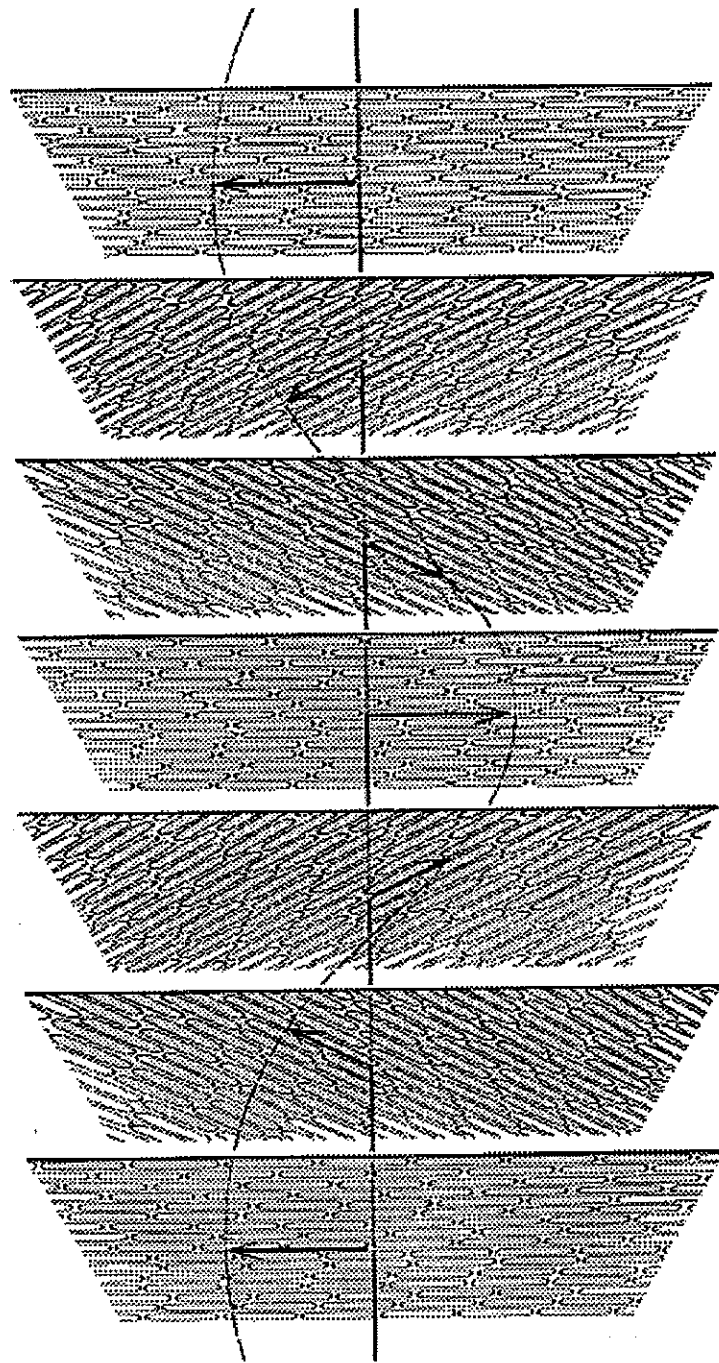


The name for nematic liquid crystals comes from the Greek word for thread. This name is appropriate because nematic liquid crystals contain microscopic thread-like structures floating freely or attached to the surface of the container. The molecules are arranged with long axes parallel, but no layers exist. The molecular structure of nematic liquid crystals is not as ordered as that of smectic liquid crystals. Figure 4.10 shows the nematic liquid crystal molecular structure.

An interesting property of smectic and nematic liquid crystals is that when applied in a thin film and viewed through a dielectric material such as glass, the liquid crystals appear

Figure 4.11: Cholesteric Liquid Crystal Molecular Structure

Source: Ferguson, 1964



As a result of the microencapsulation process, liquid crystals are very useful in the determination of surface temperature. Liquid crystals provide a way to obtain local temperature measurements at a high resolution over a model surface without obstructing the flow or local heat flux. This is in contrast to thermocouples which are point sensors and may protrude into the flow. Liquid crystals have a color response time of no more than 100 microseconds.

Encapsulated liquid crystals are available in two forms. They can be obtained on a precoated, blackened substrate of paper or as a water-based slurry. The slurry form allows more freedom in that it may be airbrushed onto any surface regardless of the geometry.

Microencapsulation thus creates a substance that is affected primarily by temperature, a quantity to which the projected color of the liquid crystals can be directly related. Microencapsulation allows gelatin in a polyvinyl alcohol binder to form spheres 10 to 40 microns in diameter around very small amounts of the liquid crystal mixture. The liquid crystals are then referred to, appropriately enough, as encapsulated liquid crystals and are greatly shielded from the effects of shear stress, chemical vapors, and ultraviolet light.

Advanced fabrication techniques have solved this dilemma. The process of microencapsulation allows gelatin in a polyvinyl alcohol binder to form spheres 10 to 40 microns in diameter around very small amounts of the liquid crystal mixture. The liquid crystals are then referred to, appropriately enough, as encapsulated liquid crystals and are greatly shielded from the effects of shear stress, chemical vapors, and ultraviolet light.

The distance between aligned molecular layers of liquid crystals affects the color that the liquid crystal projects. For pure liquid crystals, the distance between aligned molecular layers can be altered by temperature and shear stress as well as chemical vapors, ultraviolet light, and magnetic and electric fields. An example of electric fields affecting smectic and nematic liquid crystals was described in the previous paragraph. These many factors affecting the pure liquid crystals difficult. For instance, a color change in the experimentation with pure liquid crystals difficult. For instance, a color change in the liquid crystals could not be directly related to any one parameter. Temperature and shear stress effects as well as contributions by ultraviolet light, chemical vapors, and electric and magnetic fields had to be examined. Separating the effect of merely temperature on the liquid crystal molecular structure and thus its projected color was extremely difficult.

When subjected to an electric field, liquid crystals appear transparent (Cooper, Field, Meyer, 1975).

opaque when subjected to an electric field. When the electric field is removed, the liquid

thermography cameras which also yield continuous temperature distributions. This is operating temperatures. Liquid crystals are also much cheaper to use than infrared a great reduction in cost from testing turbine blades, for example, at their normally high involving liquid crystals can be conducted at room temperature conditions. This provides Practically also makes liquid crystals a valuable temperature measuring tool. Tests

always correlate to the same precise temperature values.

restart the experiment. Colors, regardless of when or in what order they appear, will sprayed may be reoriented or flow conditions in a test may be changed without having to cool, the reverse color order is seen. Thus the surface on which the liquid crystals are colorless to red, yellow, green, blue, violet, and again colorless. As the liquid crystals heated through their color range, they show a continuously changing color spectrum from

Reversibility is also an important property of liquid crystals. As the liquid crystals are one $^{\circ}\text{C}$ will display color from $30\text{ }^{\circ}\text{C}$ to $31\text{ }^{\circ}\text{C}$.

instance, a liquid crystal mixture with an even temperature of $30\text{ }^{\circ}\text{C}$ and a bandwidth of over which all the colors of the visible spectrum are displayed by the liquid crystals. For mixture first begins to display a reddish color. The bandwidth is the temperature range from 0.1 to $50\text{ }^{\circ}\text{C}$. The even temperature is the temperature at which the liquid crystal substrates can be mixed to achieve even temperatures from -40 to $285\text{ }^{\circ}\text{C}$ and bandwidths $^{\circ}\text{C}$. Liquid crystals also have good resolution on the order of $0.1\text{ }^{\circ}\text{C}$. Liquid crystal temperature variations. For narrow band crystals these variations may be as small as 0.15 Another attractive feature of liquid crystals is their ability to respond to slight on a given test surface.

thermocouple arrays, and also qualitatively reveal the thermal patterns and isotherm lines obtained by using liquid crystals. The distributions are continuous, unlike the results of relationship can be calibrated to enable precise surface temperature distributions to be distance between molecular layers of the liquid crystal. This color/temperature on the sensed temperature. This property is caused by the temperature affecting the As already mentioned, liquid crystals scatter light at different wavelengths depending thermocouple.

than a few milliseconds (Treland and Jones, 1987) which is of the same order as a typical

side of the wall. Therefore, the heat conduction may be assumed one-dimensional. During the transient test does not penetrate far into the wall such that it reaches the other model's wall is assumed to be a semi-infinite medium, meaning that the thermal energy coating of liquid crystals, the colors of which are recorded with a video camera. The (e.g. relatively cold) flow. The surface temperature distribution is monitored using a (e.g. hot) model into impulsively starting the flow over the model or by rapidly injecting a such as Plexiglas. A step change in the convective heating must then be created, either by such as Plexiglas. To use this technique, the test model should be constructed from an insulating material

4.2.3.1 Transient Technique

Liquid crystals may be used in convective heat transfer research through the use of two different techniques. These methods are the transient technique and the steady state technique. Both techniques are now discussed.

4.2.3 Types of Heat Transfer Experiments

Finally, it must be emphasized that liquid crystals have two primary uses. First, they may be used as a flow visualization tool to qualitatively see the thermal patterns (isotherms) on a surface. Laminar and turbulent flow regions, for instance, could be distinguished due to their different heating rates. Liquid crystals may also be used to measure continuous surface temperature distributions, thus allowing calculation of is quantitative and reasonably accurate is extremely useful due to the possibility of validating analytical and computational viscous flow/heat transfer models and new turbulence models. It is the job of the experimenter to decide how to best utilize liquid crystals for his or her work.

Because infrared image sensors must be cryogenically cooled during operation, and the test section viewing window must be made of a special material to allow infrared radiation transmission.

Figure 4.12 should help to further clarify the transient heat transfer method. Thus by knowing the model wall temperature and the corresponding time, the convective heat transfer coefficient, h , may be calculated for a substrate with known $\sqrt{P_{wall} c_{wall} k_{wall}}$.

$$\begin{aligned}
 k_{wall} &= \text{thermal conductivity of wall of model} \\
 c_{wall} &= \text{specific heat of wall of model} \\
 P_{wall} &= \text{density of wall of model} \\
 T_{\infty} &= \text{gas temperature (constant)} \\
 T_{initial} &= \text{initial wall temperature of model (constant)} \\
 T_{wall} &= \text{surface wall temperature of model at time } t \\
 \text{where } \gamma &= \frac{\sqrt{P_{wall} c_{wall} k_{wall}}}{h \sqrt{t}}
 \end{aligned}$$

$$\frac{T_{\infty} - T_{initial}}{T_{wall} - T_{initial}} = 1 - e^{-\gamma^2 erfc(\gamma)} \quad (4.2)$$

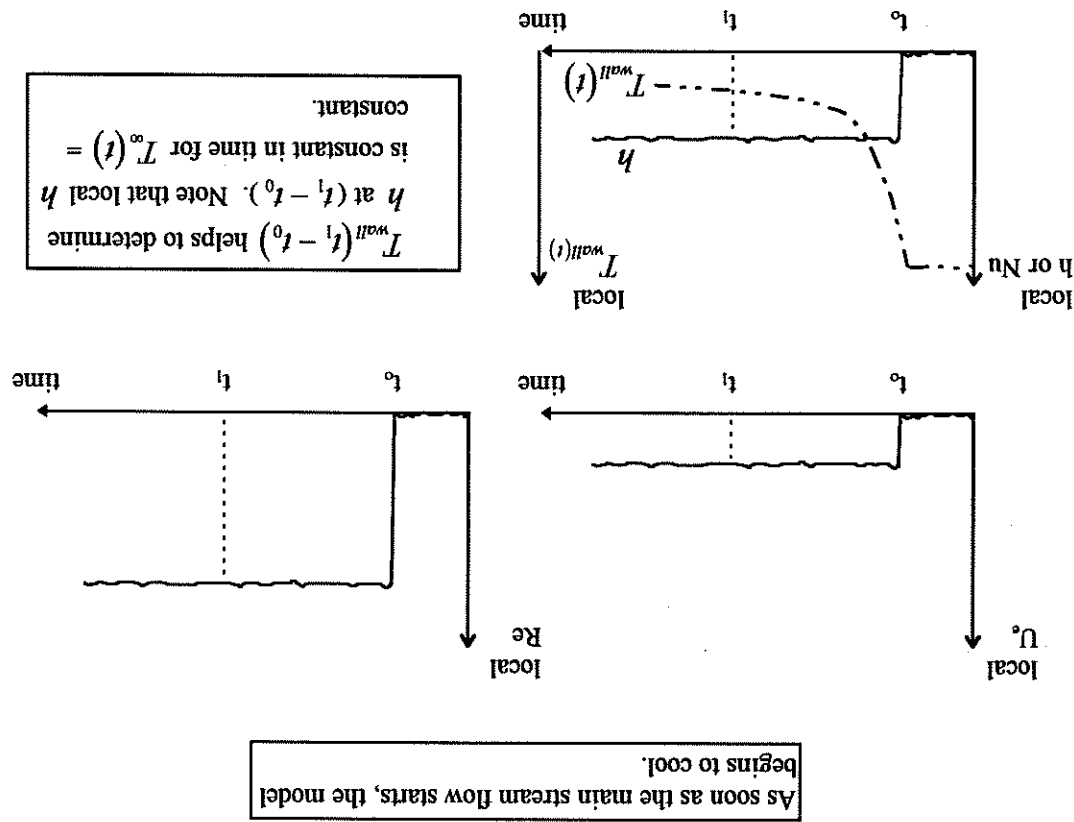
An analytic solution to equation 4.1 results (equation 4.2) if the thermal properties and gas temperature are assumed to be constant. Refer to Jones and Hippiensteel (1988), Camci, Kim, and Hippiensteel (1992), Camci, Hippiensteel, and Poinsatte (1993), and Kim (1991) for detailed discussion of the analytical solution process. Carslaw and Jaeger (1959) also discuss analytically solving equation 4.1.

$$\frac{\partial^2 T}{\partial z^2} = \frac{k_{wall}}{P_{wall} c_{wall}} \frac{\partial T}{\partial z} \quad (4.1)$$

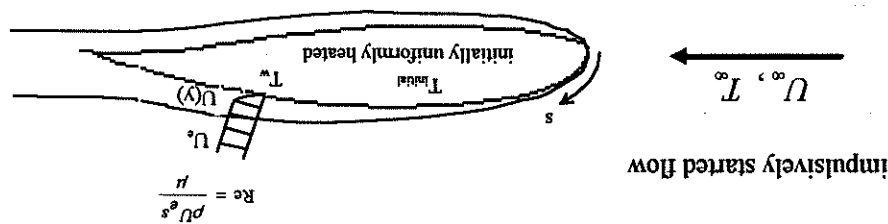
The convective heat transfer coefficient, h , may then be deduced from this time history of temperature by solving the 1D transient heat conduction equation analytically. The 1D transient heat conduction equation is as follows:

of temperature by solving the 1D transient heat conduction equation analytically. The 1D

Figure 4.12: Classification of Transient Heat Transfer Method



$$T_{initial} > T_\infty$$



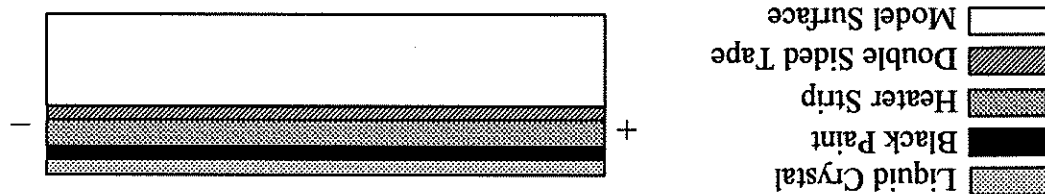
In incompressible flow h and skin friction coefficient C_f are analogous.

h is a measure of the ability of the viscous layer to transfer heat by forced convection

$$h = \frac{T_{wall} - T_\infty}{q''_{TOTAL} - q''_{COND} - q''_{RAD}} \quad (4.3)$$

heat transfer coefficient is calculated via Newton's Law of Cooling. Knowing the temperature information at the various power settings, the convective process is repeated until the color bands have covered the entire heater strip surface. Again steady state is allowed to be realized, and an image is recorded. This bands. Again steady state is allowed to be realized, and an image is recorded. This information. The power to the heater strip is then increased causing a shifting of the color with an image processor. The colors on the heater strip directly yield temperature conditions are allowed to be reached, and then an image of the heater strip is recorded strip. The DC voltage is increased until color bands appear. At this point steady state model is then exposed to the flow, and a DC voltage is applied across the heater.

Figure 4.13: The Composite Heater Element



heater strip. A typical composite heater element is shown in Figure 4.13. After the black paint is applied, a very thin coating of liquid crystals is sprayed onto the strip is then spray painted black to provide the best color contrast for the liquid crystals. heater element is usually performed by using a double-sided tape. The attachment of the temperature variations in the experimental temperature range. The attachment of the surface (such as Inconel 600) does not change its electrical resistance due to local (1988) for information on this method. The basic assumption is that the metallic heater the surface of the test model. Refer to Wiedner (1994) and Hippenssteile and Russell (1988) for information on this method. This method of heat transfer research requires the use of a heater element attached to

4.2.3.2 Steady State Technique

$$q''_{RAD} = \alpha e_{wall} T_{wall}^4 - \alpha e_\infty T_\infty^4 \quad (4.6)$$

magnitude, is estimated by using a black body assumption.

The radiation loss term, which is relatively small when T_{wall} and T_∞ are close in

$$t_{wall} = \text{model wall thickness}$$

is measured

$$T_2 = \text{temperature on side of wall opposite to where } T_{wall}$$

$$T_{wall} = \text{surface wall temperature of model}$$

where

$$q''_{COND} = h_{wall} \frac{t_{wall}}{T_{wall} - T_2} \quad (4.5)$$

The conduction loss term is approximated as one-dimensional.

a technique are given in Wiedner and Cimci (1996).

One should notice that equation 4.4 is valid only for rectangular heater geometries with any aspect ratio. For heater surfaces having arbitrarily specified boundaries, a more elaborate technique is required for the accurate calculation of q''_{TOTAL} . Details of such a technique are given in Wiedner and Cimci (1996).

$$A_{heater} = \text{area of heater element}$$

$$R_{heater} = \text{resistance of heater element}$$

$$V_{heater} = \text{voltage across heater element}$$

where

$$q''_{TOTAL} = \frac{R_{heater}^{GENERATED} A_{heater}^{strip}}{V_{heater}^{strip}} \quad (4.4)$$

For simple Joulean heating,

flow situations. See Figure 4.14. These prediction tools must be able to handle many complicated computational methods. The h distributions can be used as benchmark data against which to compare the needed to improve viscous flow/heat transfer tools that use the Navier-Stokes equations. Relating back to one of the objectives of the current study, accurate h distributions are heat transfer is important.

This section presents several examples in which accurate convective heat transfer information is necessary. These are but a few of the many areas in engineering in which heat transfer is necessary.

4.2.4 Importance of the Convective Heat Transfer Coefficient, h

These two methods are used to obtain high-resolution convective heat transfer data. The next section will give some insight as to why it is important to have methods to accurately calculate convective heat transfer coefficient values.

This composite heater strip method surface has a minimal effect on the model geometry and thus on the flow. The heater strip has a minimal effect on the model geometry and thus on the flow. The heater strip composite construction should be as thin as possible, and the edges of the strip should smoothly blend in with the model surface, if possible. Care must also be taken with the steady state technique to ensure the heater strip surface. Care must also be taken with the steady state technique to ensure the heater strip geometry may be very complex since the liquid crystals are merely sprayed onto the model allowing the attachment of the heater element. For the transient technique, the model disadvantage of this steady state technique is that the model shape must be conducive to continuous and high-resolution heat transfer maps (Hippeneisteel and Russell, 1988). A simplicity, to be readily applied using commercially available products, and to provide This composite heater strip method is recognized by Hippeneisteel and Russell to have

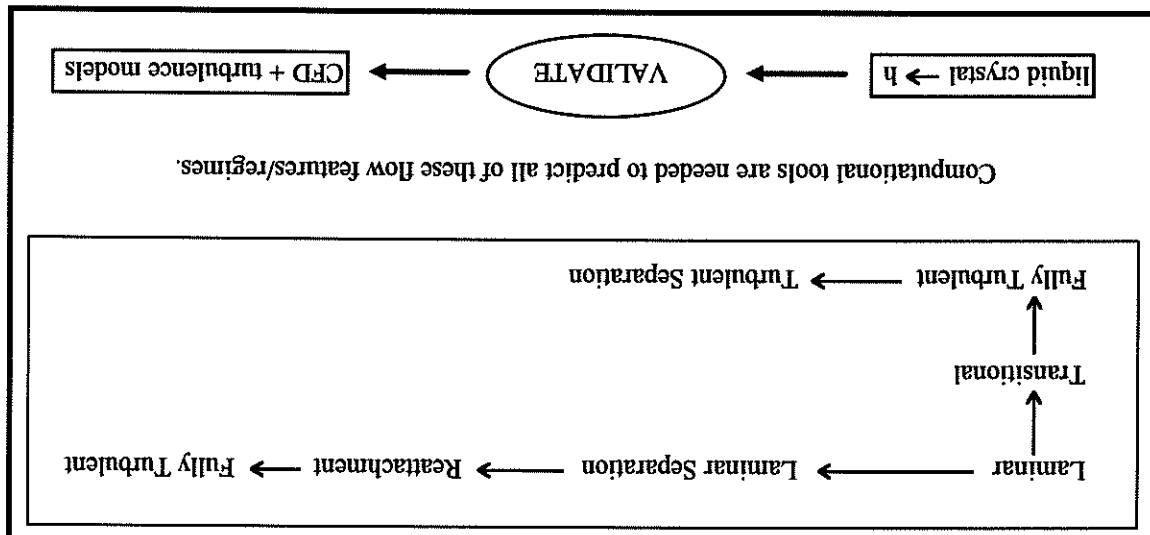
$$\begin{aligned}
 T_\infty &= \text{free stream static temperature} \\
 \epsilon_\infty &= \text{wind tunnel wall emissivity} \\
 \epsilon_{wall} &= \text{model wall emissivity} \\
 \sigma &= \text{Stefan-Boltzmann constant}
 \end{aligned}$$

where

As a use in aircraft aerodynamics, Kleim points out that convective heat transfer rate may be used to calculate local skin friction (Klein, 1968). Through integration of the skin friction over the aircraft surface, an accurate value of total drag may be obtained. To achieve this goal, gas turbine inlet temperatures and pressures must be increased. Thus the heat loads to the turbine blades must necessarily increase. If this is to become a reality, more effective cooling needs to be developed for turbine blades to provide acceptable metal temperatures and blade life. To precisely predict blade temperatures, accurate convective heat transfer coefficients must first be obtained (Hippeneister, Russell, and Torres, 1985).

In the field of turbomachinery there is a constant desire to increase engine efficiencies. In the field of high speed aircraft, materials for high speed aircraft.

Figure 4.14: Various Flow Regimes in Which Can Validate Codes



The first person to use liquid crystals as a tool for aerodynamic research was Enrico Klein in 1968. He used pure (unencapsulated) liquid crystals to study transition on a wind tunnel model of a supersonic airplane of symmetric cross section at a zero degree angle of attack. The turbulent boundary layer existing on the model caused the liquid crystals to display colors different from the colors associated with regions of laminar flow due to variations in surface temperature caused by the differing boundary layer flow characteristics. Klein's work was qualitative in nature only since the effects of temperature and shear stress are combined for pure liquid crystals. Klein noted that, "It is therefore clear that liquid crystals must be shielded from mechanical shear to obtain good quantitative results" (Klein, 1968). This statement was realized when microencapsulation became possible.

Quantitative convective heat transfer data were first obtained five years after Klein's work in 1973 by Vennemann and Buitensch (Simoenich and Moffat, 1984). They coated models with liquid crystals and aerodynamically heated them in a high-speed flow. A transient technique was used to calculate the convective heat transfer coefficient.

4.2.5 Past Heat Transfer Work Using Liquid Crystals

Specifically, an energy balance shows that convective and evaporative cooling are the important to have accurate knowledge of the heat transfer on the wing's surface. The wing surface at locations where the ice is going to form. In order to predict where ice will first begin to accumulate for given environmental and flow conditions, it is very important to stop it before it has a chance to form. This may be accomplished by heating on wings is to stop it before it has a chance to form. This may be accomplished by heating the wing surface at locations where the ice is going to form. In order to predict where ice will first begin to accumulate for given environmental and flow conditions, it is very important to have accurate knowledge of the heat transfer on the wing's surface.

The following section gives many examples of past instances where liquid crystals were employed to obtain experimental convective heat transfer data. Both transient and steady information is critical for accurately predicting icing (Poniatte and Van Fossen, 1990).

Specifically, an energy balance shows that convective and evaporative cooling are the important to have accurate knowledge of the heat transfer on the wing's surface. The wing surface at locations where the ice is going to form. In order to predict where ice will first begin to accumulate for given environmental and flow conditions, it is very important to have accurate knowledge of the heat transfer on the wing's surface.

The first steady state experiments using liquid crystals were performed by den Ouden and Hoogendoorn a year later in 1974. They used a constant temperature heat source and measured stagnation heat transfer from a jet impinging on a flat plate (den Ouden and Hoogendoorn, 1974). Hippenssteelle, Russel, and Torres also performed steady state heat transfer experiments. This group used the steady state method and liquid crystals to calculate convective heat transfer coefficients on the midchord of a turbine blade airfoil in a static cascade. They achieved a maximum uncertainty in h of 6.2% (Hippenssteelle, Russel, and Torres, 1985).

Jones used a transient technique to calculate convective heat transfer coefficient values. Specifically, they examined the effect of rib heat transfer promoters on the complicated flow in a representative blade trailing edge passage (Treland and Jones, 1985). An interesting study was performed by Jones and Hippenssteelle in 1988. They performed both transient and steady state experiments using liquid crystals to calculate convective heat transfer coefficients on a model duct wall. Results from both methods were consistent. For the transient tests, they combined two different liquid crystal mixtures with differing evaporation temperatures into a single liquid crystal mixture. This is possible since the liquid crystals are encapsulated, and each different liquid crystal mixture in the combination will act as though independent. Jones and Hippenssteelle used this combination of two different liquid crystal mixtures to eliminate the problem of determining an initial surface temperature at each point on the model. They call this technique the "double crystal method" (Jones and Hippenssteelle, 1988).

Meer et al. used liquid crystal thermography to study the location of transition in a flat plate boundary layer (Meer et al., 1991). The destabilizing effect of introducing heat into a gas boundary layer was examined. This destabilizing effect causes a measurement of the transition region that occurs when no heat is applied.

Camci and Glezer performed a liquid crystal heat transfer study on a rotating disk (Camci and Glezer, 1997). Their work showed that encapsulated liquid crystals do not respond to wall shear stress.

thermal conductivity, k , of the material through which the losses are occurring must be To estimate thermal conduction losses while using the steady state technique, the

4.2.6 Experimental Determination of Thermal Conductivity of the Wring Material

chosen for this study.

convective heat transfer coefficients on the SMT01 airfoil. The steady state technique was desired. The next section begins the discussion of the experimental determination of experiments that have been performed in which convective heat transfer information was

These past uses of liquid crystals in the engineering community show the types of

mixed so that a chemical hazard will change an indicator from green to red, for instance.

state, will react to certain chemical vapors by changing colors. Liquid crystals can be chemical leaks or hazards. This is possible since liquid crystals, especially in the pure In addition to non-destructive testing, liquid crystals may also be used as indicators for

material, and the liquid crystals will show a different color.

surroundings. Thus imperfections will be a different temperature than the surrounding surface and applying heat. Imperfections will conduct heat at a different rate than their (Parsley, 1991). Structural imperfections may be located by spraying liquid crystals onto a Another qualitative use of liquid crystals is in the area of non-destructive testing

circulation.

helping to assess the severity of infiltration of joints, and revealing areas of poor distribution caused by spinal cord injuries, aiding in the diagnosis of migraine headaches,

following as possible medical uses of thermography: checking for asymmetric temperature crystals may reveal abnormalities in local heating of the skin. And mentions the

the vasodilation or constriction of the subcutaneous arterioles. Thermography using liquid are the patency of the arteries bringing blood into the region, the rate of blood flow, and

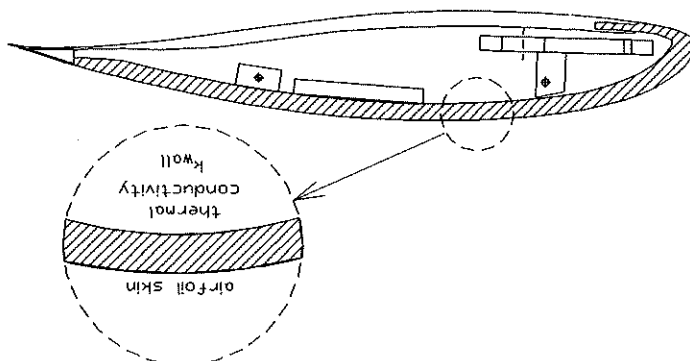
of subcutaneous blood supply. Among the factors affecting subcutaneous blood supply thermology is the science of studying local changes in skin temperature that are a function

Because of the interesting nature of this topic, it is briefly discussed here. Clinical paper entitled "Clinical Applications of Computerized Thermography" (Anbar, 1988).

Micahel Anbar discussed the value of thermography to the medical community in his

To accomplish this goal, a scrap piece of the wing material was cut into a rectangular shape. Figure 4.15 gives insight into the material being tested. A piece of Nickel 600 foil was taped to one surface of the test piece using double-sided tape, and copper bus bars were attached. The double-sided tape was 0.005 inches thick. Nickel foil was used for the heater strip because its resistance does not change in the experimental range in which it was used. Figure 4.16a shows the test piece. A Keltiley 580 micro-ohmmeter was used to measure the resistance of the heater strip to an accuracy of four decimal places. The wire leads marked "A" were used to apply a voltage across the heater strip using a Hewlett Packard 6261B DC power supply. The leads marked "B" were connected to a Fluke 77 multimeter so that the voltage across the heater strip could be measured. The wire coming from the center of the test piece is for a K-type cement-on thermocouple. The wire connecting the two surfaces opposite the heater strip. These two thermocouples were placed immediately below the Nickel foil. A second thermocouple which was placed immediately below the Nickel foil. A second thermocouple was attached to the surface opposite the heater strip. These two thermocouples were connected to a Fluke 77 multimeter so that the voltage across the heater strip could be measured. The wire coming from the center of the test piece is for a K-type cement-on thermocouple which was placed immediately below the Nickel foil. A second thermocouple was attached to the surface opposite the heater strip. These two thermocouples were connected to a Fluke 77 multimeter so that the voltage across the heater strip could be measured.

Figure 4.15: Sketch of Wing Material Being Tested



Since this material is composed of a layer of Owens Corning extruded polystyrene Foamular 150 sandwiched with layers of E-glass in an epoxy matrix, an estimate of the thermal conductivity could have been made based on the properties of those elements. However, it was felt that to minimize experimental error, the value of k should be experimentally determined.

thermocouples allowed the temperature difference through the wing material test piece to be measured. Figure 4.16b shows a side view of the test piece. Using micrometers, the average thickness of the test piece was measured to be 0.362 inches (0.919 cm) based on ten separate locations. Measurements were performed before attachment of the heater strip. A piece of space shuttle tile manufactured by Rockwell International Corporation was used to insulate the test piece. Insulation was important to minimize radiation and convection losses during the tests. Figures 4.16c and 4.16d show the insulation material and how the test piece was situated, respectively. In Figure 4.16e more insulating material was added to form sides of what would be an enclosing insulating box. The lid of the box can also be seen in the figure.

Figure 4.16g: Final k Testing Setup

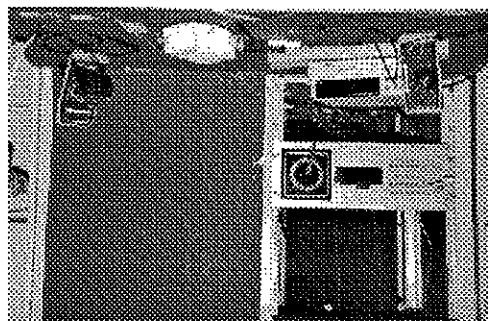


Figure 4.16f: Insulation Box Complete

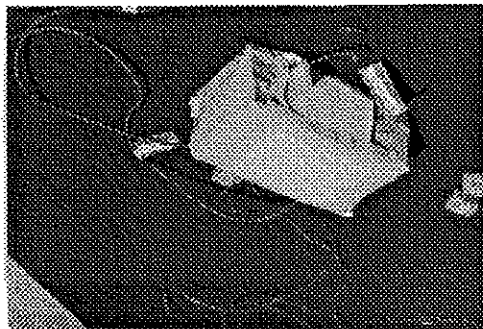


Figure 4.16e: Assembly of Insulating Box

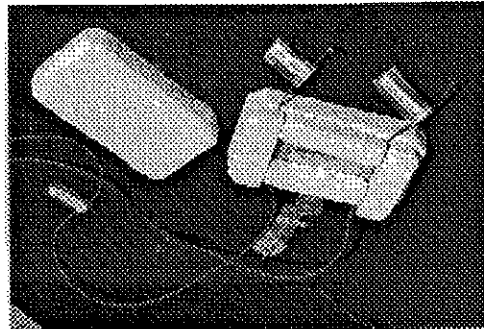


Figure 4.16d: Insulating the Test Piece

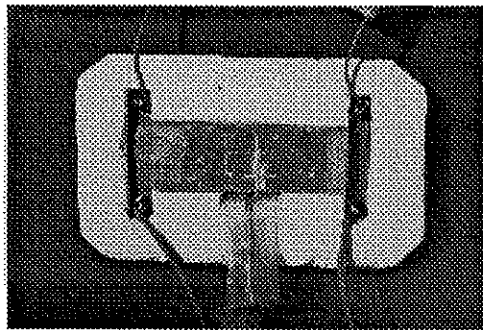


Figure 4.16c: Insulation Material

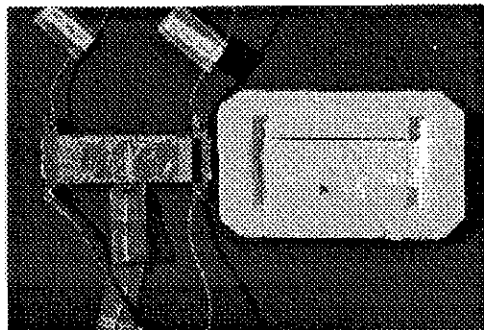


Figure 4.16b: Side View of k Test Piece

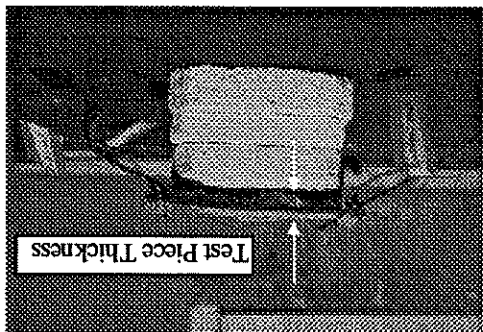
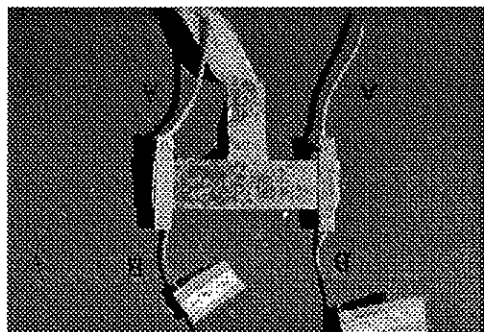


Figure 4.16a: k Test Piece



The thermal conductivity is the slope of the graph of the total generated heat flux versus temperature gradient through the wing material test piece. Tests were performed on four separate days, and the average slope was determined. Figure 4.17 presents the results for the thermal conductivity experiments.

$$\frac{P_{\text{heater}}}{V^2} = k_{\text{wall}} \frac{\Delta T}{T_{\text{wall}} - T_2} \quad (4.7)$$

obtained.

total heat flux generated due to the insulating enclosure, the following expression is obtained:

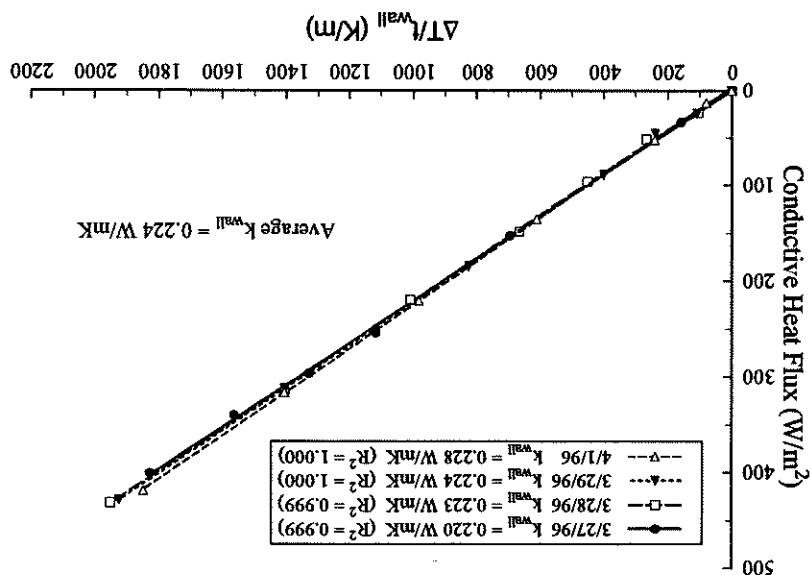
4.5. Combining those two equations and noticing that the conductive heat flux equals the wing material test piece, the thermal conductivity was determined from equations 4.4 and series of voltages to the heater strip and recording the temperature difference across the was attached to the thermocouples through a mechanical voltage scanner. By applying a display, had been connected to an Omega-CJ cold junction compensation which in turn measure the voltage across the heater strip. A second multimeter, a Fluke 45 Dual had been attached to the appropriate leads, and the multimeter had been connected to Figure 4.16C. The entire experimental setup is shown in Figure 4.16g. The power supply layers of paper towels and secured with masking tape. This final assembly can be seen in Figure 4.16C. After putting the lid on the insulating box, the entire assembly was wrapped in five

Material	T (°C)	k (W/mK)
Asbestos (sheet)	20	0.74
Bakelite	20	0.230
Brick (cement)	10	0.34
Fat	20	0.17
Plexiglas	20	0.184
Rubber (soft)	20	0.2

Table 4.2: Selected Samples of Thermal Conductivity Values of Insulators

To verify that the results of this testing made sense, the value of the thermal conductivity of the wing material was compared to that of several insulators taken from Appendix B, Properties of Solids, of Adrian Bejan's *Heat Transfer* (Bejan, 1993). An estimate of the uncertainty in the measurement, the method of Kline and McClintock (1953). It was found that $\Delta k_{wall} = \pm 8.9\%$ was a good representative value of the experimental uncertainty in k_{wall} .

Figure 4.17: Experimental Determination of k_{wall}



From these examples, the experimentally determined value of k for the wing material is seen to be of the correct order of magnitude and can be used with confidence to calculate the conduction losses through the wing material.

4.2.7 The Image Processing System

To record the liquid crystal colors and to convert the colors to quantitative temperature information, an image processor was used. The image processor is an NTSC (National Television System Committee) standard 24-bit color system which converts RGB (red, green, blue) information to HSI (hue, saturation, intensity) information for each pixel of a 512×480 image (Wiedner, 1994).

Hue corresponds directly to the dominant wavelength of the light entering the image processor sensor for the visible spectrum. Saturation refers to color purity, or in other words, the amount of white contained in a specific color. Intensity refers to the relative brightness of a color (Kim, 1991).

The RGB attributes were captured by the CCD sensor inside a standard 8mm video camera. Complete images were acquired at a rate of 30 frames per second. The RGB attributes were then multiplexed and sent to the image-capturing board made by Data Translation. The image processor system uses three eight-bit video A/D converters, which means that each RGB or HSI attribute varies between 0 and 255.

The hue attribute is used to determine the temperature at a given pixel location. The intensity attribute is used as a filtering device for a given pixel location. If the intensity value of a pixel falls below 50, the hue value becomes unstable, and the pixel can not be used to produce an accurate temperature value (Kim, 1991). Also, if the intensity value of a pixel exceeds 200, the hue value becomes less accurate due to the saturation of the CCD sensor in the video camera.

4.2.8 Modifications to Model Prior to ASWT Heat Transfer Experimentation

The ASWT tests were conducted with a finite aspect ratio 2.58 model since fluorescent measuring convective heat transfer coefficients with the existing laboratory equipment. Any problems that would arise would be addressed and corrected before final experimentation would take place in the higher-flow-quality (less turbulence, more two-dimensional test section flow) LSLT. Pittsburgh Paints spray enamel quick dry flat black to provide maximum color contrast for the liquid crystal images. The next step in preparing the model was to construct two bus bars inside of the wing that would provide electrical connections for the heater strip to be used in the steady state heat transfer technique that was chosen for experimentation. The bus bars were made out of sheet copper 1/16 inches thick. Two wires were attached to each bus bar using Circuit Works conductive epoxy. One wire on each bus bar would be used to apply constant DC voltages across the heater strip during experimentation. The other wire on each bus bar would provide leads for a multimeter to measure the applied voltage directly across the heater strip. This second set of wires eliminates the need to calculate the voltage drop across the power leads had the multimeter been used only to record the voltage supplied by the DC power supply.

The heater strip was then cut from a piece of Nickel 600 foil, the resistance of which is constant in the temperature range encountered during experimentation. The heater strip was cut as a rectangle with dimensions of $2\frac{1}{4} \times 1$ inch and had a thickness of 0.025 mm. The heater strip length allowed a $\frac{1}{4}$ inch excess on either end of the strip with which to make the bus bar connection (the total length of the strip from bus to bus was $2\frac{1}{4}$ inches). A strip of double-sided tape 0.005 inches thick was attached to the wing upper surface at the midspan where the heater strip would lie. The heater strip was then rolled onto the tape strip taking care to avoid trapping air bubbles beneath the foil. Figure 4.18 shows the heater strip attached to the upper surface of the model. The Nickel strip was then sprayed black in preparation for the liquid crystal coating.

The wing at its midspan showed that the flow was two-dimensional on the surface of the wing. Oil flow visualization results showed that the flow was two-dimensional on the surface of the wing. The next step in preparing the model was first painted with Pittsburgh Paints spray enamel quick dry flat black to provide maximum color contrast for the liquid crystal images. The next step in preparing the model was to construct two bus bars inside of the wing that would provide electrical connections for the heater strip to be used in the steady state heat transfer technique that was chosen for experimentation. The bus bars were made out of sheet copper 1/16 inches thick. Two wires were attached to each bus bar using Circuit Works conductive epoxy. One wire on each bus bar would be used to apply constant DC voltages across the heater strip during experimentation. The other wire on each bus bar would provide leads for a multimeter to measure the applied voltage directly across the heater strip. This second set of wires eliminates the need to calculate the voltage drop across the power leads had the multimeter been used only to record the voltage supplied by the DC power supply.

The heater strip was then cut from a piece of Nickel 600 foil, the resistance of which is constant in the temperature range encountered during experimentation. The heater strip was cut as a rectangle with dimensions of $2\frac{1}{4} \times 1$ inch and had a thickness of 0.025 mm. The heater strip length allowed a $\frac{1}{4}$ inch excess on either end of the strip with which to make the bus bar connection (the total length of the strip from bus to bus was $2\frac{1}{4}$ inches). A strip of double-sided tape 0.005 inches thick was attached to the wing upper surface at the midspan where the heater strip would lie. The heater strip was then rolled onto the tape strip taking care to avoid trapping air bubbles beneath the foil. Figure 4.18 shows the heater strip attached to the upper surface of the model. The Nickel strip was then sprayed black in preparation for the liquid crystal coating.

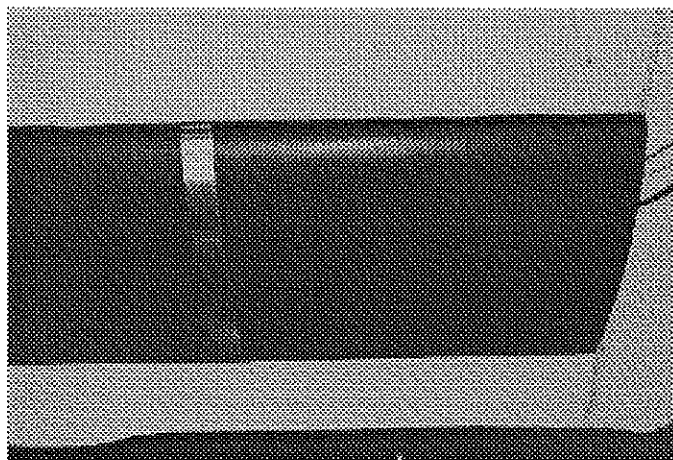
contraction section of the ASWT. By varying the tunnel speed, a calibration plot of the other transducer was connected to static pressure ports located before and after the transducers was next connected to the total and static ports of the pitot-static probe. The transducers were used to read the pressure transducer output voltages. One of the pressure voltmeters were used to read the pitot pressure transducer output voltages. TSI integrating Instrument hand pump and a Dwyer Instruments, Inc. manometer, TSI integrating Validyne Model CD15 Camber Demodulator, were then calibrated using a Meriam section. Two 0.125 psi Validyne differential pressure transducers, each connected to a calibrator. A pitot-static probe was positioned along the centerline of the empty test section. Before installing the model into the ASWT for testing, the wind tunnel first had to be calibrated.

4.2.9 ASWT Setup for Heat Transfer Experimentation

Before installing the model into the ASWT for testing, the heat flux generated by the heater strip used in calculating conduction losses from the heat flux generated by the heater strip. Finally, a single K-type cement-on thermocouple was attached inside the wing to the lower surface at approximately a 60% chordwise location. The purpose of this thermocouple was to record the model's internal temperature (T_3 , in equation 4.5) to be used in calculating conduction losses from the heat flux generated by the heater strip. The purpose of this thermocouple was to record the model's internal temperature (T_3 , in equation 4.5) to be seen.

A slurry of thermochromic liquid crystals with an evaporation temperature of 30 °C was sprayed onto the strip using an airbrush. The slurry was dried carefully between successive coats by using a heat gun. Several coats were applied until very distinct color patterns were seen.

Figure 4.18: Inconel Before Painting



A K-type cement-on thermocouple was attached to the tunnel wall immediately upstream of the model to allow measurement of the free stream temperature. The leads A Multivac Pro 360 digital potentiometer was attached to the wing tip using an angle iron bracket. The bracket was carefully positioned along the chordline so that the potentiometer readout would display the angle of attack. The digital potentiometer has a resolution of $\pm 0.1^\circ$. A Maxwell Electronics Inc. x-y stepping motor controller was used to drive the angle of attack adjust motor.

Figure 4.19: The Model in the ASWT

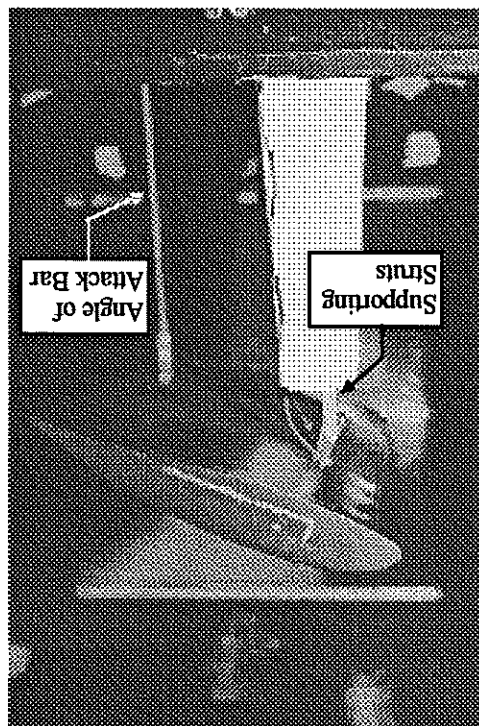


Figure 4.19.

The model was then installed in the test section of the ASWT. Two struts supported the model, and a metal rod connected to the lower surface of the model near the trailing edge provided a means for angle of attack adjustment. These features can be seen in the photograph. The calibration slope was determined to be 1.0452 Pa/Pa .

test section dynamic pressure versus the contraction pressure drop was constructed. The

4.2.8. Liquid Crystal Calibration

The liquid crystals were calibrated to obtain a hue versus temperature relationship. Details regarding liquid crystal calibration are available in Section 4.2.14 in which the calibration for the LSLTT tests is described. Figure 4.20 summarizes the ASWT setup. The liquid crystals were calibrated to obtain a hue versus temperature relationship. The liquid crystal coated surface was avoided by only illuminating the lights when data were being taken.

The liquid crystal illumination for the liquid crystal coated heater strip. Direct radiative heating of incandescent light bulbs in reflectors were positioned on either side of the test section to provide illumination for the liquid crystal coated heater strip. Two 200 Watt translation image processor which was inside a 386 personal computer. Data would be horizontal in the image. The camera video output was connected to the Data that was built for that specific purpose. The camera was positioned so that the heater strip the heater strip on the upper surface of the model through a five inch wide Lucite window A Sony 8mm video camera was mounted above the test section. The camera viewed Section 4.2.8.

A Hewlett Packard 6261B DC power supply was used to apply a voltage across the heater strip. A TSI integrating voltmeter was used to display the voltage that was applied across the heater strip. A discussion of the actual wiring for the heater strip is available in that provided a zero °C reference point electronically. The voltage from the compensator mechanical voltage scanner was connected to an Omega-CJ cold junction compensation that connected to a mechanical voltage scanner. The single set of leads coming from the from this thermocouple as well as the thermocouple leads coming from the model were connected to a mechanical voltage scanner. The single set of leads coming from the

The DC power supply was turned on, and the voltage level was increased slowly until color first began to appear on the heater strip. At this point, the heat transfer was allowed

the flow speed until the required pressure drop was reached.

across the contraction section was determined. The wind tunnel was then run, increasing pressure was computed, and through the tunnel calibration the necessary pressure drop preceding a given experiment. From this velocity the required test section dynamic Reynolds number of 315,000 was calculated based on the atmospheric conditions

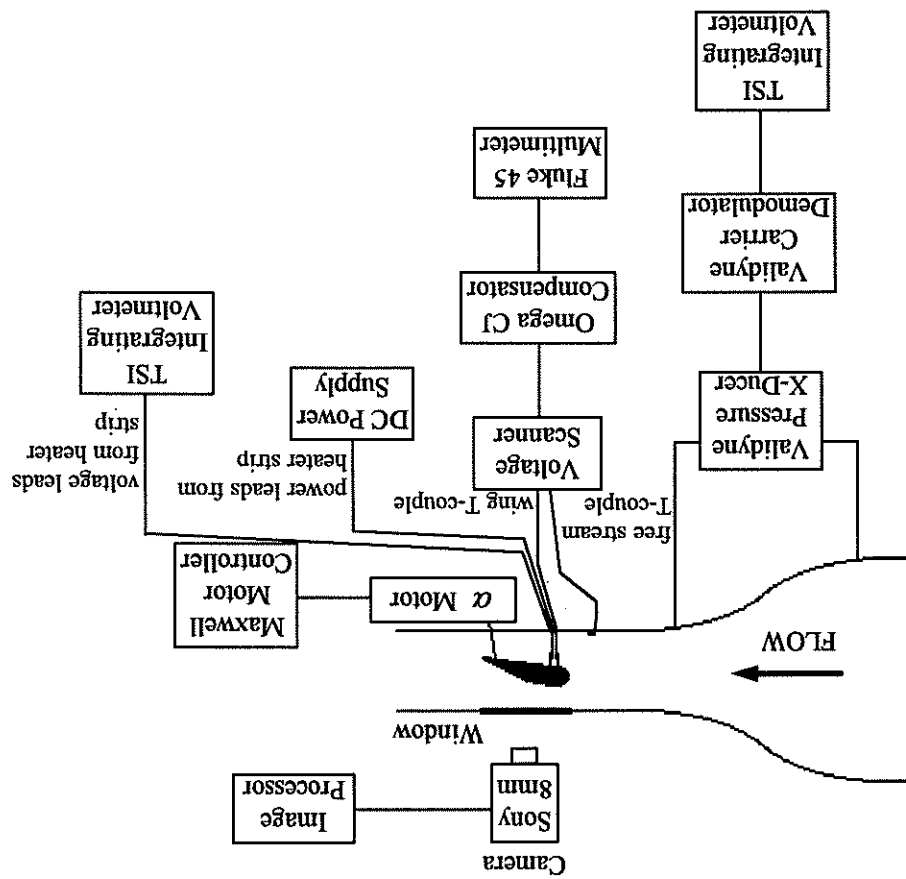
After setting the desired angle of attack, the velocity necessary to achieve a target

number of 315,000. Angles of attack tested included 0, 5, and 10 degrees.

contrast under the incandescent lighting system. Tests were conducted for a Reynolds number of 315,000. All experiments were conducted during the night to maximize the liquid crystal color

4.2.10 ASWT Experimental Procedure

Figure 4.20: Schematic of ASWT Heat Transfer Experimentation Setup



Once steady state was reached, the voltage applied across the heater strip was recorded along with the free stream and internal thermocouple output voltages. The incandescent lights were then illuminated. An image of the color pattern on the heater strip was then grabbed with the camera, providing security in the event of a problem with the original image taken by the image processor. The lighting system was then turned off. Operating the lights in this manner minimized the effects of radiation to the heater strip from the lights in the laboratory. The effects of radiation to the heater strip from the lights in this manner minimized the effects of radiation to the heater strip from the lights in the laboratory.

Steady state was determined by watching the color pattern on the heater strip and by observing to reach steady state. A time of approximately 10 minutes was usually sufficient. Steady

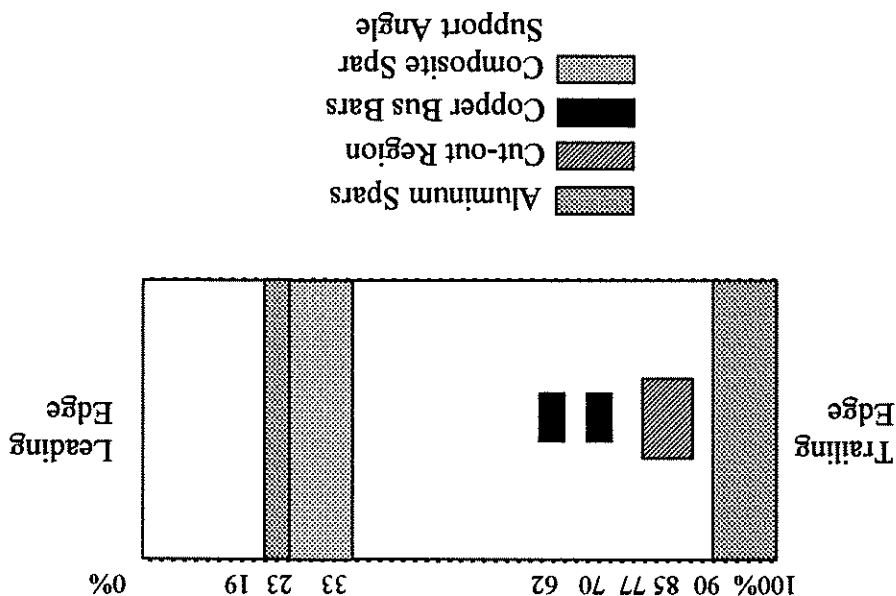
Results of the initial heat transfer tests in the ASWT are presented in Figure 4.36 in Section 4.2.16 on the same graph as results for experimentation in the LS LT. Only the zero degree angle of attack case is presented because problems encountered rendered other data taken in the ASWT very difficult to interpret. The intent of testing in the ASWT was not to interpret the h maps generated, but to determine any underlying problems that should be addressed before experimentation began in the LS LT. The data generated in the LS LT would be fully analyzed and interpreted (Sections 4.2.16 to 4.2.18).

Many problems did arise during this initial experimentation that reduced the accuracy of the heat transfer coefficients obtained. One of these problems involved the width of the heater strip. Edge effects on the color patterns reduced the region of the heater strip in which valuable data could be taken by about 50%. See Figure 4.21. Only the middle half of the strip provides a two-dimensional color band that may be used for determining average hue values at a given chordwise location. Because of this reduced region of valuable data, the lower limit on the total number of pixels in a given column that must pass the hue and intensity criteria had to be very low in order to obtain data at each chordwise station. Thus hue averages suffered because of these edge effects. This passes the hue and intensity criteria had to be very low in order to obtain data at each chordwise station. Thus hue averages suffered because of these edge effects. This chordwise scatter in the h maps and necessitated the use of an averaging technique. The data presented in Figure 4.36 of Section 4.2.16 have been averaged to achieve a smooth line.

4.2.11 Problems Discussed and Known During ASWT Tests

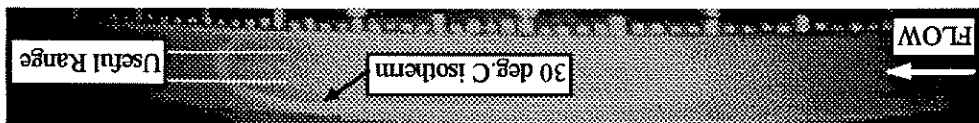
During the experiment, and a final compilation of the h, x/c points was made. Column passing both criteria were averaged, and this average hue was converted to a temperature through the liquid crystal calibration. The chordwise location of the column of pixels was recorded, thus providing the necessary information for a single h, x/c data point. The image processor then moved on to the next chordwise location scanning for pixels that passed both required criteria. This process was repeated for all images taken during the experiment, and a final compilation of the h, x/c points was made.

Figure 4.22: Sketch of Inside of Model for ASWT Tests



Another problem involved the internal layout of the wing model as shown in Figure 4.22. The heater strip (located on the outside of the wing) had to pass over several internal features of the wing: the main aluminum spar, a composite spar support angle that held the main spar in position, the copper bus bars, a cutout area that was required to provide clearance for the angle of attack mount, and the trailing edge aluminum spar. All of these internal features affected the conduction losses from the heater strip. This situation would have to be remedied to provide more confidence in the experimentally determined h values.

Figure 4.21: Edge Effects on the Heater Strip Color Pattern



Not only did the extensions have to increase the wingspan by over 10 inches, but they also needed to allow easy attachment of the wing to a horizontal rotary indexing table below the test section and a $\frac{3}{4}$ inch rotary bearing above the test section. The indexing table would allow the wing angle of attack to be adjusted.

Below the test section and a $\frac{3}{4}$ inch rotary bearing above the test section, the indexing table was designed to connect the lower wing extension to the model. This mounting piece that was designed to connect the lower wing extension to the indexing table is shown in Figure 4.23. It was built by machining a solid aluminum bar and tapping a piece of $\frac{1}{4}$ inch thick steel sheet.

4.2.2.1 Fabrication of the Wing Extensions

4.2.2 Modifications to the Model Prior to LSLT Heat Transfer Experimentation

The internal thermocouple was also seen to be a problem in that it only provided an average temperature for the inside of the model. The conduction loss term would again suffer because of this shortcoming.

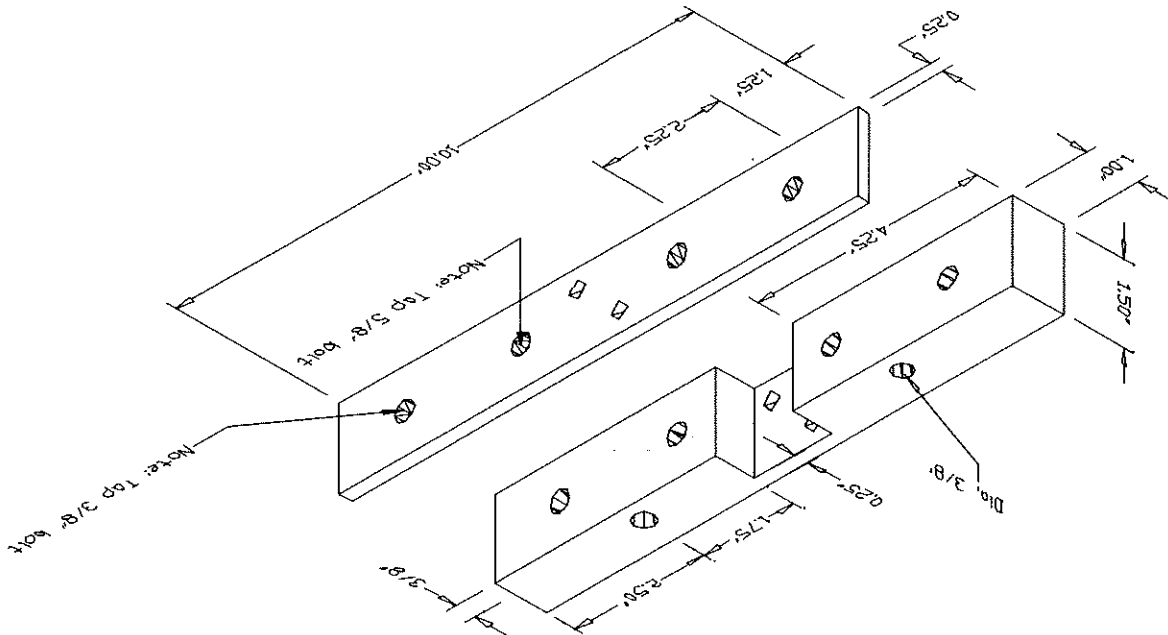
In addition to these problems, the lighting was not deemed to be satisfactory. Much intensity was lost through the wind tunnel Plexiglas windows. This was seen to be a possible problem in that if the intensity of the colors on the heater strip dropped too low, the color image CCD sensor would not provide an accurate hue value (Kim, 1991).

All of these problems had to be addressed before testing could begin in the LS LT. The following section discusses the modifications made to the model and the solutions to the problems discovered during heat transfer experimentation in the ASWT.

The internal thermocouple was also seen to be a problem in that it only provided an average temperature for the inside of the model. The conduction loss term would again

The wing extensions were designed to increase the overall span of the model to 44 inches. This length allows slightly over one inch to protrude both above and below the test section ceiling and floor boards when the model is installed in the LS TT. Drawings of the extensions are shown in Figure 4.24a and 4.24b. The bottom extension was constructed from a solid aluminum bar 18 $\frac{1}{4}$ inches long with a 1 $\frac{1}{2}$ x $\frac{3}{4}$ inch cross section. These cross section dimensions were calculated from a simple beam bending and twisting analysis using the maximum predicted aerodynamic loads. The top extension utilized 18 inch long aluminum bar with the same cross section as the bar of the bottom extension. However, in addition to the aluminum bar, the top extension was built with a $\frac{3}{4}$ inch diameter rod protruding from the aluminum bar. This rod allowed an easy interface with the rotary bearing on the top of the wind tunnel. Figure 4.25 shows the model with extensions mounted in the LS TT.

Figure 4.23: Rectangular Indexting Table Mount



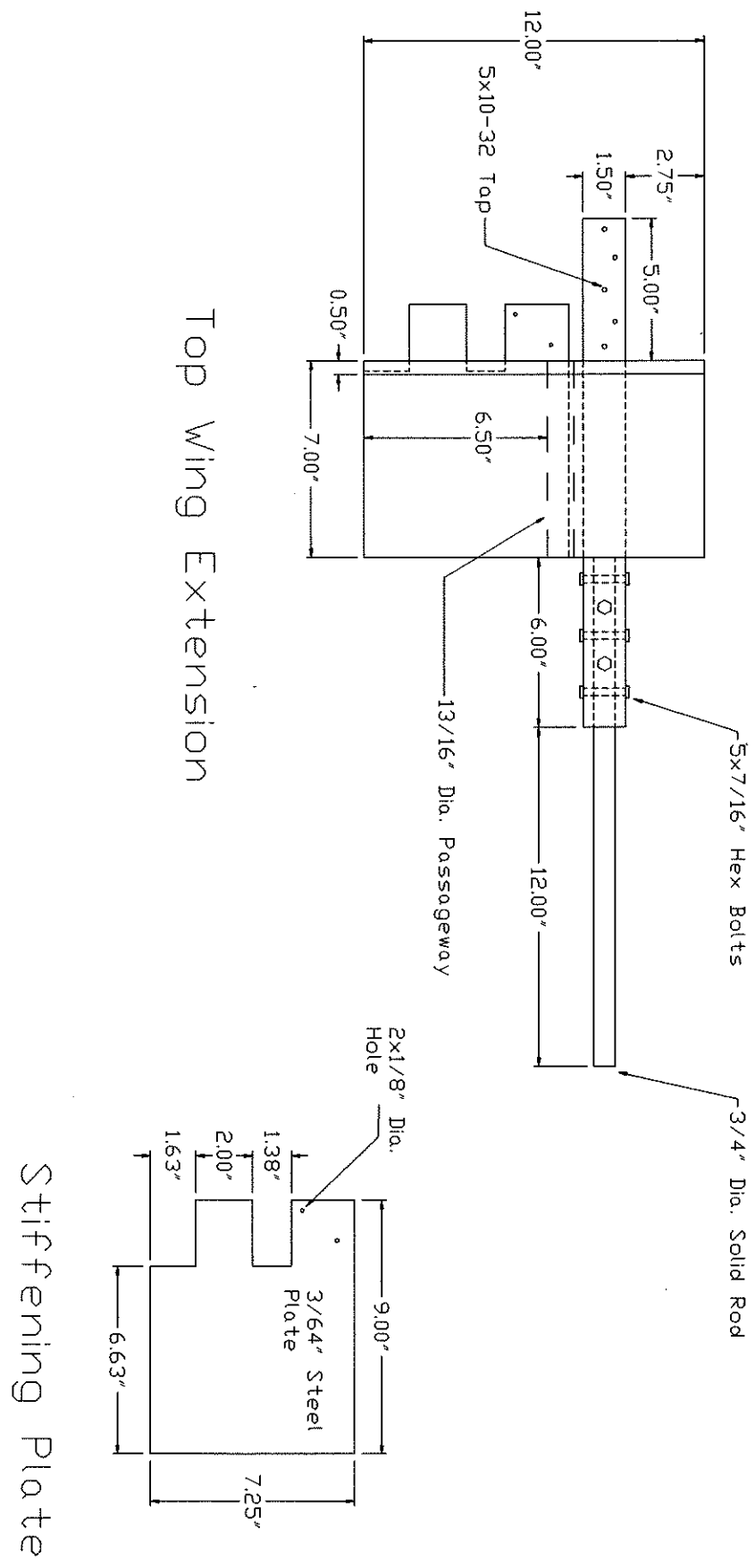


Figure 4.24a: Top Wing Extension (lower surface view)

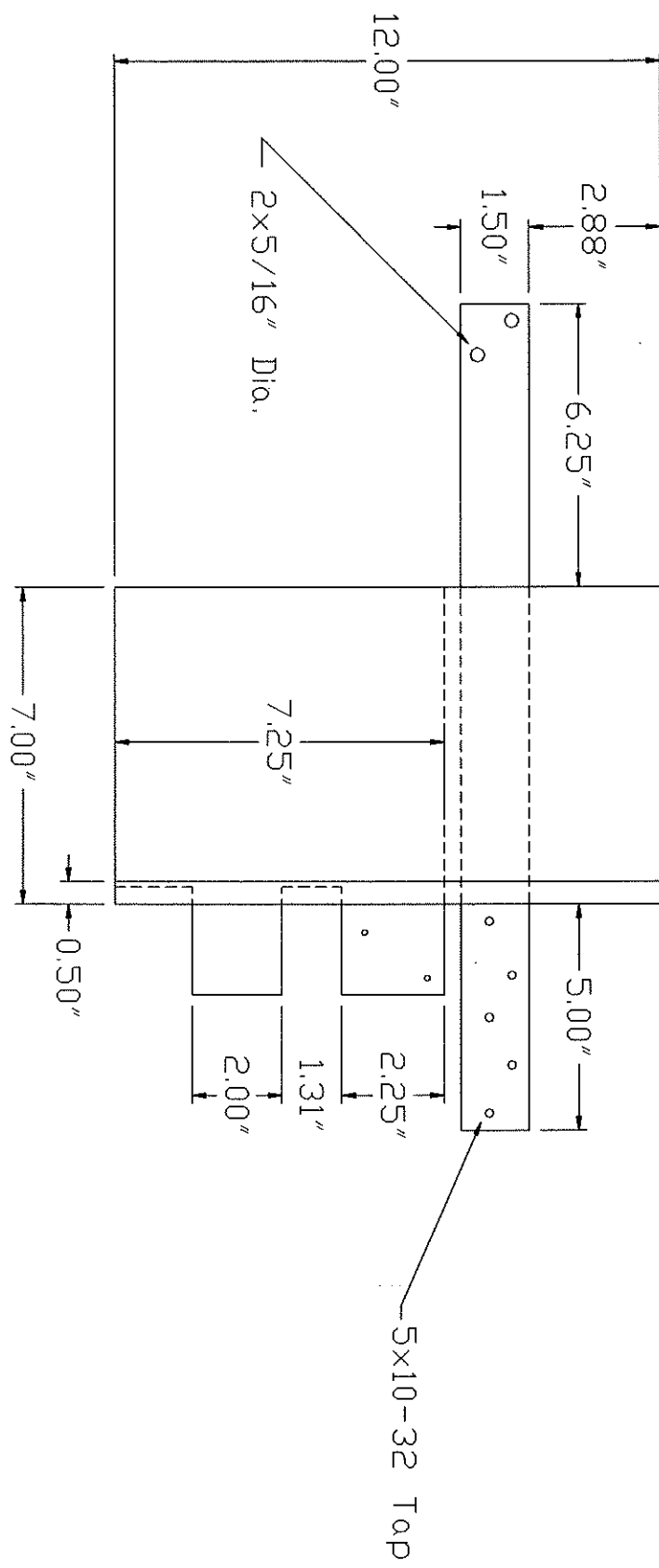
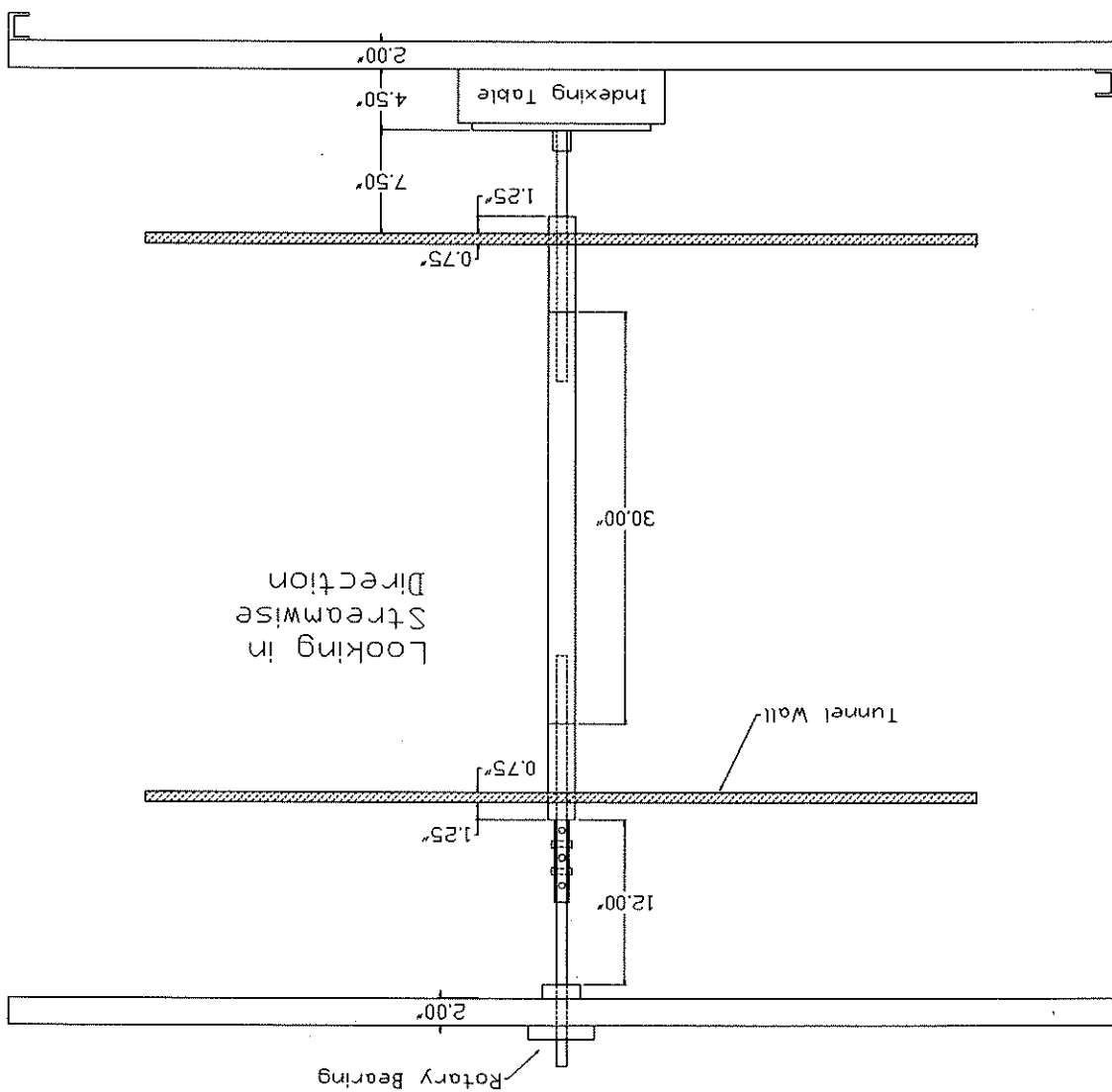


Figure 4.24b: Bottom Wing Extension (lower surface view)

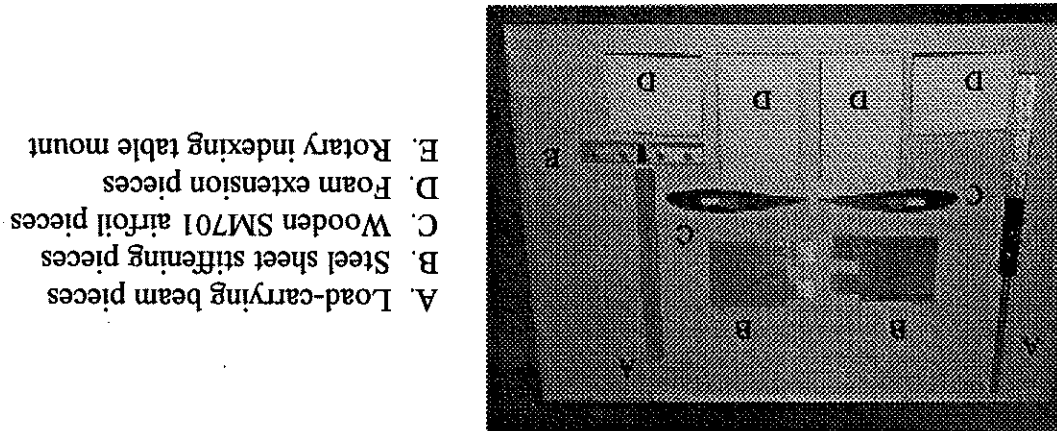
(NOTE: Vertical LS LT components not drawn.)

Figure 4.25: Model with Extensions Mounted in LS LT



To ensure precise alignment when attaching the aluminum beam pieces (A) to the main wing spar at both wing tips of the model, a small-10 mW helium-neon laser made by Hughes Aircraft Company was used. A small piece of Formica was cut so that it rode along the aluminum beams. The laser beam was first aligned with the leading edge of the wing. The laser was then traversed until it hit a vertical line on the Formica piece. By sliding the Formica along the length of the beam, adjustments could be made such that the beam was precisely aligned. Both extension beam pieces were aligned in this manner. See Figures 4.27a and 4.27b.

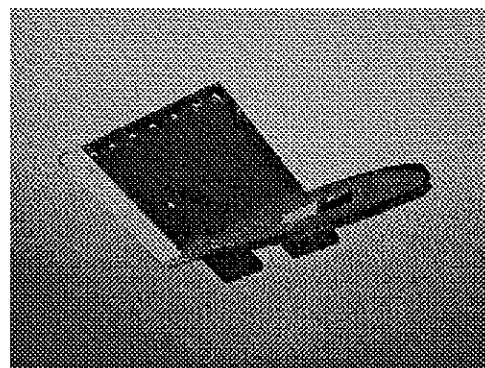
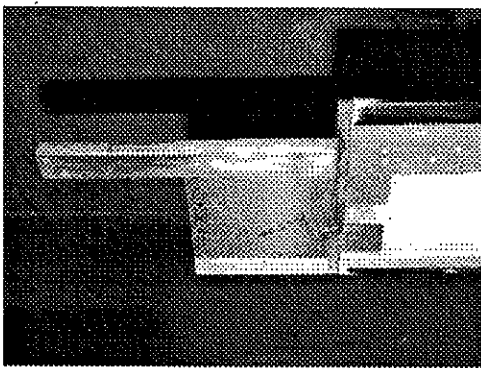
Figure 4.26: Wing Extension Pieces Before Assembly



A series of photographs is now presented to clarify the design and fabrication of the wing extensions. Figure 4.26 shows all the pieces that were built to construct the wing extensions. Figure 4.26 shows all the pieces that were built to construct the wing extensions.

Extension Assembly

Figure 4.28a: Beginning Wing



The stiffening piece (B) was inserted through the slot in the wooden SM701 airfoil piece (C). See Figure 4.28a. The trailing edge has been moulded from Evercoat professional body filler (bondo). This provides more durability than using foam for the thin trailing edge.

The assembly of the bottom extension will be discussed. The top extension was assembled in the same manner.

After this alignment was completed, the assembly of the extensions could continue. The assembly of the bottom extension will be discussed. The top extension was assembled in the same manner.

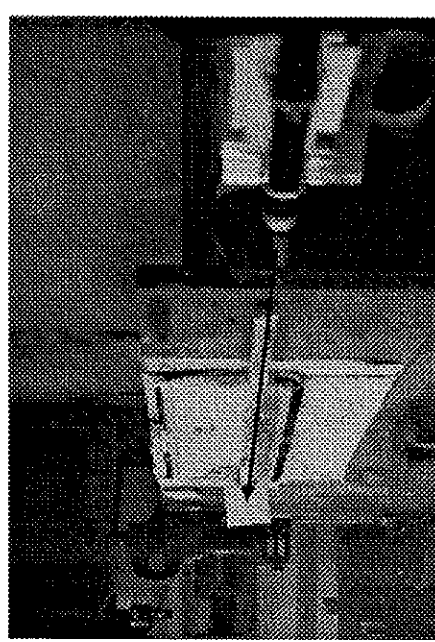
Carrying Beams

Figure 4.27a: Aligning Load-



Carrying Beams (cont.)

Figure 4.27b: Aligning Load-



A means had to be devised to pass internal wires out of the wing through one of the extensions. A 13/16 inch inner diameter metal pipe was used to form a passageway through the left wing tip extension. The pipe was heated with a propane torch and pressed into the extension immediately behind and parallel to the load carrying beam. The high temperature of the pipe allowed it to melt easily through the foam extension piece forming a passageway for the internal wires.

Figure 4.28d: Attachment of Final Foam Piece

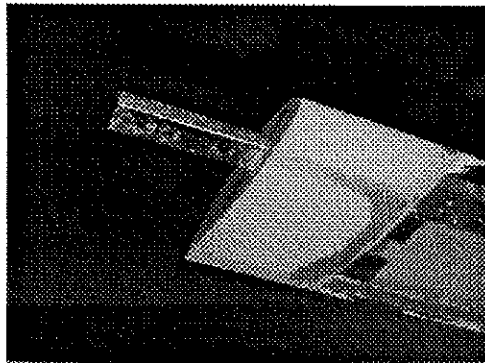


Figure 4.28c: Attachment of First Foam Piece



Upon final sanding, the extension appeared as in Figure 4.28e. A second foam extension piece was then glued to the assembly to complete the airfoil shape. Bondo was applied to seal remaining gaps. This can be seen in Figure 4.28d. A second foam extension piece was then glued to the assembly to complete the airfoil was completed with 100 and 400 grit sandpaper to achieve fairly smooth surfaces. Coming Formular 150 insulating foam. Formica SM701 airfoil templates were first glued on either side of the foam blocks. A taut wire was then heated by passing a current through it, and the wire was used to slice the desired shapes out of the foam. Finishing on either side of the foam blocks. A taut wire was then heated by passing a current as seen in Figure 4.28c. The foam extension pieces had been cut from blocks of Owens A foam extension piece (D) was then glued to the stiffening piece (B) with the epoxy (C).

minute epoxy was applied to attach the stiffening piece (B) to the wooden airfoil piece wing. See Figure 4.28b. Once the pieces were checked for proper positioning, Devcon 5 and the entire assembly was attached to the main wing spar at the appropriate tip of the The load-carrying beam was then inserted through the wooden SM701 airfoil piece,

Figure 4.28F: Complete Extensions
Before Covering

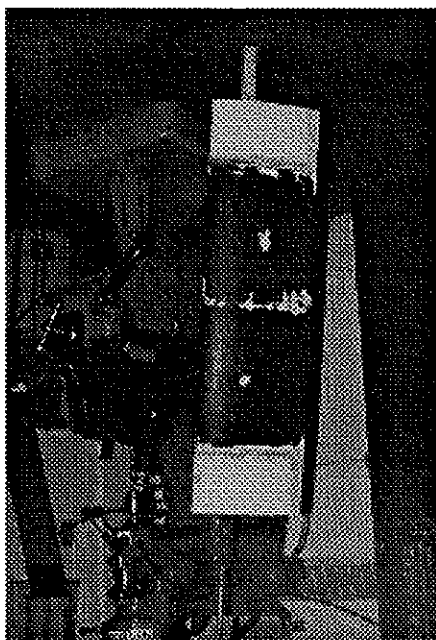
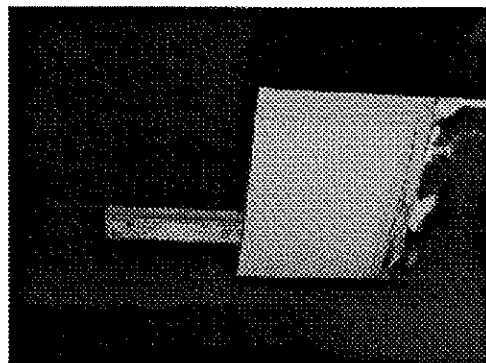


Figure 4.28E: Extension After
Sandining



Both extensions can be seen attached to the model in Figure 4.28C. This picture was taken before the model received a final coat of black paint. The wing extensions were later covered with Top Flite Monokote (a heat-shrink plastic covering) to provide a smooth surface. Problems were encountered in this final step. The heat from the Hobbyco custom sealing iron that was used to apply the plastic Monokote covering caused slight extensions were located far from the center span region of the model where the heat not entirely smooth. This was not seen to be a major problem, however, since the bumps to form in the foam of the extension piece. Thus, the final finished extensions were transfer measurements would be taken. The extensions could be improved by re-sanding and applying a layer of E-glass epoxy fiberglass instead of the Monokote plastic covering.

To address the problem of edge effects on the heater strip color patterns, it was decided to increase the width of the heater strip from one inch to three inches. This would create a much larger region along the center of the strip in which the color bands would be two-dimensional. As a result of this change, a better average hue value would be attainable, and the scatter encountered in the ASWT h maps should be diminished.

The problem of the internal geometry of the wing as seen in Figure 4.22 of Section 4.2.11 was remedied by shifting the entire heater strip from the midspan by $4\frac{1}{4}$ inches. Oil flow visualization had shown that the flow would still be two-dimensional in this new location, and by shifting the heater strip the cutout region near the trailing edge could be avoided. In addition, the composite spar support angle was cut away from the new location of the heater strip, and the new forward bus bar was built so that it did not interfere with the upper surface of the wing. Thus the heater strip only had to pass over the main aluminum spar, the aft bus bar, and trailing edge aluminum spar. The problems with the composite spar support angle, the forward bus bar, and the cutout region, totaling approximately 22% of the chord, were eliminated.

An internal array of eight thermocouples was installed along the inside of the upper surface to eliminate the uncertainty of only using one thermocouple. Internal temperatures at chordwise locations would be determined by linearly interpolating between the nearest thermocouples. The problem with lighting was addressed by increasing the power of the bulbs from 200 Watts to 500 Watts. The lights were placed on variable ac (variac) power supplies so that the best light intensity could be achieved.

A final improvement was made for the experimentation in the LSLT. A FORTRAN data acquisition code was written to sample the necessary voltages during the testing. A DAS20 board manufactured by Metabyte Corporation was used to digitize the analog voltage signals. This FORTRAN code is listed in Appendix C as the program getdata.for.

4.2.12.2 Model Changes Due to Knowledge Gained from ASWT Tests

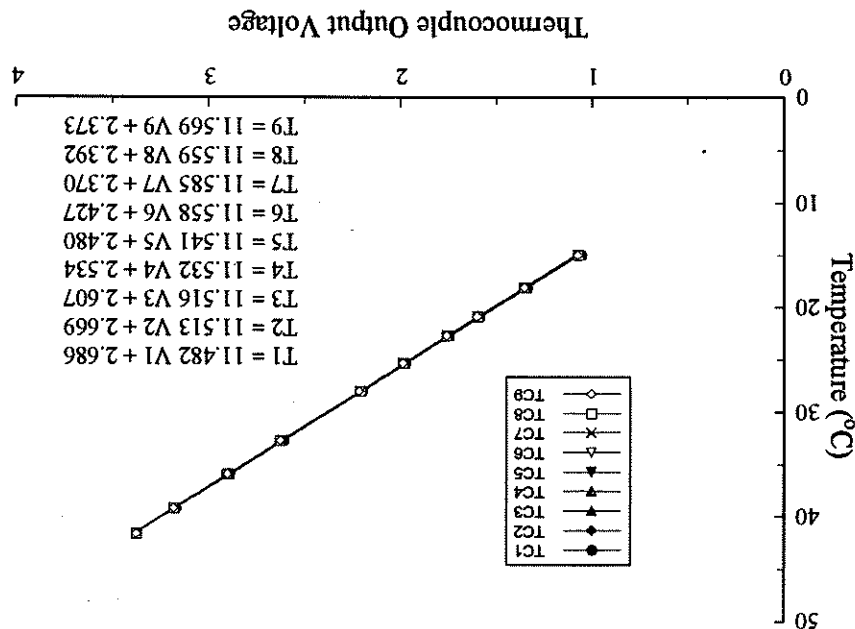
4.2.13 LSLT Setup for Heat Transfer Experimentation

Before the model could be installed in the test section, the eight thermocouples comprising the internal thermocouple array as well as a thermocouple to be used to measure free stream temperature had to be calibrated. These nine thermocouples were connected to a mechanical voltage scanner. The single set of leads coming from the voltage scanner was connected to a MEPTS-9000B main unit to provide signal conditioning and amplification of the thermocouple output voltages. The conditioned output of the thermocouple signal was then sent to channel 2 of the DAS20 interface. A hot water bath was prepared in a one gallon insulating thermos. The nine thermocouples were placed in the bath along with a certified (NIST) thermometer against which the thermocouples would be calibrated. Calibration corrections for the thermometer were supplied by Brooklyn Thermometer Company, Incorporated. The water was stirred to achieve a good equilibrium temperature, and each thermocouple output voltage was sampled by the DAS20 board by rotating the dial of the voltage scanner. Cold water was added to the thermos to lower the temperature between calibration points. The calibration slopes for the nine thermocouples are seen in Figure 4.29.

The tunnel was then calibrated in the same manner as discussed in Section 4.2.9 for the ASWT. A \pm 10 inch H₂O and a \pm 1 psi differential pressure transducer purchased from Techkor Instrumentation were used in this calibration process to record the pressure drop across the contraction section and the test section dynamic pressure, respectively. The pressure transducers were connected to a MEPTS-9000A main unit that provided signal conditioning and amplification. A Metram Instrument hand pump was used to calibrate the pressure transducers against a Metram Instrument manometer. The output voltage of the pressure transducers against a Metram Instrument manometer was fed into the DAS20 pressure transducer connected across the tunnel contraction. The output voltage of the pressure transducers was recorded by a MetraByte DAS20 A/D board inside a Compaq Deskpro 386s personal computer.

The model was mounted vertically in the center of the test section. Beneath the test section, a rotary bearing held the wing in place as shown in Figure 4.31. More to the test section, a rotary indexing table with the wing mounted. Above the wing, a rotary indexing table which allowed angle of attack to be changed. Figure 4.30 shows the rotary indexing table with the wing mounted. Above the test section, the model was secured to a rotary indexing table which allowed angle of attack to be changed. Figure 4.30 shows the rotary indexing table with the wing mounted. Above the test section, the model was secured to a rotary indexing table which allowed angle of attack to be changed. Figure 4.30 shows the rotary indexing table with the wing mounted.

Figure 4.29: Calibration of the Nine Thermocouples



A Sony 8mm video camera mounted on a tripod viewed the heater strip on the upper surface of the model through the side windows of the test section. The heater strip was horizontal in the camera viewfield. The camera video output was connected to the Data Translation image processor inside a 286 personal computer. Two 500 Watt incandescent leads wired to the heater strip was fed into channel 1 of the DAS20 interface to allow the strip through a set of leads attached to the bus bars inside the model. A second set of leads wired to the heater strip was used to apply a voltage to the heater applied bus-to-bus voltage to be recorded.

Figure 4.31: Rotary Bearing Mount
Above Test Section

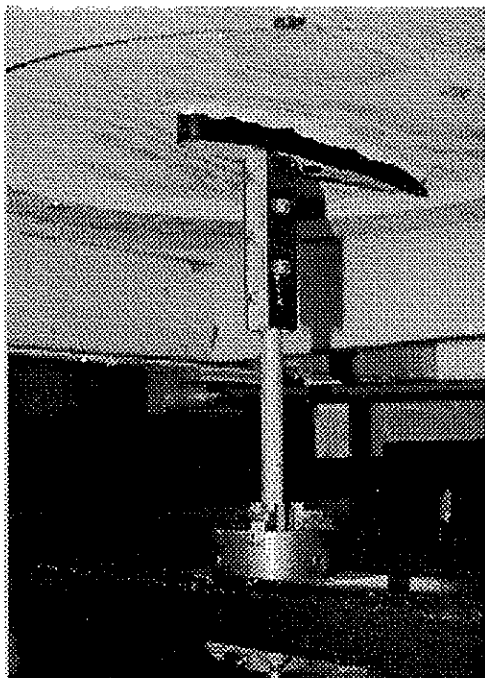
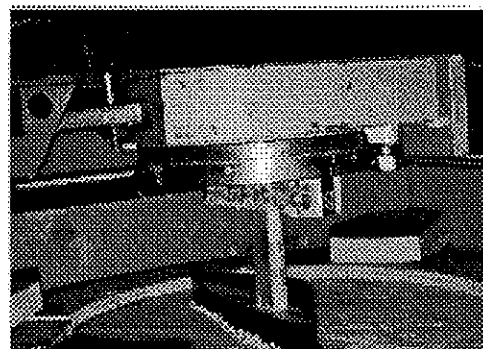


Figure 4.30: Model Mounted to
Rotary Indexing Table



Weatherstrip and Caulking Cord was used to seal any gaps between the model and the rotating wooden templates that interfaced with the test section.

light bulbs in reflectors were positioned to provide illumination for the liquid crystal coated heater strip.

Figure 4.32 shows the model mounted in the test section, and Figure 4.33 summarizes

the experimental setup for the LS LT heat transfer tests.

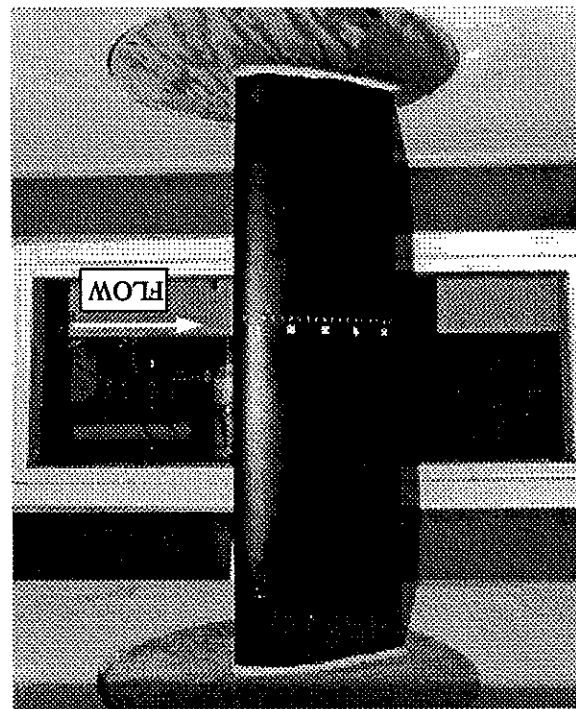


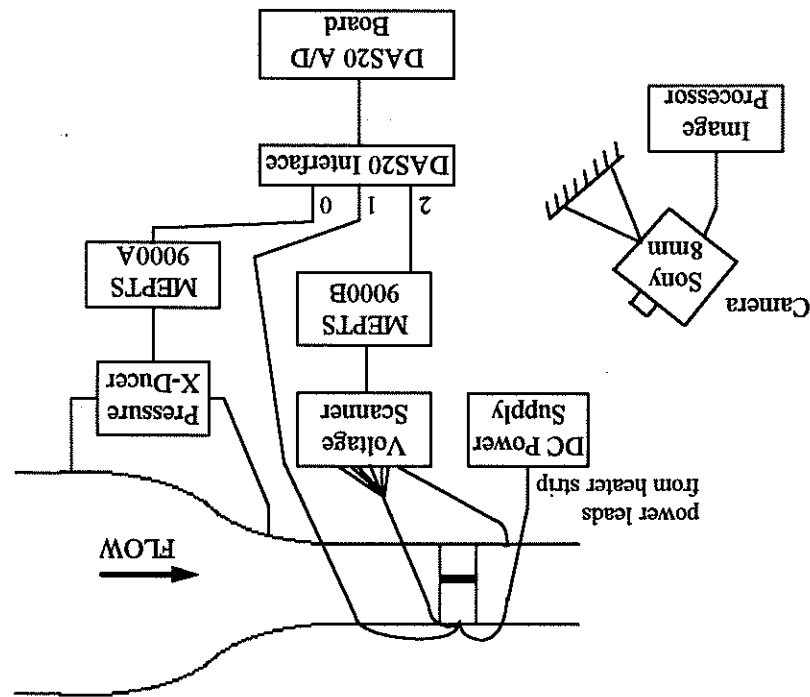
Figure 4.32: Model Mounted in LS LT Test Section (view of upper surface)

The calibration piece was next placed in the wind tunnel test section in the same location as the wing model's heater strip. Two 500 Watt incandescent lights were set up to illuminate the test section. The power of the lights was adjusted with the variac unit until a uniform lighting was present. The intensity of the illumination was checked with the image processor. A video camera was positioned to record the color response of the image processor piece along with a voltmeter readout of the thermocouple voltage in the same field of view.

Using the same slurry that was applied to the wing model's heater strip, thermochromic liquid crystals were then sprayed onto the black calibration piece using an airbrush. Before heat transfer tests could be conducted, the liquid crystal layer sprayed onto the heater strip first had to be calibrated. This was done by first affixing a K-type cement-on material was then spray painted black with the same paint that was used on the wing which was found to be a good insulator. The surface of this calibration piece of wing thermocouple (with a response time of 3 to 5 ms) to a scrap piece of the wing material which was found to be a good insulator. The surface of this calibration piece of wing heater strip was then sprayed onto the black calibration piece using an airbrush. Using the same slurry that was applied to the wing model's heater strip, thermochromic liquid crystals were then sprayed onto the black calibration piece using an airbrush.

4.2.14 Calibration of the Liquid Crystals

Figure 4.33: Schematic of LSLT Heat Transfer Experimentation Setup



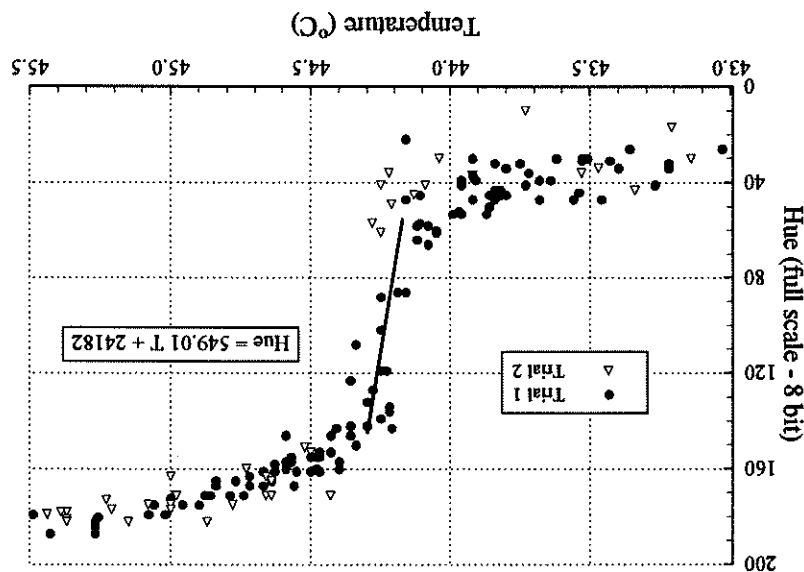
It is important to mention now that ideally the position of the lights should remain constant for both the liquid crystal calibration and the actual heat transfer experiments. For the current experimentation, however, it was necessary to slightly shift the lighting between tests. This was necessary since many different angles of attack were studied, and it was not practical to calibrate the liquid crystals for every different configuration. Had the lighting not been shifted, there would have existed regions of shadow at certain chordwise locations of the airfoil for the different angles of attack. While this slight shifting of the lights was not ideal, it was not expected to greatly affect the measurements. In fact, Kim found that the intensity of a pixel analyzed by the image processor did not greatly affect the measured hue value, the parameter to which the temperature is directly related. In performing a series of experiments in which he varied the intensity of the illumination of a liquid crystal coated surface, Kim discovered that the liquid crystal hue versus temperature linear slope calibration did not shift by more than $\pm 0.1^{\circ}\text{C}$ along the temperature axis. He summarized, "It was concluded that by significantly changing the intensity of illuminating light, the local hue values did not vary in a strong manner" (Kim, 1991).

The calibration piece was next heated through the event temperature range of the liquid crystals by using a Proheat heat gun. The wind tunnel windows were sealed just as would be the case when the airfoil is exposed to flow. The cooling of the calibration piece back down through the liquid crystal color event temperature range was videotaped. This transient process occurred in approximately 15-25 seconds. Had a better insulating material been used for the calibration piece, this time perhaps could have been increased. Using the image processor, video images of this cooling process were captured one at a time. The pixel overlaying the thermocouple sensor location was analyzed for hue a time. The pixel overlaying the thermocouple sensor location was analyzed for hue many frames of the video, and a hue versus temperature calibration graph was constructed as shown in Figure 4.34.

To perform a thorough liquid crystal calibration, Kim recommends that a plot of hue versus intensity also be constructed (Kim, 1991). He regards this as a useful tool in setting up the lighting for a successful heat transfer experiment. Kim explains that color image sensors do not provide accurate hue values if the local intensity drops below a value of approximately 50. Also if the local intensity exceeds 200, the accuracy of the hue values determined by the image processor suffers due to the saturation of the CCD sensor.

Uncertainty in the liquid crystal calibration is $\pm 0.25^{\circ}\text{C}$ for a given hue value falling in the linear range. From the experimental scatter, the uncertainty in the calculation of a temperature value due to the noise level inherent in commercially available CCD sensors (Mauldin, 1996) is estimated as $\pm 0.15^{\circ}\text{C}$. However, factoring in from a hue value in the linear range may be estimated as $\pm 0.1^{\circ}\text{C}$. The overall uncertainty in the thermocouple measurement (estimated as $\pm 0.1^{\circ}\text{C}$), the overall uncertainty in the liquid crystal calibration is $\pm 0.25^{\circ}\text{C}$ for a given hue value falling in the linear range.

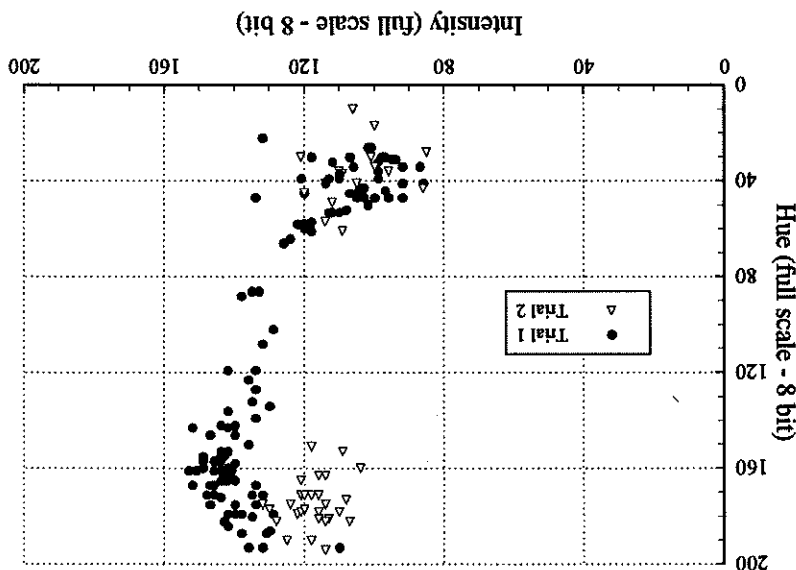
Figure 4.34: Liquid Crystal Calibration Graph



code used to analyze the images taken during experimentation and to calculate the internal thermocouple, the array of eight thermocouples was monitored. The FORTRAN acquisition was used for the LSLT tests, and instead of recording the output of a single used during the ASWT tests (Section 4.2.10) with a few differences. Computerized data attack tested included 0°, 5°, 10°, 15°, 18°, and 20°. The experimental procedure followed that Tests were conducted for Reynolds numbers of 315,000 and 750,000. Angles of

4.2.15 LS LT Experimental Procedure

Figure 4.35: Hue Versus Intensity Check for Liquid Crystal Calibration



calibration. For the most part, they fall into Kim's ideal range of 100 to 150. The intensity values are not in violation of Kim's recommendation for a good liquid crystal Such a plot was made for the current liquid crystal calibration as seen in Figure 4.35. repeated. Ideally, Kim suggests intensity levels between 100 and 150 (Kim, 1991). drop below 50 or climb above 200, the lighting should be adjusted and the calibration examine whether these intensity boundaries are exceeded. If the local intensity values Thus a hue versus intensity plot should be included in the calibration of liquid crystals to

convective heat transfer coefficients may be found in Appendix C. It is named potential flow solution will lead to errors in the predicted distributions. Since the main code used for the inviscid calculations can not take separation into account. This poor potential flow solution will suffer greatly at those higher angles of attack since the panel 20° is because at higher angles of attack, gross separation exists on the airfoil. The second reason for not making predictions for angles of attack of 15° , 18° , and 20° is that the laminar region is first predicted.

STAN5, the boundary layer code employed, to stop calculations when a reverse flow separation point fairly well. The parabolic nature of the boundary layer equations causes separation point to mark the location of the laminar

The predicted distributions are also seen to mark the rest of the airfoil is reported to be minimal (Crawford and Kays, 1975).

These sudden variations were most likely caused by the rapid initial development of the stagnation point existed for the predicted distributions (not shown on the graphs). boundary layer and the finite grid size in the x direction and in the y direction (normal to the airfoil surface). The influence of initial disturbances on the results presented for the rest of the airfoil is negligible caused by the rapid initial development of the stagnation point existed for the predicted distributions (not shown on the graphs). It should be mentioned that fluctuations in a small region near the distributions. It is agreed that fluctuations in a small region near the distributions between the predicted distributions and the experimentally determined experimental procedure as can be seen in Figures 4.36 to 4.41. In general, good agreement exists for the cases of $\alpha = 15^\circ$, 18° , or 20° . Two reasons exist for not making predictions at those angles of attack. First, the six predictions that were made adequately verified the made for the cases of $\alpha = 15^\circ$, 18° , or 20° . No predictions were made for the cases of $\alpha = 0^\circ$, 5° , and 10° . Figures 4.36 to 4.41. These figures cover angles of attack of 0° , 5° , and 10° . No predictions were theoretical heat transfer distributions (discussed in Chapter 3.0) are included in Figures

The first area to be discussed is the validity of the experimental approach. The

be made between the heat transfer method and the oil flow visualization results.

Figures 4.36 to 4.44 contain the heat transfer results of the LSLT tests. In addition to heat transfer information, each graph contains the corresponding oil flow visualization results as previously presented in Table 4.1 of Section 4.1.4. Easy comparisons can now

4.2.16 LS LT Heat Transfer Results

convective heat transfer coefficients may be found in Appendix C. It is named appwning for.

ASWT data shown in Figure 4.36 can be taken as a higher free stream turbulence levels in the ASWT and the LS LT, there are also different solid and wake blockage effects occurring in the two tunnels (see results of oil flow visualisation in Section 4.1.3). Stream turbulence intensity effects can not be made because, in addition to the different Tu large effect on the measured heat transfer data. Definitive conclusions regarding free ASWT leads to higher values of measured convective heat transfer coefficient. It is evident from the data of Figure 4.36 that the free stream turbulence intensity level has a very similar for both turbulence intensity levels, but the higher turbulence intensity in the A SWT version of the experiment performed in the LS LT. The trends in the h distributions are very similar for both turbulence intensity levels, but the higher turbulence intensity in the A SWT version of the experiment performed in the LS LT.

These flat plate predictions further verify the experimental method employed by predicting low turbulence wind tunnel environment of the LS LT. Layer prediction method (STAN5) produces very good agreement with the h data from the measured h data range with reasonable success. A more accurate differential boundary the measured h data range with reasonable success. A more accurate differential boundary layer prediction method (STAN5) produces very good agreement with the h data from the measured h data range with reasonable success. A more accurate differential boundary

$$C_f = \frac{0.0592}{Re_x^{1/4}} \quad \text{turbulent flow} \quad (4.10)$$

$$C_f = \frac{0.664}{\sqrt{Re_x}} \quad \text{laminar flow} \quad (4.9)$$

$$St = \frac{\rho U_e C_p}{h} = \frac{2 Pr_e^{1/3}}{C_f} \quad (4.8)$$

1986) for the turbulent case (equation 4.10). Figures 4.36 and 4.37 also contain flat plate laminar and turbulent heat transfer distributions under the appropriate test conditions. The predictions were made using the Reynolds analogy relating convective heat transfer to skin friction, equation 4.8. The skin friction coefficients were calculated using the Blasius solution for the laminar case (equation 4.9) and an empirical equation suggested by McLoughlin (Neumann and Hayes,

purpose of making theoretical predictions was to verify the experimental method (which had been accomplished at the lower angles of attack), no effort was made to obtain accurate h predictions at the higher angles of attack.

Figure 4.37: h Map for $\alpha = 0^\circ$, $Re = 750,000$

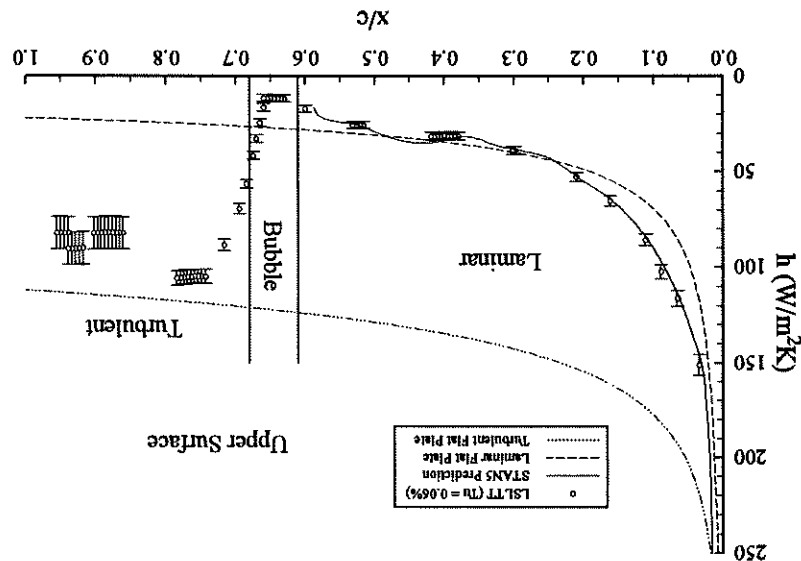


Figure 4.36: h Map for $\alpha = 0^\circ$, $Re = 315,000$

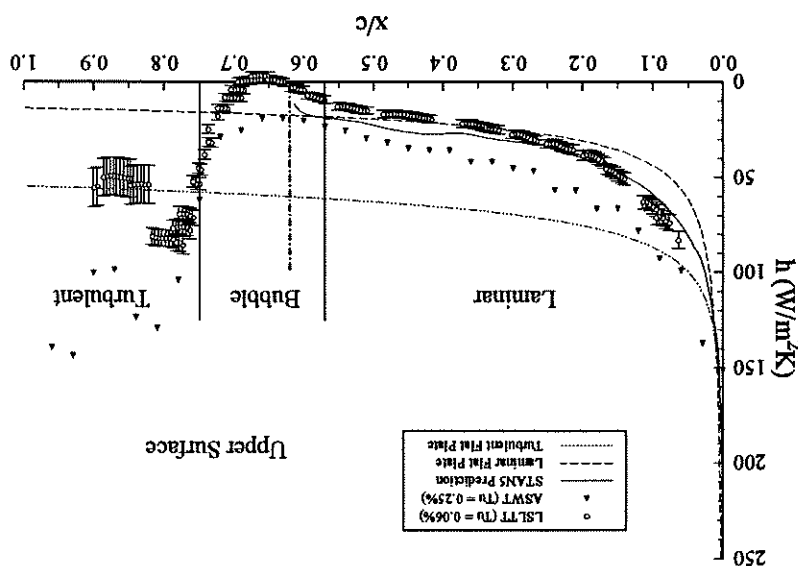


Figure 4.39: h Map for $\alpha = 5^\circ$, $Re = 750,000$

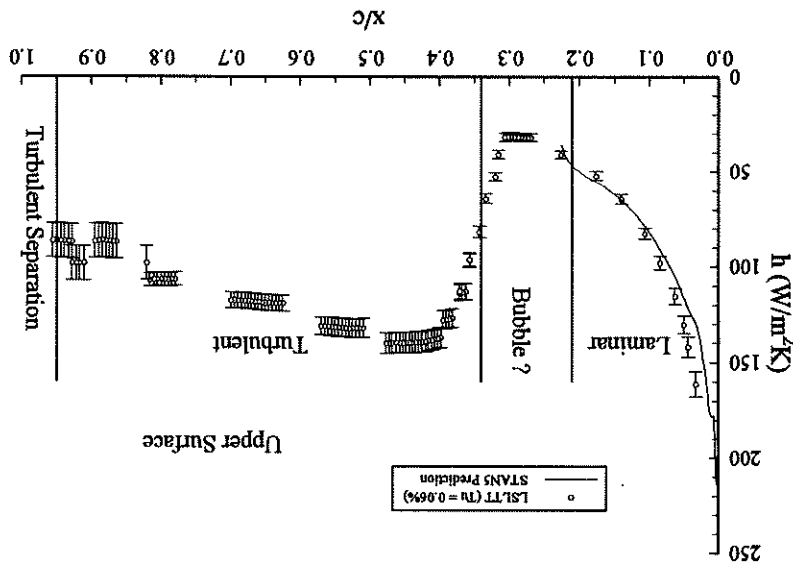


Figure 4.38: h Map for $\alpha = 5^\circ$, $Re = 315,000$

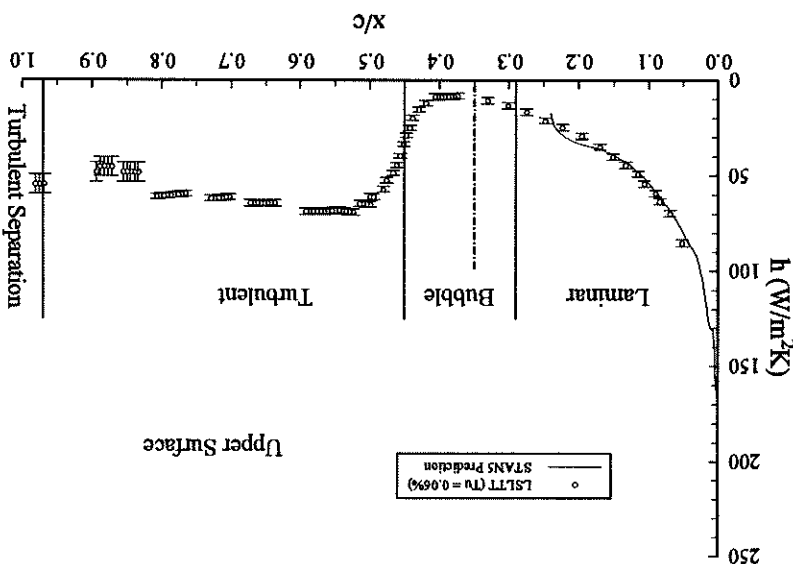


Figure 4.41: h Map for $\alpha = 10^\circ$, $Re = 750,000$

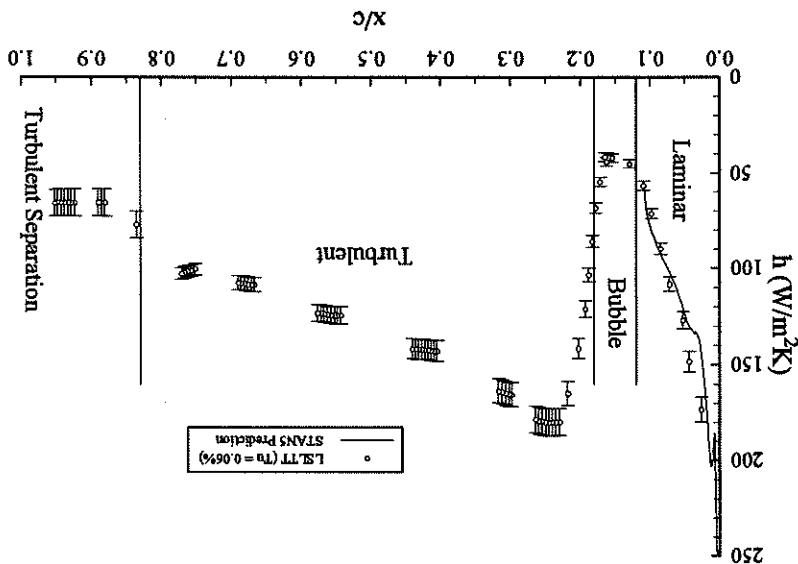


Figure 4.40: h Map for $\alpha = 10^\circ$, $Re = 315,000$

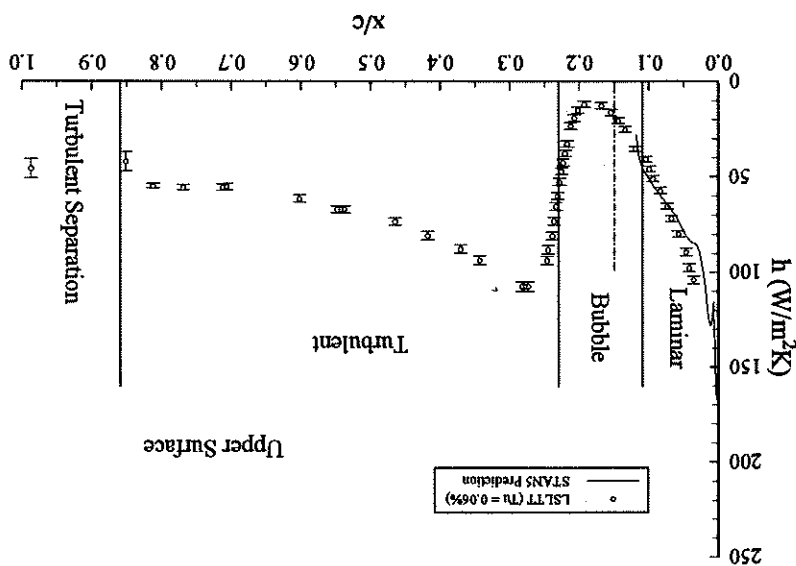


Figure 4.42: h Map for $\alpha = 15^\circ$, $Re = 750,000$

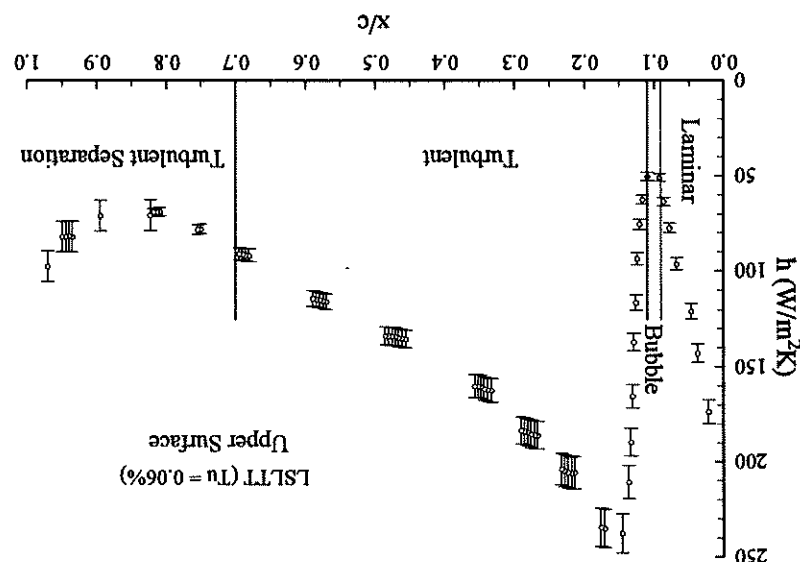
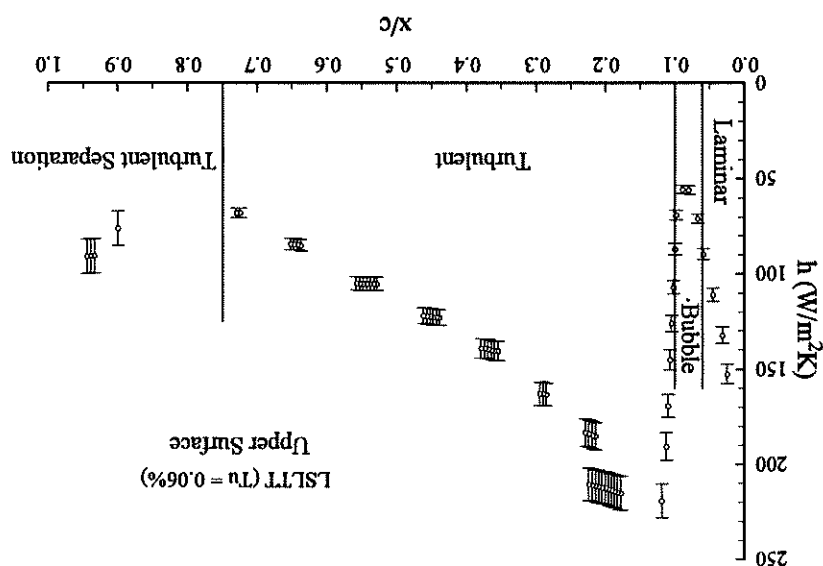
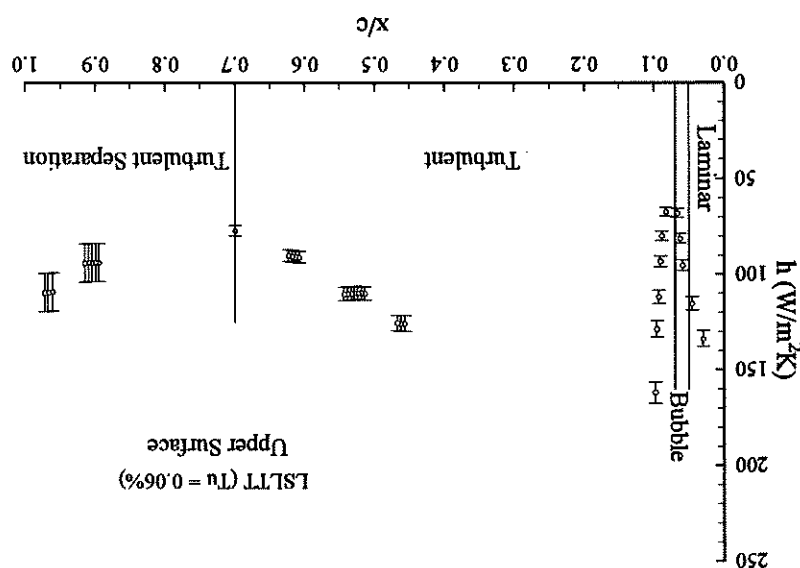


Figure 4.43: h Map for $\alpha = 18^\circ$, $Re = 750,000$



(NOTE: Image processor malfunctioned during testing resulting in incomplete data.)

Figure 4.44: h Map for $\alpha = 20^\circ$, $Re = 750,000$



The main reason for performing the heat transfer experiments was to determine if the h maps could provide a good quantitative description of different flow regions existing on the airfoil. This topic will now be explored.

Examining Figures 4.36 to 4.44, it is seen that the laminar regions are marked on the h maps by a decaying trend. This trend is a result of the developing thermal boundary layer. The turbulent regions are also seen to display a decaying trend in the h distribution for the same reason as mentioned for the laminar boundary layer. The laminar and turbulent separated regions are seen to be well marked by the heat transfer method. Results concerning the regions are seen to be well marked by the heat transfer method. Results concerning the change in the h distribution occur at the laminar separation point. The h distribution reveals no indication of laminar separation for any of the other experimental cases as seen in Figures 4.37 to 4.44.

This general failure of the heat transfer method to indicate laminar separation can possibly be explained by examining the nature of the forward portion of the laminar separation bubble and the laminar flow leading up to it. In general, the momentum of the fluid particles in the laminar flow approaching the separation bubble is being overcome by viscous and adverse pressure effects. By the time laminar separation occurs, the laminar boundary layer has been drained of most of its momentum. Laminar separation then does not bring about a drastic change to the near wall flow properties.

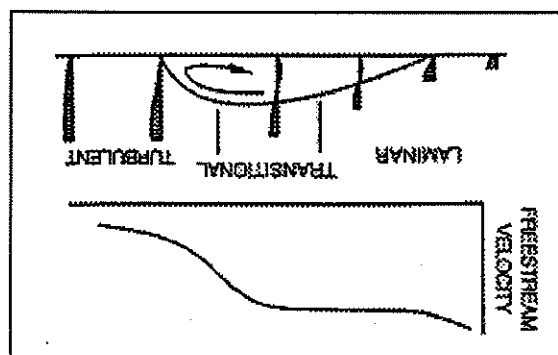
Now, looking into the laminar separation bubble, Mallikel and Mayle found that the forward portion of a laminar separation bubble is a constant pressure region which grows rather slowly (Mallikel and Mayle, 1996). As can be seen in Figure 4.45, a nearly constant free stream velocity exists over the forward portion of a laminar separation bubble. Because of this relatively uncoupling velocity and the extreme thinness of the laminar separation region at the bubble's onset, the heat transfer characteristics would not be expected to radically alter at the beginning of the bubble. The data of Figures 4.37 to 4.44 reflect this hypothesis.

The flow reattachment at the end of the laminar separation bubble as marked by the oil flow visualization method is seen to occur in the region of the h distribution that exhibits the largest heat transfer coefficient gradient. This is especially obvious in Figures 4.36 to 4.41 in which large laminar separation bubbles exist. The local maximum heat transfer coefficient is seen to exist slightly downstream of the reattachment location. Rivir et al. (1994) found a similar result when examining a turbulent reattaching flow on a flat plate. Flow separation in their case was induced by an adverse pressure gradient created by deflection of the wind tunnel wall. They report, "The heat transfer rate increased rapidly approaching reattachment with a peak occurring slightly downstream of the mean reattachment point" (Rivir et al., 1994).

It appears that after reattachment, the newly formed turbulent boundary layer must adjust to the presence of the wall before taking on the characteristics of a typical turbulent boundary layer. As a possible explanation for this observed heat transfer coefficient trend, Bradshaw and Wong studied such a flow (Bradshaw and Wong, 1972). At reattachment, the reattachment region of flow that separated on a backward-facing step is examined. They report, the shear layer splits. Part of the flow is deflected upstream into the recirculating flow region, while the outer region of the shear layer forms the attached shear boundary layer. This newly formed boundary layer retains characteristics of the shear boundary layer. They report, the shear layer splits. Part of the flow is deflected upstream into the recirculating flow region, while the outer region of the shear layer forms the attached shear boundary layer. Bradshaw and Wong studied such a flow (Bradshaw and Wong, 1972). At reattachment, they report, the shear layer splits. Part of the flow is deflected upstream into the recirculating flow region, while the outer region of the shear layer forms the attached shear boundary layer.

Figure 4.45: Velocity Distribution over a Separation Bubble

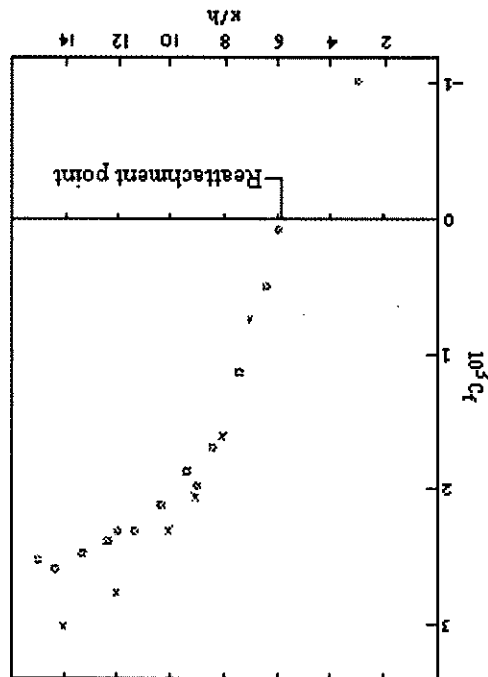
Source: Malik and Mayle, 1996



trend in the reattachment region as the skin friction coefficient was shown to follow by For the current work, the convective heat transfer coefficient is seen to follow the same

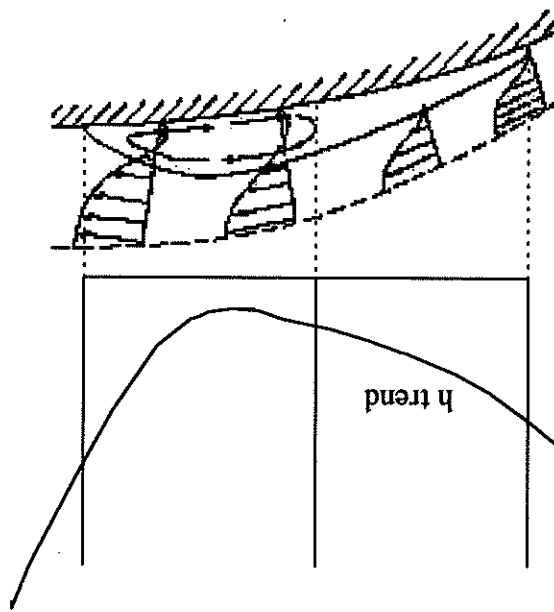
Figure 4.46: C_f Trend After Flow Reattachment

Source: Chandrusuda and Bradshaw, 1981



reattachment region of flow over a backward-facing step. Figure 4.46 shows this C_f trend in the coefficient immediately after reattachment. Figure 4.46 found a similar trend for the skin friction flow on a flat plate, Castro and Epik (1996) found a similar trend for the skin friction Yoo and Baik (1992) and by Chandrusuda and Bradshaw (1981). Looking at reattachment relaxation region the wall skin friction coefficient continues to increase as was shown by distance from the wall as is expected in a turbulent boundary layer. Finally, in the mixing length scales change from values typical of shear layers to varying linearly with a typical turbulent boundary layer value of one. In addition, in this relaxation region the intermittency of the boundary layer changes from a typical shear layer value to relaxes back to the expected "law of the wall" turbulent velocity profile. In this relaxation region, the intermittency of the boundary layer changes from a typical shear layer value to through it. Thus in the flow region immediately after reattachment, the boundary layer relaxes back to the expected "law of the wall" turbulent velocity profile. In this relaxation region, the intermittency of the boundary layer changes from a typical shear layer value to

Figure 4.47: Convective Heat Transfer in a Separation Bubble



representation of this apparent phenomenon.

A final interpretation regarding laminar separation bubbles and convective heat transfer coefficients comes from examining Figures 4.36, 4.38, and 4.40. In Section 4.1.3 it was mentioned that fluorescent oil surface flow visualization seemed to indicate a division of the laminar separation bubble into two regions. Figures 4.36, 4.38, and 4.40 contain an estimate of the extent of these two regions of the laminar separation bubble. The position of the bubble is marked by solid vertical lines, and the border between the forward stagnation region and the aft circulation region of the bubble is shown with a dash-dot vertical line. These three experimental cases were the only instances in which the oil flow was visualized photographs clearly revealed these two distinct regions of the laminar separation bubble. It appears from these figures that the minimum in convective heat transfer coefficient lies slightly after the boundary between the forward stagnation region and the aft circulation region of the laminar separation bubble. It is apparently in the aft circulation region of the laminar separation bubble that the convective heat transfer coefficient begins its increase to a turbulent level. Figure 4.47 is a qualitative representation of this apparent phenomenon.

As has been discussed, the onset of laminar separation is not clearly revealed by the heat transfer method. However, Figures 4.36 to 4.44 clearly show that the separation bubble and the minimum heat transfer region are always coincident. The location of turbulent separation is also ambiguous from the heat transfer distributions. Figures 4.38 to 4.44 contain regions of turbulent separating flow. Figures 4.38 and 4.39 do not have sufficient data in the turbulent separated region to make discussion meaningful. Therefore, the discussion will be restricted to Figures 4.40 to 4.44.

In Figures 4.40 and 4.41, the convective heat transfer coefficient appears fairly constant in the turbulent separated region. These two figures are for $\alpha = 10^\circ$, which for the Reynolds numbers considered is prior to stall. A different trend in h occurs after stall = 18°, and $\alpha = 20^\circ$. A minimum in the h distribution exists in the turbulent separated region of those figures, and the convective heat transfer is being enhanced near the trailing edge. An explanation for this heat transfer enhancement will be offered in Section 5.1.6 which discusses results of qualitative shear stress experiments.

The location of the onset of turbulent separation is not clear from the heat transfer method. One possible explanation may lie in the nature of the turbulent separation. No method, however, was a steady state approach. Only a snapshot of this "dancing" color pattern of the liquid crystals in the turbulent separated flow regions. The heat transfer phenomenon. This was observed during the heat transfer tests by noticing "dancing" color patterns of the liquid crystals in the turbulent separated flow regions. The heat transfer region at the turbulent separation location was taken and analyzed. Thus the time dependence of the separation location was lost, and the averaged h trend was found not to reveal the turbulent separation location.

Turbulent separation is also a three-dimensional phenomenon. The "dancing" separation region on the heater strip is not usually a two-dimensional line. It will be skewed at some angle (see, for instance, Figure 4.6c). However, the heat transfer coefficients were calculated based on two-dimensional columns of hue values on the strip. Thus a two-dimensional method was used on a three-dimensional flow phenomenon.

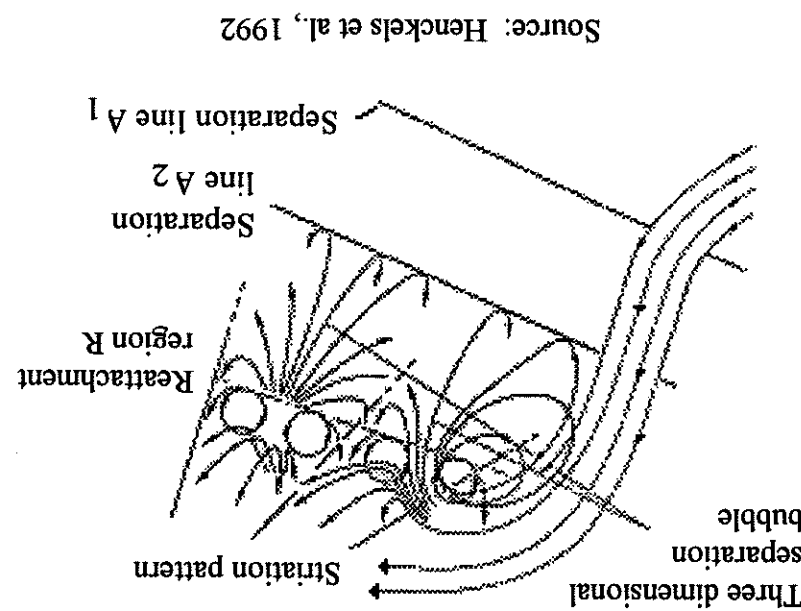
QUESTION

Now that the ability of the heat transfer method to provide flow region information has been explored by comparison to conventional oil flow visualization results, a few side topics will be explored. The first of these topics involves the formation of parallel, longitudinal vortices in the laminar separation bubble. Secondly, a comparison of the stagnation point heat transfer results at a zero degree angle of attack will be made to theoretical cylinder-in-crossflow heat transfer predictions. Finally, a word of caution will be given regarding the heat transfer method employed.

ANSWER

Now that the ability of the heat transfer method to provide flow region information has been explored by comparison to conventional oil flow visualization results, a few side topics will be explored. The first of these topics involves the formation of parallel, longitudinal vortices in the laminar separation bubble. Secondly, a comparison of the stagnation point heat transfer results at a zero degree angle of attack will be made to theoretical cylinder-in-crossflow heat transfer predictions. Finally, a word of caution will be given regarding the heat transfer method employed.

Henckels, Kriens, and Mauer observed longitudinal vortices in the reattachment region of a laminar separation bubble on a flat plate in hypersonic flow (Henckels et al., 1992). The laminar separation was caused by the pressure gradient due to an oblique impinging shock wave. They explained that the concave curvature of the boundary layer in the separation region coupled with the instabilities of the laminar shear layer gave birth to these vortices. A qualitative sketch of these reattachment vortices, known as Görtler vortices, is given in Figure 4.48.



Source: Henckels et al., 1992

Figure 4.48: Schematic Interpretation of Streamwise Vortices at Reattachment